Università degli Studi di Padova
Dipartimento di Fisica e Astronomia "Galileo Galilei"
Corso di Laurea Magistrale in Fisica

Development of Microdosimetric Techniques Applied to Hadron Therapy

Relatore: Dott.ssa Laura De Nardo

Correlatore: Dott. Paolo Colautti

Laureanda: Elisa Motisi

Anno Accademico 2014/2015

Index

Introduction **1**

1 Hadron Therapy **3**
1.1 Characteristics of Charged Particle Therapy 3
1.2 The Problem of RBE Determination 6
1.3 Hadrotherapic Centers 11

2 Microdosimetry **15**
2.1 Microdosimetric Quantities 15
2.2 Graphical Presentation of a Microdosimetric spectrum 16
2.3 RBE Determination 17

3 Detectors and Experimental Setup **21**
3.1 Tissue Equivalent Proportional Counters 21
3.2 Experimental Setup 26
3.2.1 Mini-TEPCs 26
3.3 Gas System 27
3.4 Electronic Chain 28

4 Data Analysis **31**
4.1 Pulse-height Calibration and Logarithmic Rebinning 31
4.2 Superposition Regions and Determination of the Cut Point 35
4.3 Microdosimetric Spectra and Uncertainties 36
4.4 Fermi Fit and Energy Calibration 38

5 Measurements in low-LET fields **43**
5.1 Low-LET spectra 45

6 Measurements at the CN accelerator, LNL-INFN **51**
6.1 Results 52

7 Measurements at CNAO, Pavia **57**
7.1 Beam Characteristics 57
7.2 Measurements Description 58
7.3 Results 60

8 Conclusions **67**

A C++ sources **69**
A.1 Linear Regression 69
A.2 Calibration and Rebinning 69

A.3 Determination of the Cut Point 73
A.4 Microdosimetric Spectra and Uncertainties 82
A.5 Fermi Fit 86

Introduction

Among the different treatments in radiation oncology, hadron therapy is an innovative therapeutic procedure for localized solid tumors, which are difficult to treat with standard radiation therapy.
Charged ions have good ballistic properties, which give to hadrons a great spatial precision and reduces the imparted dose to the healthy tissues surrounding the tumor. Moreover, a higher *relative biological effectiveness* (RBE) and a lower *oxygen enhancement ratio* (OER) increase hadron capability to control radioresistant and anoxic tumors.
At the present some cancer treatment centers benefit of this technique to cure a great variety of tumor types, ranging from uveal melanomas to chordomas located at the base of skull or in the spinal region [1], significantly reducing the incidence of radiation-induced second cancers. Nowadays forty-nine hadrotherapy facilities are located all over the world, twelve of which in Europe, and provide treatments with proton and carbon ions.
The main open issue in hadrontherapy is the lack of an accurate knowledge of the RBE values at different depths in the irradiated tumor. Constant values of RBE are rather adequate to describe sparsely ionizing radiations, such as fast protons, although experimental data show a significant RBE increase at the distal edge of the treated area. Such an assumption is not valid for heavier ions, such as ^{12}C ions, since their RBE values strongly vary with the depth in tissue.
A physical approach capable to assess the hadron RBE values consists in collecting the microdosimetric spectrum of the radiation under study at any point of interest. Microdosimetry is the investigation of the distributions of the energy deposited by a radiation field in tissue volumes of size close to chromosome dimensions. In the microdosimetric approach, the local energy deposition pattern and its stochastic characteristics become important, and mean quantities of radiobiological interest can be derived.
At the present many laboratories around the world are focusing in the field of microdosimetry, in particular an European project called BioQuart includes many subprojects aimed to study the correlation between the biological effects of radiation and its energy deposition pattern at micrometric and nanometric scales, including physical and biological measurements (www.ptb.de/emrp/bioquart-home.html).
Microdosimetric measurements are performed via instruments called mini-TEPCs (Tissue Equivalent Proportional Counters), which simulate the response of micrometric tissue sites to a given irradiation field. In particular this thesis deals with simulated sizes of the order of $1\mu m$, because this is the order of magnitude of the chromosome thickness.
At the moment there are few microdosimetric measurements performed in ^{12}C therapeutic beams. The aim of this work is to investigate the performances of mini-

TEPCs in a clinical carbon beam. With this beam, complications due to non-linear phenomena in the electronic avalanche of the mini-TEPC could occur. In fact, the high concentration of spatial charge built with high event rates, can disturb the electric field in the counter and distort microdosimetric spectra. The use of high gains could in principle speed-up the charge collection process, but can also lead to distortions in the final spectra.
For this reasons, the mini-TEPC response has been investigated at different voltages, corresponding to different gas-gains, both in low-LET (photons) and high-LET (fast neutrons and carbon ions) irradiation fields.
This thesis is formed by two sections. The first section is a descriptive part. It is organized as follows.

- Chapter 1 covers the general features of hadron therapy and the problems connected to the RBE determinations, describing the main models used nowadays to assess ^{12}C RBEs.
- Chapter 2 focuses on the topic of microdosimetry, defining microdosimetric quantities and their distributions. The main microdosimetric models to assess the RBE value of a radiation field and the success of the microdosimetric approach in determining proton RBE values are also presented.
- Chapter 3 deals with the mini-TEPCs description, including the physics of the counter, the electronic avalanche formation and the inherent limits of these detectors. Moreover it describes the electronic chain and the vacuum system. Finally, the simulation principle between tissue and propane-TE or pure propane is introduced.

The second section represents the experimental part, including measurements and data analysis, and it is divided as follows.

- Chapter 4 concerns mini-TEPCs data analysis. In order to optimize both in time and quality the data analysis, a GUI/C++-based software has been developed. The code algorithms are described in this chapter, and the sources can be found in appendix.
- Chapter 5 introduces the measurements performed with different mini-TEPCs in a ^{137}Cs gamma field at different applied voltages.
- Chapter 6 describes the measurements performed with different mini-TEPCs in fast neutron fields at different applied voltages.
- Chapter 7 describes the measurements performed at the CNAO clinic center with a therapeutic carbon beam. Experimental data are discussed.
- Chapter 8 presents the conclusions, the summary and future prospectives.

1. Hadron Therapy

1.1 Characteristics of Charged Particle Therapy

Radiation therapy is the treatment of malignant tumors by means of ionizing radiation. This treatment modality relies on the energy losses of energetic particles traversing a biological target, through ionizations and excitations of the constituent atoms. Therein the cellular nuclei are the main sensitive structures, since they include the DNA molecules containing the genetic information. In particular, radiation-induced ionizations can lead to single or double strand breaks in the DNA structure. While the former can be repaired using the other strand as a template, the latter are more difficult to repair and can lead to wrong rejoinings of the broken ends. These misrepairs can then induce mutations, chromosome aberrations, or cell death.
The most common form of radiotherapy uses photons, with an estimated yearly rate of 1 patient every 10 million people [4]. Hadron therapy differs from conventional therapy in many aspects, such as depth-dose profiles, LET[1], OER[2] and RBE[3] values. These are key quantities in radiation therapy and are discussed in more detail, later on.

Dose Profile The *absorbed dose* is a quantity used to quantify the exposure of a medium to ionizing radiation. The absorbed dose in a point is defined as the quotient of $d\epsilon$ by dm, where $d\epsilon$ is the mean energy imparted to matter in an infinitesimal volume $dV \to 0$ in a material with density ρ, and dm is the mass in dV. It is expressed in gray, where $1\ Gy = 1\ J \cdot 1\ kg^{-1}$ [3].
This point quantity is thus defined in the limit of small domains, assuming an energy density function continuous and derivable in the geometrical space. The non-stochastic absorbed dose in tissue is the average of this quantity in the tissue volume, and it is used in radiation protection.
Qualitatively the dose profile for a beam of therapeutic photons or neutrons traversing biological matter exhibits an initial increase followed by a roughly exponential decrease. Figure 1.1 shows the comparison between the depth-dose curve of a

[1]The Linear Energy Transfer of a charged particle in a medium is the quotient of dE on dl, where dl is the distance traveled by the particle and dE is the mean energy-loss due to collisions with energy transfers less than some specified value Δ [2], $L_\Delta = (dE/dl)_\Delta$.

[2]OER, standing for Oxygen Enhancement Ratio, is defined as the ratio of the doses necessary to cause the same biological effect in hypoxic and oxygenated conditions respectively.

[3]This quantity is defined as the ratio of the absorbed dose of some reference radiation which produces a given biological effect, to the absorbed dose of the test radiation that produces an identical effect. For a given radiation R and a reference radiation X, the RBE is $RBE_R = D_X/D_R$, where normally the reference radiation is 250kV X-rays.

photon-beam and the curves due to other types of ionizing radiations while traversing soft tissues (e.g. ligaments, skin, muscles, etc.).

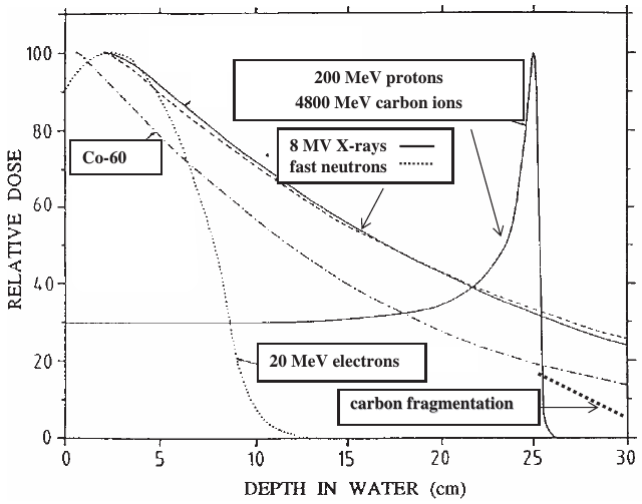

Figure 1.1: Comparison between depth-dose curves for photons, neutrons and protons, as in [4].

Energetic charged ions, on the other hand, deposit little energy in their initial path. The majority of energy deposition takes place at the end of their path, generating a peak in the depth-dose profile (Bragg peak). After that, the deposited energy strongly decreases. These features allow to obtain a better dose conformation, and a more selective tailoring of the biological area to be treated, by using charged ions instead of photons, neutrons or electrons. For ions heavier than proton, there is also the advantage of a reduced lateral diffusion, which gives the projectiles even more spatial precision.
This "inverse-dose" profile is consequence of the interaction mechanisms of heavy charged ions in the target material. In the energy range used in therapy, they mainly interact with the target electrons and slow down continuously (Continuous Slowing Down Approximation). For higher ion energies the interaction time is short, leading to small energy transfer, while the opposite happens at lower energies. The energy loss as a function of the ion and target characteristics is given by the Bethe-Bloch formula given (in non-relativistic conditions) by

$$-\frac{dE}{dx} = \frac{4\pi e^4 z_{eff}^2 ZN}{m_e v^2} ln\Big(\frac{2m_e v^2}{< I >}\Big), \tag{1.1}$$

where v and z_{eff} are the velocity and the charge of the primary particle (z_{eff} is equal to its atomic charge at high velocities), m_e is the electron mass, N and Z are the number density and the atomic number of the traversed material and $< I >$ is the mean ionization energy of the target atom or molecule.
In practical situations, due to the narrowness of the Bragg peak of monoenergetic ions (typically of the order of one millimeter or less), it is necessary to superimpose several different Bragg-peaks to spread them properly over the tumor area. This is done by decreasing the energy of the initial ion beam and opportunely weighting the components of different energy (assigning the relative fraction of dose to be imparted with a given energy). The result is a "flat-topped" depth-dose curve, known as SOBP (Spread Out Bragg Peak), depicted qualitatively in Figure 1.2 for a beam of protons. The advantage of this technique is to decrease the imparted dose in the region before

and after the tumor site.

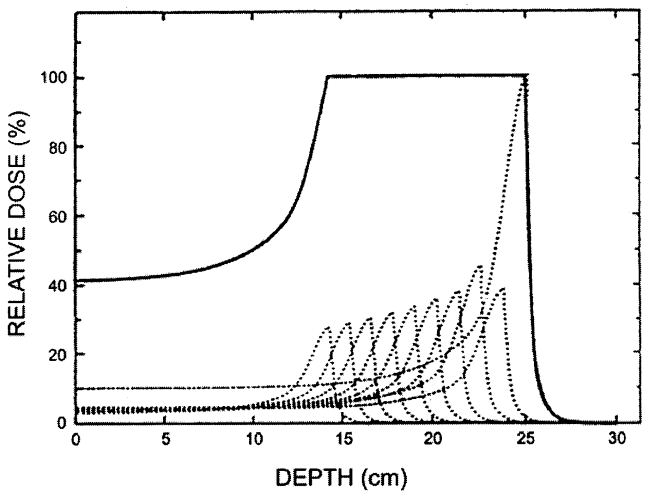

Figure 1.2: Depth-dose distributions for a spread-out Bragg peak (SOBP, solid curve) and its constituent Bragg peaks (dotted curves). The SOBP profile is created by adding several Bragg peaks with different energy, their number depending on the depth of the region to be treated.

With ions heavier than protons, the depth-dose profile is worsen by the presence of a tail component of fast charged particle arising from the nuclear fragmentation of the projectile, which causes a significant amount of energy to be imparted in the distal part after the tumor. A comparison between the depth-dose curves and SOBPs of protons and carbon ions is shown in Figure 1.3 and Figure 1.4 respectively.

The radiobiological and clinical effects are directly related to the absorbed dose, yet this is not sufficient to give an estimate of the complete biological effect, which also depends on the type of irradiation.

Difference in LET As previously stated, the *Linear Energy Transfer* L_Δ for charged particles of a given type and energy stopping in a material is the quotient of dE_Δ by dl, where dE_Δ is the mean energy lost by the charged particles due to electronic interactions in traversing a distance dl, minus the energy carried away by energetic secondary electrons produced with kinetic energies greater than Δ. If no energy cut off is imposed, the unrestricted LET equals the linear electronic stopping power. L_Δ specifies the amount of local energy imparted to the target, thus it is linked to the proximity and distribution of ionization points.
From now on the term LET will refer to the unrestricted linear energy transfer L_∞. Low-LET radiations are for example photons and electrons, where the electrons responsible for the ionizations are subjected to scattering and deflection at large angles in the absorber, giving a "sparse" ionization pattern.
For charged ions, the ionizations are mostly included in the core and in the neighboring part of the δ-ray penumbra of the primary track. For this reason charged ion radiation is also called *densely ionizing* and leads to higher LET values.
It has been observed that a high-LET radiation is in general more effective in causing biological damages than a low-LET one, in fact the single or double strand breaks of the DNA are more concentrated. Carbons have a higher LET if compared to protons due to their higher nuclear charge. For this reason, a carbon irradiation

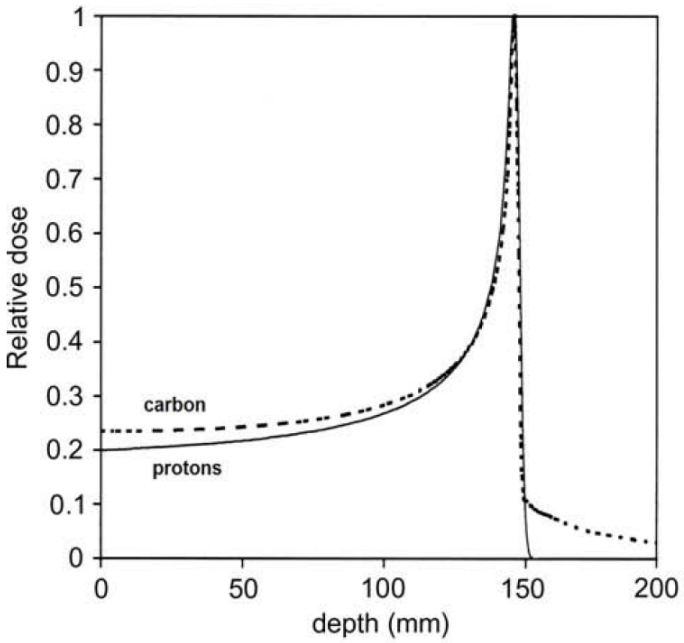

Figure 1.3: Relative depth-dose distributions for a 145 MeV proton beam and a 276 MeV/amu carbon beam, with a range of ∼14 cm [5].

causes more severe local damages and has a greater effectiveness when treating radioresistant tumors compared to protons and photons.

Difference in OER The effects caused in an irradiated tumor also depend on the oxygen content of the irradiated tissues. The amount of oxygen enhances the sensitivity of the irradiated cells, increasing the biological effect of radiation through the production of free radicals which cause additional damages, other than those attainable considering only the direct interactions of photons with tissue [19].
The ratio of the doses needed to produce the same effect in the presence and absence of oxygen is the Oxygen Enhancement Ratio parameter, $OER = D/D_0$, where D is the dose in the real tissue and D_0 is the dose that would be required under complete tissue oxygenation.
In tumors, the oxygen content may vary, the fraction of hypoxic cells also reaching 100% for some solid tumors. This would require the increase of the dose delivered for a better tumor control, at the expense of the growth of side effects.
The difference in radiation sensitivity between hypoxic and oxygenated cells has been proved to decrease if a high-LET radiation is employed, allowing to monitor the biological response of a tumor independently on its vascularization degree.

1.2 The Problem of RBE Determination

One of the main challenges in hadron therapy is the identification of physical parameters related to the biological effects of radiation, such as the inactivation of tumor cells and the sparing of normal tissues.
Nowadays the Linear Quadratic model (LQ) is used as a model of cell killing. In-

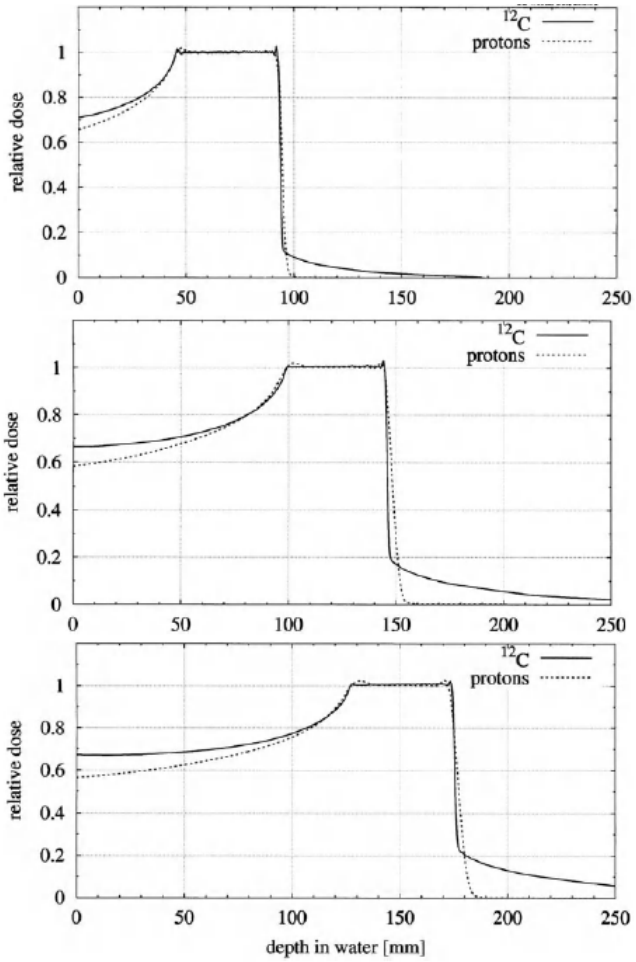

Figure 1.4: Comparison of calculated SOBPs of protons and carbon ions at a penetration depth of 100 mm (upper figure), 150 mm (middle figure) and 180 mm (lower figure) [6]. The corresponding proton energies are 116 MeV, 146 MeV and 162 MeV, respectively. The carbon ion energies are 216 MeV/amu, 275 MeV/amu and 307 MeV/amu, respectively.

vitro as well as in-vivo experiments show that the fraction of surviving cells can be described through a linear-quadratic function of the absorbed dose, namely [8]

$$S = exp[-(\alpha D + \beta D^2)], \tag{1.2}$$

where the coefficient α is the slope at small doses and β is the curvature at larger doses.
This trend of experimental data can be interpreted as follows. When a cell sample undergoes a given irradiation, the radiation field is responsible for the production of double-strand breaks (DSBs) or base damage in the DNA, at a rate which is, in first approximation, proportional to the dose. When pairs of adjacent DSBs wrongly rejoin together, chromosome aberrations can occur producing lethal lesions.
Experimentally it is found that densely ionizing radiation has a greater biological impact than X-rays for the same dose level. In fact, X-ray dose response has a large shoulder at low doses and an exponential decrease at higher doses, as shown in Figure 1.5, while for charged ions the quadratic component decreases with increasing ionization density (LET) and the survival curve is characterized by a purely exponential trend.

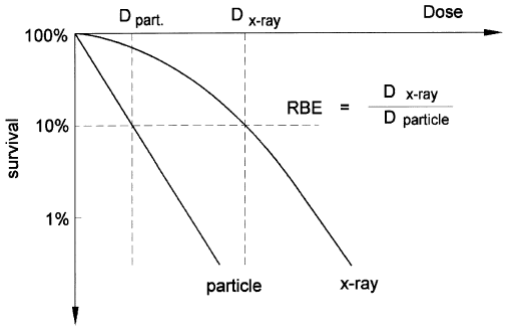

Figure 1.5: Definition of the Relative Biological Effectiveness, illustrated for cell survival curves, as in [6].

For different radiations the same level of physical dose can correspond to different cell survival levels. To cope with the inadequacy of the sole dose concept, and to compare the biological effects of various types of irradiations, the concept of RBE has been introduced, defined as the ratio of a reference X-ray dose (typically 250kV X-rays) to the particle dose to achieve the same biological effect, e.g.

$$RBE_{10\%} = \frac{D_X}{D}, \tag{1.3}$$

where the subscript stresses the RBE dependence on the survival level representing the equivalence point. This definition is depicted qualitatively in Figure 1.5. The RBE alone does not fully characterize the therapeutic beam, since it depends on the type and energy of the radiation, on the dose fractionation history, on the biological end-point and cell-line considered. Because of the non-linearity of the X-ray curve, the RBE strongly depends on the effect level. For for carbon ions RBE values of 3 or 4 are found at the end of their range, where the high local ionization density cause clustered lesions producing irreparable DNA damage. For RBE values greater than one an *effective dose* D_{eff} is defined

$$D_{eff}[GyE] = RBE \cdot D[Gy], \tag{1.4}$$

measured in Gray equivalent (GyE). In radiation therapy the optimization of the weighting factors of the various Bragg peaks forming the SOBP must then be made by taking into account the effective dose, rather than the physical dose, to achieve homogeneous killing effect over the treated area.
RBE values are not easily accessible, due to the variety of parameters they depend on, therefore various models have been proposed to estimate RBE values from physical measurements.
The first radiobiological experiments by Zirkle et al. in 1935 showed that to fully describe the biological effectiveness of a ionizing radiation, the spatial distribution of energy deposition must be taken into account.
It was thus proposed to describe the biological damage in terms of the LET of the incident primary particle, linking the concentration of deposited energy to the damages in microscopic structures near the particle track. In this view low-LET radiations are less damaging than high-LET ones.
In first approximation the RBE is related to the LET. The first RBE-LET relation obtained by Barendesen [9] for alphas and deuterons showed an increase of RBE with LET until a maximum, then a decrease attributed to cell overkilling. In a recent work by Sørensen et al. [10], several literature data of the RBE dependence

on LET have been summarized, showing a correlation between the dose-averaged LET and the RBE values for three different cell lines (for V79, CHO and T1), as it can be seen in Figure 1.6.

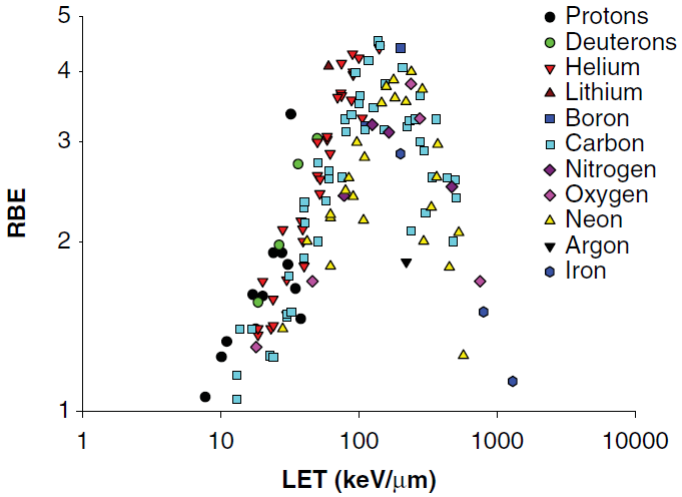

Figure 1.6: Relationship between RBE and LET for various charged particles irradiating V79 cells, where the biological endpoint considered is a 10% survival fraction, as in [10].

In general however, the RBE is not a unique function of the LET, the difference being attributed to the change in the track structure of the primary particles. Moreover, the LET changes with the traveled depth in tissue and so does the RBE, making any RBE-value assumption inaccurate.
Currently in proton clinics a RBE value of 1.1 is adopted, despite the evidence of RBE variations with the depth traveled in tissue (due to proton energy and LET variations) or dose fractionation, tissue type and biological endpoint. The magnitude of these RBE variations is small in the plateau region of the SOBP if compared to the current abilities to determine RBE values [31], and differences are of the order of $10 \div 20\%$ [17], while in the distal edge the differences are much higher.
For heavier ions like carbons, RBE values are higher and their variations with depth are more pronounced even in the plateau region. In particular, it was shown for many cell lines that in the initial part of the carbon path the ionizations produce mostly repairable damages, while the RBE becomes greater than 1 in the last 40 mm of the carbon track (in water or in biological tissue) [4]. Therefore, the correct inclusion of a variable-RBE model in carbon therapy is crucial.
Two of the current approaches to obtain RBE values in carbon therapy are discussed.

NIRS approach At the National Institute of Radiological Sciences, located in Chiba (Japan), the clinical dose to be assigned to a carbon beam is determined through an experimental approach, using the clinical experience with fast neutron beams and a dose-scaling procedure, taking into account just the LET dependency of RBE [11].
The empirical procedure relies on the observation that the RBE values of a 290 MeV/amu carbon ion beam and of the fast NIRS neutrons are equal when the LET of the carbon beam is 80 $keV/\mu m$, inducing the same biological effect on a Human Salivary Gland cell-line (HSG) at 10% survival probability, since these cells are assumed to be a good marker of the tumor response. This is shown in Figure 1.7.

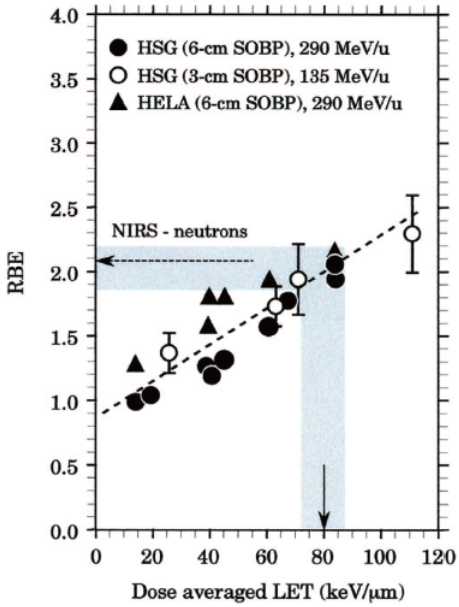

Figure 1.7: RBE-LET in-vitro data for the irradiation of HSG and HeLa cells for carbon ion beams with different energies, as in [13]. The horizontal arrow shows the RBE of NIRS neutrons, the vertical line marks the LET value of the carbon ion beam which leads to the same RBE value.

The carbon ion dose-depth profile is shaped in order to achieve a uniform *in-vitro* SOBP, corresponding to a 10% survival of the HSG cells. Since the neutron-equivalent point for a 290 MeV/amu carbon ion beam corresponds to a depth traveled in water of about 150 mm, the constraint is that the RBE at this depth is equal to 2.
The RBE of fast neutrons used in clinical practice at NIRS is equal to 3. It is assumed that the *in-vitro* carbon SOBP can be converted into a *clinical* SOBP by simply scaling the *in-vitro* SOBP for a factor 3/2 at the point of neutron equivalence, namely the ratio of clinical and in-vitro neutron RBEs. The dose scaling procedure is illustrated in Figure 1.8.
The main critic to the NIRS approach derives from the fact that the RBE equivalence between neutron and carbons is set independently from the dose and the radiosensitivity of the irradiated tissues. In principle these parameters should be taken into account when estimating RBE values.

GSI approach In order to describe the RBE of high-LET therapeutic beams, various track structure–based models were developed, such as the Local Effect Model (LEM) developed at GSI [14]. This model is currently used in order to optimize the treatment planning at the HIT (Heidelberg) and CNAO (Pavia) ion-therapy facilities.
The idea behind the LEM model is that the critical structures leading to the biological damage, are contained in the cell nucleus, which is considered as the sensitive target. This can be divided into smaller sub-volumes, with nanometric size, where the probability to induce a damage depends only on the local energy deposition, regardless of the radiation type causing it. In this view, equal local doses correspond to equal local radiation effects and the biological response to carbon ions can be derived from X-ray cell survival curves.

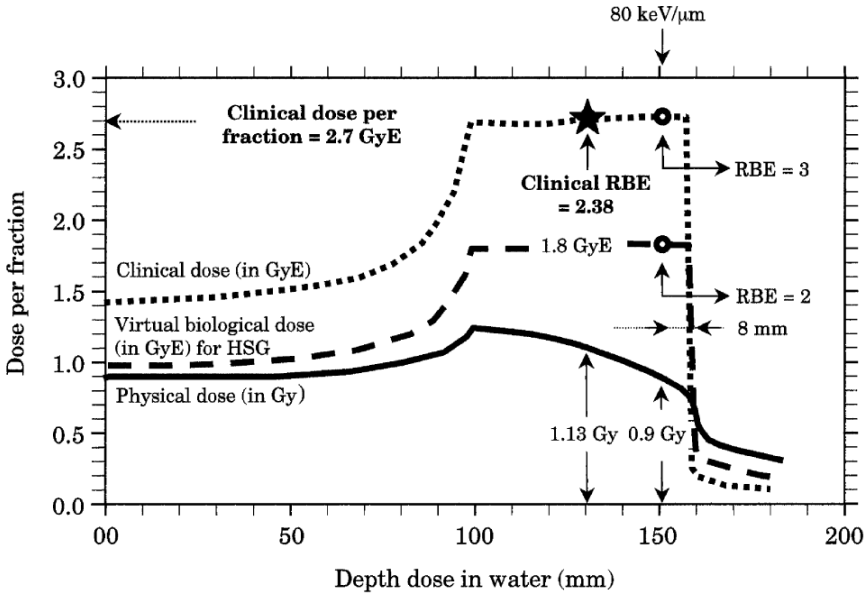

Figure 1.8: Scheme illustrating the determination of the clinical SOBP, as in [13]. The physical dose (solid line) is converted into an in-vitro SOBP (dashed line) by using RBE values at a 10% survival level for HSG cells. The in-vitro SOBP is then scaled by a factor 3/2 to obtain the final clinical SOBP (dotted line).

Three parameters are needed as input in the model, to calculate the probability of cell inactivation for a heavy ion field. The first is the radial dose profile of the incident primary particle, which is assumed to be constant in the core of the primary track, and decreasing with the square of the distance in the penumbra. This allows to calculate the local dose in the sensitive sub-volumes by superimposing the contributions of the different particles which contribute to the energy deposition in that volume. The second input parameter is the target geometry, which is assumed to be a cylinder with experimentally determined radius and which height is kept small compared to LET variations in that volume. The last parameter are photon survival curves (fitted by the linear-quadratic model), which are used to make the connection between the local imparted doses and the actual biological effect.
The principle behind the model is depicted in Figure 1.9.
The model allows to obtain a clinical proton RBE of $1.2 \div 1.3$, and the RBE mapping for carbon ions.
The main critics to this model arise from the principal assumption. In fact, the possibility to use a low-LET survival curve to characterize the effect of high-LET radiations is in contrast with the experimental observation that different-LET radiations produce different effects, due to the different ability of their individual tracks to produce clustered damages [15].

1.3 Hadrotherapic Centers

The features of charged particles make them useful in the case of spatially defined solid-tumors. However, particle therapy has also some practical disadvantages. One issue are the high costs involved, in fact the global investments needed for a proton therapy and a combined (protons and carbons) facilities are 3.6 and 5.3 times that of a photon facility, respectively [7]. These arise from the need of a more skilled

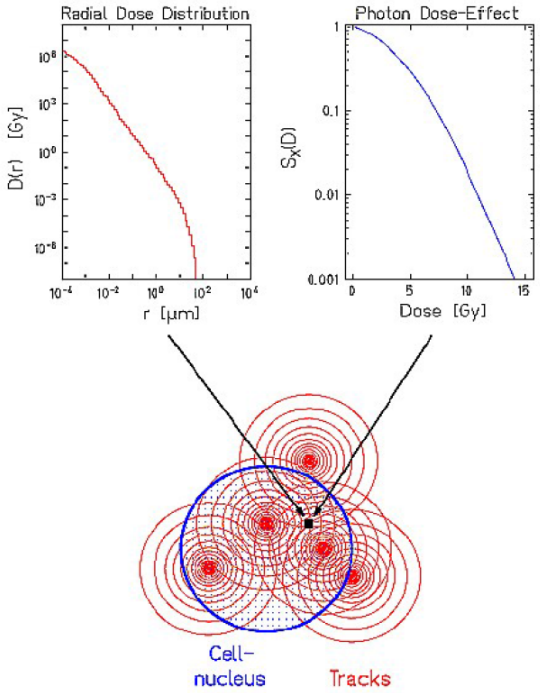

Figure 1.9: The cell nucleus (blue circle) is hit by particles with a given radial dose profile (red circles). In each cellular sub-volume (black dots) it is possible to calculate the locally imparted dose, knowing the radial dose profile of the primary particles (shown in the upper left). The local dose deposited is linked to the cell survival probability through the survival curves obtained for photon irradiation (upper right).

staff and the requirement of dedicated facilities to deliver ion beams.
From the operating point of view, ion therapy is also more sensitive to the depth traveled in tissue than photon therapy, and the accurate positioning of the patience together with accurate scanning and imaging techniques is more crucial.
Finally, the determination of the clinical dose to be provided still represents an open issue. This is discussed in Section 1.2.
Nowadays the existing ion-therapy facilities use protons and carbon ions, which energy and type is chosen according to the depth of the tumor. A list of the current treatment centers can be found in Table 1.1. The use of other types of ions is currently under investigation.

COUNTRY	WHO, WHERE	PARTICLE	START OF TREATMENT	TOTAL PATIENTS TREATED	DATE OF TOTAL
Canada	TRIUMF, Vancouver	p	1995	175	Dec-13
Czech Republic	PTC Czech r.s.o., Prague	p	2012	140	Dec-13
China	WPTC, Wanjie, Zi-Bo	p	2004	1078	Dec-13
China	IMP-CAS, Lanzhou	C-ion	2006	213	Dec-13
China	Fudan University CC, Shanghai	C-ion	2014	36	Sep-14
England	Clatterbridge	p	1989	2446	Dec-13
France	CAL, Nice	p	1991	4936	Dec-13
France	CPO, Orsay	p	1991	6432	Dec-13
Germany	HZB, Berlin	p	1998	2312	Dec-13
Germany	RPTC, Munich	p	2009	1811	Dec-13
Germany	HIT, Heidelberg	p	2009, 2012	503	Dec-13
Germany	HIT, Heidelberg	C-ion	2009, 2012	1368	Dec-13
Germany	WPE, Essen	p	2013	32	Dec-13
Italy	INFN-LNS, Catania	p	2002	350	Dec-13
Italy	CNAO, Pavia	p	2011	76	Dec-13
Italy	CNAO, Pavia	C-ion	2012	105	Dec-13
Italy	APSS, Trento	p	2014	first patient	Oct-14
Japan	HIMAC, Chiba	C-ion	1994	8073	Dec-13
Japan	NCC, Kashiwa	p	1998	1226	Mar-13
Japan	HIBMC, Hyogo	p	2001	4223	Dec-13
Japan	HIBMC,Hyogo	C-ion	2002	1935	Dec-13
Japan	PMRC 2, Tsukuba	p	2001	2967	Dec-13
Japan	Shizuoka Cancer Center	p	2003	1590	Dec-13
Japan	STPTC, Koriyama-City	p	2008	2306	Dec-13
Japan	GHMC, Gunma	C-ion	2010	985	Dec-13
Japan	MPTRC, Ibusuki	p	2011	919	Dec-13
Japan	Fukui Prefectural Hospital PTC, Fukui City	p	2011	428	Dec-13
Japan	Nagoya PTC, Nagoya City, Aichi	p	2013	199	Dec-13
Japan	SAGA-HIMAT, Tosu	C-ion	2013	62	Dec-13
Japan	Aizawa Hospital PTC, Nagano	p	2014	first patient	Oct-14
Poland	IFJ PAN, Krakow	p	2011	39	Dec-13
Russia	ITEP, Moscow	p	1969	4320	Dec-13
Russia	St.Petersburg	p	1975	1386	Dec-12
Russia	JINR 2, Dubna	p	1999	995	Dec-13
South Africa	NRF - iThemba Labs	p	1993	521	Dec-13
South Korea	NCC, IIsan	p	2007	1158	Dec-13
Sweden	Svedberg Lab.,Uppsala	p	1989	1356	Dec-13
Switzerland	CPT, PSI, Villigen	p	1984, 1996, 2013	7045	Dec-13
USA, CA.	J. Slater PTC, Loma Linda	p	1990	17829	Dec-13
USA, CA.	UCSF, San Francisco	p	1994	1621	Dec-13
USA, MA.	MGH Francis H. Burr PTC, Boston	p	2001	7345	Dec-13
USA, IN.	IU Health PTC, Bloomington	p	2004	1927	Dec-13
USA, TX.	MD Anderson Cancer Center, Houston	p	2006	4746	Dec-13
USA, FL.	UFPTI, Jacksonville	p	2006	5085	Dec-13
USA, OK.	ProCure PTC, Oklahoma City	p	2009	1364	Dec-13
USA, PA.	Roberts PTC,UPenn, Philadelphia	p	2010	1744	Dec-13
USA, IL.	CDH Proton Center, Warrenville	p	2010	1329	Dec-13
USA, VA.	HUPTI, Hampton	p	2010	767	Dec-13
USA, NY.	ProCure Proton Therapy Center, New Jersey	p	2012	512	Dec-13
USA, WA.	SCCA ProCure Proton Therapy Center, Seattle	p	2013	86	Dec-13
USA, MO.	S. Lee Kling PTC, Barnes Jewish Hospital, St. Louis	p	2013	93	Oct-14
USA, TN.	Provision Center for Proton Therapy, Knoxville	p	2014	100	Aug-14
USA, CA.	Scripps Proton Therapy Center, San Diego	p	2014	first patient	Feb-14
USA, LA.	Willis Knighton Proton Therapy Cancer Center, Shreveport	p	2014	first patient	Sep-14

Table 1.1: Hadrontherapy facilities worldwide in operation (source www.ptcog.ch,updated 09-Nov-2014).

2. Microdosimetry

2.1 Microdosimetric Quantities

As stated in Chapter 1, a correct evaluation of the biological effects due to a given kind of irradiation field is unfeasible without knowing the details of the energy deposition pattern. The main biological sensitive structures are chromosomes and DNA. At the chromosome level the stochastic characteristics of the energy deposition are dominant, due to the interplay between the discrete distribution of the sensitive components in irradiated matter and the discreteness of the microscopic energy deposition pattern.
The main objective of microdosimetry is the investigation of the imparted-energy probability distributions in irradiated matter [40], considering single charged-particle passages across the volume of interest (single events), of micrometric size.
A basic microdosimetric quantity is the *energy deposit* ϵ_i which is the energy absorbed in a given *transfer point*, given by

$$\epsilon_i = E_{in} - E_{out} + Q, \tag{2.1}$$

where E_{in} is the energy of the ionizing particle without taking into account its rest mass, E_{out} is the sum of the energies of all particles leaving the transfer point and Q is the change in the rest masses, that has to be considered when nuclear reactions or pair production are involved, since they can further release ($Q > 0$) or absorb ($Q < 0$) the energy. The point of interaction is called *transfer point* when the deposited energy exceeds the minimum value required to cause a given change (e.g. ionization).
The number of the relevant transfer points is linked to the probability of occurrence of a given biological effect.
The quantity ϵ describes the sum of all the energy deposits in the site arising from one or more particles and their secondaries. This is a stochastic quantity, since the underlying physical processes are stochastic.
The *lineal energy* is the ratio of the energy imparted to the volume due to a single event ϵ to the mean chord length $\bar{l}$ of the volume

$$y = \frac{\epsilon}{\bar{l}}. \tag{2.2}$$

The mean chord length of a convex volume is the mean length of randomly oriented chords in the volume which, according to a theorem by Cauchy, for a convex body with volume V and surface area S is given by the equation

$$\bar{l}_{convex} = \frac{4V}{S}, \tag{2.3}$$

which will be recalled in Section 3.2. This parameter is introduced to take into account the geometry of the interaction, since the paths of energy deposition can intersect the site through a variety of chord lengths.
The occurrence of the different lineal energy events can be described through the frequency probability density $f(y)$ and the fraction of dose imparted between events of different dimensions, is described through a dose distribution $d(y)$.
The relation between the two probability densities is

$$d(y) = \frac{y}{\bar{y}_F} f(y), \tag{2.4}$$

where $\bar{y}_F$ is the frequency-averaged lineal energy value.
The *specific energy imparted* z is the ratio of the energy imparted to the volume and the mass m inside it

$$z = \frac{\epsilon}{m}. \tag{2.5}$$

Similarly to the case of lineal energy, the frequency $f_1(z)$ and dose $d_1(z)$ probability densities can be defined, where the subscript 1 refers to a single event. In this condition the lineal and the specific energy are proportional to each other.
For a large number of events in the site volume, the distribution of specific energy shows small fluctuations from its mean value, and the average value of multi-event specific energy can be thought as the absorbed dose

$$D \approx \bar{z} = \int_0^\infty z f(z) dz, \tag{2.6}$$

where $f(z)$ is the multi-event distribution that can be derived from $f_1(z)$ through a convolution operation [40].

2.2 Graphical Presentation of a Microdosimetric spectrum

Microdosimeters analyze a variety of radiation fields, from fast electrons produced by gamma radiation to low-energy heavy recoils produced in neutron fields. Due to this feature, a microdosimetric spectrum must be capable of inspecting a broad range of imparted energies, covering several orders of magnitude. A lower limit is set by the smaller observable event which is the production of one electron, typically 30 eV (approximately the ionization potential of the employed TE gases). The upper limit strongly depends on the inspected flux of charged particles and can achieve hundreds of keV.
To deal with this large range of energies and to compare results obtained under different experimental conditions, the conventional approach consists in dividing the lineal energy axis into equal logarithmic intervals, while presenting the frequency or dose distributions on a linear axis.
In the frequency distribution spectrum, equal areas represent equal fractions of observed events, while in the dose distribution spectrum equal areas between different lineal energy values represent equal fractions of imparted dose by those events.
The details of the logarithmic presentation are discussed later on, in Section **??**.
An example of microdosimetric spectrum for a neutron source is presented in Figure 2.1.

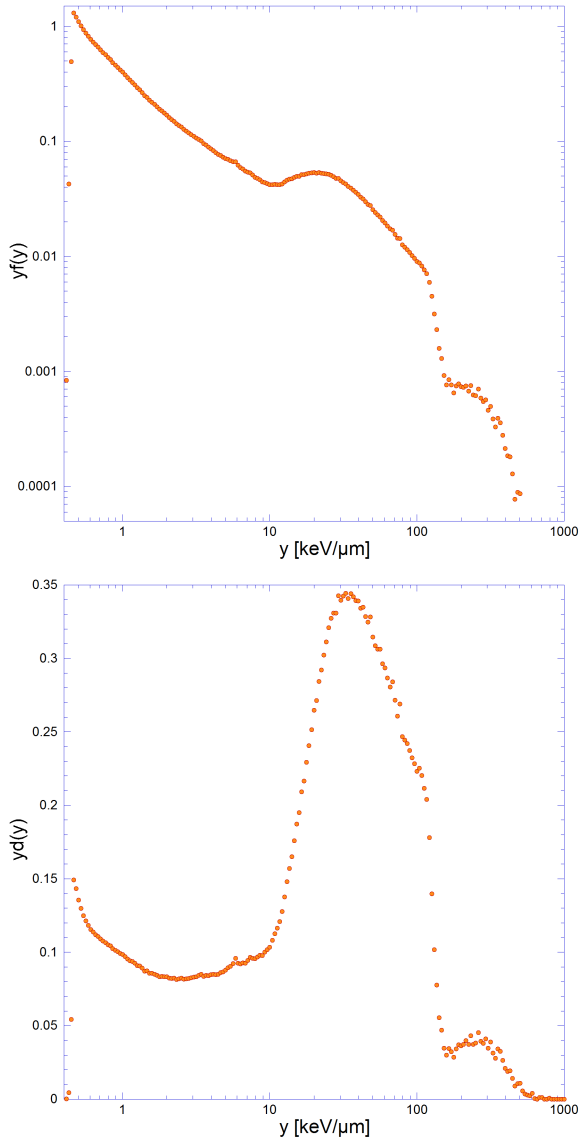

Figure 2.1: Frequency (normalized counts) and dose distributions for a neutron source, as a function of the lineal energy.

2.3 RBE Determination

As stated in the previous chapter, the RBE of a therapeutic beam is related to the spatial distribution of energy deposition events, as this influences the biological effectiveness of a radiation. RBE can be described through physical microdosimetric measurements, which are more reproducible and faster than radiobiological ones.

Microdosimetric approach Radiobiological and microdosimetric measurements taken in the same conditions, can be used to assess the RBE of a generic irradiation field by determining an empirical distribution in the lineal energy domain called *biological weighting function* $r(y)$. This parameter actually depends on the radiobiological parameters at which it is calculated, such as biological endpoint and absorbed dose, and on the simulated biological size in microdosimetric spectra. Its

determination is based on the assumption that the information on single event spectra $d(y)$ is sufficient to determine the contribution of different radiation components to the total biological effectiveness.
In particular, the microdosimetric RBE values are defined as

$$RBE_{\mu} = \int_0^{\infty} r(y)d(y)dy \approx \sum_{y_0}^{y_{max}} r(y_i)d(y_i)\Delta y_i., \tag{2.7}$$

The advantage is that the microdosimetric measurements can be performed for a wide variety of irradiations, and the function $r(y)$ can be obtained through iterative unfolding methods [22].
Few $r(y)$ distributions have been derived in literature using different RBE-d(y) sets. For example in work by Pihet et al. [23] the $r(y)$ function was obtained from radiobiological RBE values for early effects in mice at 8 Gy for clinical beams of fast neutrons, and microdosimetric spectra at 2 μm site size. In a successive work by Loncol et al. [24] the feasibility of this procedure was studied for beams of fast protons, leading to the extension of the $r(y)$ function, presented in Figure 2.2.

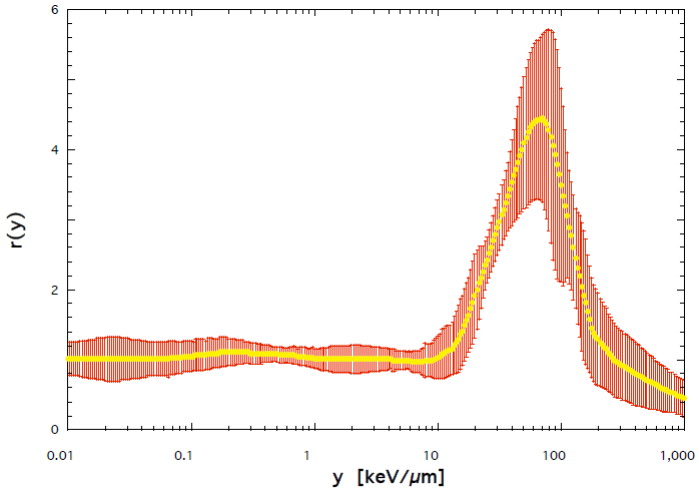

Figure 2.2: Biological weighting function for early intestine damage in mice at 8 Gy at 2 μm simulated size, as in [24]. The red bars represent $r(y)$ uncertainties.

As an application of these findings, the physical quality of the therapeutic proton beam of the Center Antoine-Lacassagne of Nice has been measured in a measurement campaign by De Nardo et al. [25] and RBE_{μ} have been calculated using the different weighting functions present in literature for early intestine damage in mice at 8 Gy. It was then made a comparison with in-vitro radiobiological data of human melanoma and human tongue cell carcinoma surviving at 2 Gy. The comparison showed that the radiobiological RBE values are well fitted by the calculated RBE_{μ} values within their uncertainties, including the statistical errors on the $d(y)$ distributions and the $r(y)$ uncertainty, when the function of Figure 2.2 is used.

In Figure 2.3 it is shown the comparison of radiobiological and microdosimetric RBEs, as a function of the depth in ocular tissue (the pristine Bragg peak corresponds to a proton energy of 61.5 MeV). Taking into account RBE_{μ} values the effective dose imparted is calculated, and it is shown in Figure 2.4. The biological

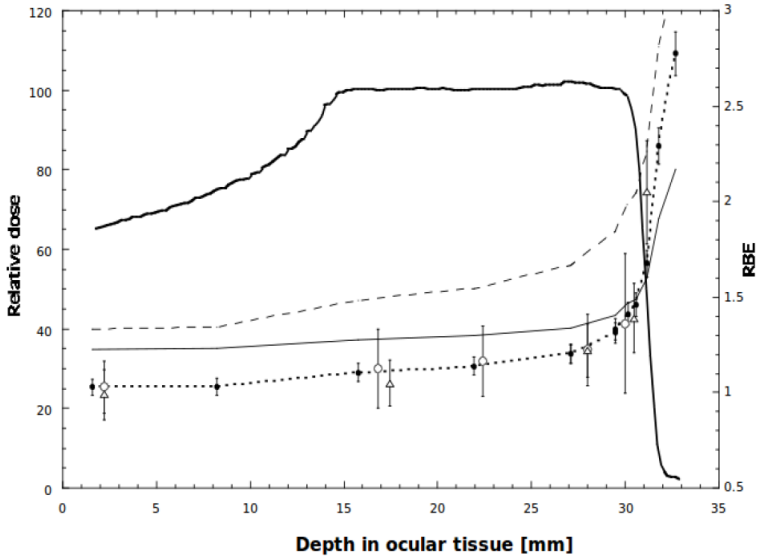

Figure 2.3: Comparison between radiobiological and microdosimetric RBEs, as in [25]. The full line is the proton SOBP and the triangles are RBE for human tongue cell carcinoma at 2 Gy, the open circles RBEs for human melanoma cells at 8 Gy. The full circles are RBE_μ values calculated with the weighting function of Loncol et al. [24] at 8 Gy. RBE_μ values calculated with the weighting function of Tilikidis et al. at 10 Gy and at 2 Gy [26] are represented by the continuous line and dashed line.

effective dose varies of the 30% along the SOBP and presents the highest variation in the distal part, showing that the radiation damage for protons cannot be considered uniform inside the irradiated volume. Moreover, the microdosimetric data show that the effective distal edge of the SOBP shifts of about 0.5 mm, which can lead to a significant dose contribution in the healthy tissues surrounding the tumor. From these measurements it was also shown that the microdosimetric approach is effective in monitoring therapeutic beams, by using suitable weighting functions.

MKM model Throughout the years microdosimetric quantities have often been used in models describing the occurrence of biological lesions, such as the clustered-damage model called the *Theory of Dual Radiation Action* (TDRA). This was proposed by Kellerer and Rossi in 1972 [34], who postulated that the effect of ionizing radiation on cells is the production of entities called *sublesions*, with a rate proportional to the specific energy in the target volume. In the model, the sublesions combine in pairs to produce the *lesions* responsible of the various biological effects, which expectation value ϵ will accordingly be proportional to the square of the specific energy

$$\epsilon(z) = Kz^2. \tag{2.8}$$

Even if some of the assumptions of TDRA were invalidated by experimental tests [35], the Microdosimetric Kinetic Model (MKM) of cell death incorporates aspects of TDRA and other models as mathematical formalism [36].
In the model the lethal lesions can be due to the combination of two sub-lesions, but also to the lack of repair of single sub-lesions after a certain amount of time, thus introducing a term proportional to the imparted energy

$$\epsilon(z) = \alpha z + \beta z^2. \tag{2.9}$$

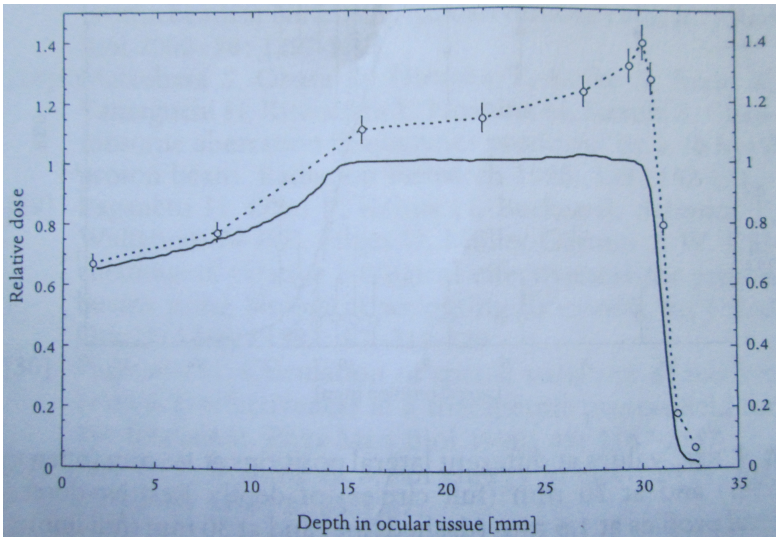

Figure 2.4: Physical absorbed dose and biological effective dose (circles and dashed line) comparison, as in [25].

In the description of the dose-effect relationship, the model takes into account the dimensions of the domains containing the critical targets and the LET of the irradiating field, together with the repair capability of the system from a kinetic or "temporal" point of view.
This model has been recently tested experimentally at the NIRS center in Japan, with the aim to include it in future treatment planning [27], [28].

Other applications

Area monitoring In area monitoring a quantity called *quality factor* Q gives an indication of the dose equivalent, which is important in unknown radiation fields. Area monitors measuring microdosimetric spectra are of practical importance, since the probability density $d(y)$ can be used to asses the mean quality factor [32] through the relation

$$Q = \int_0^\infty q(y)d(y)dy, \tag{2.10}$$

where the functions q(y) substitute the classical dependence of the quality factor on LET $Q(L_\infty)$, established in early works of radiation protection [33], typically setting $y = \frac{9}{8}L_\infty$ [42].

3. Detectors and Experimental Setup

Microdosimetric measurements are performed with different types of detectors, the most common ones being gas-filled TEPCs (Tissue Equivalent Proportional Counters) and solid-state detectors.
A common property is that the energy imparted by the incident radiation in the detector is converted into a measurable signal, which amplitude is proportional to the energy imparted. Each different detector has its advantages and limitations when investigating microdosimetric spectra.

3.1 Tissue Equivalent Proportional Counters

In this thesis the performances of a cylindrical mini-TEPC (Tissue Equivalent Proportional Counters) under different irradiation conditions are investigated. Mini-TEPCs are miniaturized gas-filled proportional counters, simulating tissue volumes of micrometric size and density of $1 g/cm^3$ by means of a tissue-equivalent gas at low pressure. The mini-TEPC under investigation was developed years ago at the LNL-INFN laboratories specifically for radiation therapy applications.
The gas is enclosed in a cavity surrounded by cathode walls and including a central anode wire. The energy deposition in the counter sensitive volume (SV) ionize the atoms of the filling gas, then the produced electrons drift towards the anode and are then amplified through a phenomenon of gas multiplication. The collected charge is then converted into a voltage pulse, typically by means of a charge sensitive preamplifier.
The pulse amplitude deriving from a given energy deposition event varies according to the gas amplification factor, determined by the voltage difference between the cathode and the anode. This must be chosen in order to work in the region of true proportionality, where the collected charge is proportional to the number of original ion pairs created by the incident radiation [51].

Simulation principle The mini-TEPC SV has millimetric dimensions and the detector operation relies on a "scaling" procedure based on the equality between the mean imparted energy in the gas-filled cavity of the TEPC and that in the simulated tissue site. The mean imparted energy in the two volumes is approximated by the energy released by charged ions in the CSDA approximation, where the Bethe-Bloch Equation 1.1 can be used.
Indicating with ΔX_t and ΔX_g the characteristic dimensions of the tissue volume

and gas cavity respectively, the equality of the imparted energy becomes

$$\left(\frac{S}{\rho}\right)_t \rho_t \Delta_t = \left(\frac{S}{\rho}\right)_g \rho_g \Delta_g, \tag{3.1}$$

where $(S/\rho)_t$ and $(S/\rho)_g$ are the mass stopping powers in tissue and gas respectively and ρ_t and ρ_g their densities.
The equation can be further simplified if the tissue and the gas have an identical atomic composition, so that $(S/\rho)_t = (S/\rho)_g$, assuming that mass stopping powers are density-independent. With these constraints, the simulation of a given tissue size ΔX_t just requires to properly choose the gas density, according to

$$\rho_t \Delta X_t = \rho_g \Delta X_g. \tag{3.2}$$

In operative conditions the parameter to be changed is the gas pressure, which is given by

$$P_g = \frac{\rho_g}{M_g} RT, \tag{3.3}$$

where M_g is the molar mass of the gas or mixture, $R \approx 8.31 Jmol^{-1}K^{-1}$ is the ideal gas constant and T is the gas temperature.

Tissue equivalent materials In order to properly apply the simulation principle, the density variation at the interface between the counter walls and the filling gas should not affect the energy deposition from the primary particle. According to Bragg-Gray cavity theory [41] states that the fluence of secondary particles from a given incident radiation will be constant and independent on density variations if homogeneity between the counter walls and the gas is achieved. For this reason the counter walls must be made of tissue-equivalent materials, the most common being A-150 TE plastic, which composition is very close to the standard muscular tissue, as seen in Table 3.1. The greater amount of carbon is necessary to ensure its electrical conductivity properties.

TE-Solid	H	C	N	O	F	Na	Mg	P	S	K	Ca
ICRU muscle (ICRU, 1964)	10.2	12.3	3.5	72.9	-	0.08	0.02	0.2	0.5	0.3	0.007
A-150 plastic (Smathers et al., 1977)	10.1	77.6	3.5	5.2	1.7	-	-	-	-	-	1.8

Table 3.1: Elemental composition of standard ICRU muscle-equivalent tissue and A-150 plastic [42], expressed as a percentage in weight.

However the density variation can lead to the scattering of the primary particle, and branches of secondaries and tertiaries will be generated departing from the primary particle track. This causes a perturbation in the energy deposition, causing ionizations which in general will not take place in the direction of the original track. These phenomena are called "wall-effects" and they can distort the experimental microdosimetric distributions [42]. They are more significant for electrons (more subject to deflections in the medium), they are also more relevant with increasing cavity size, and finally depend on the particle "quality" (namely nuclear charge Z, velocity and mass). An example of wall effect is shown in Figure 3.1, where a curved track experiments distortions at the interface between two materials with different

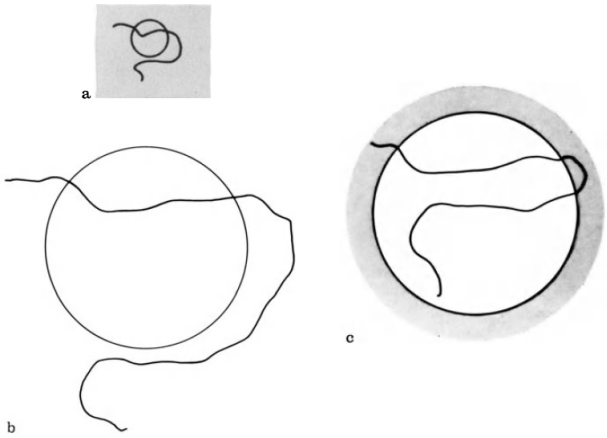

Figure 3.1: Schematic representation of a wall effect, where the curved track in the high density (a) and low density (b) materials can be distorted at the interface between the two (c), resulting in a distorted spectrum of released energy within the site [40].

densities.
The gas mixture to be employed is chosen to give the best approximation to the tissue composition and to provide homogeneity with the walls. Another requirement is to avoid the presence of electronegative elements, since in this case the electrons generated in ionizations would not be free to form the electrical avalanche, affecting the counting characteristics of the gas. The two main filling gases are propane and methane based tissue-equivalent gases, which are described in Table 3.2.

Gas-mixture	H	C	N	O	CH_4	C_3H_8	CO_2	N_2
Methane-TE (Rossi and Failla, 1956)	10.2	45.6	3.5	40.7	64.4	0	32.5	3.1
Propane-TE (Srdoc, 1970)	10.3	56.9	3.5	29.3	0	55	39.6	5.4

Table 3.2: Elemental and molecular composition of standard muscle-equivalent gas mixtures [42], expressed as a percentage in weight.

Compared to the methane-based mixture, the use of propane-TE presents better counting characteristics and it is more similar to the A-150, thus it is preferred.
In this work the mini-TEPC has been filled with pure propane. This has a higher stability over time and has higher gain characteristics compared to the propane-TE mixture. The drawback is that pure propane is not tissue equivalent. For this reason the material equivalence for the different filling gases of the TEPC is achieved by investigating the equivalence of the ionization distributions inside the gas cavity, which are later converted into energy imparted distributions. A paper by Chiriotti et al. [43] showed that in order to have the same ionization spectra of the TEPCs filled with TE-propane the density of pure propane must be reduced by a factor of 0.75 as compared with the TE-propane density.

Gas properties The proportionality constant between the number of ionizations produced by the radiation and the collected charge is determined by a gas characteristic, called gas gain.
It is defined as the mean number of electrons collected at the anode wire per primary ion pair produced by the ionizing particle [42]. It depends on the geometry of

the sensitive volume, the voltage difference between the anode and the cathode, the type of the filling gas and the pressure inside the detector volume.
The general formula for the gas gain is linked with the Townsend first-ionization coefficient α_t, that quantifies the number of ion pairs per unit length generated by one primary electron, through

$$n(d) = n_0 e^{\alpha \cdot d}, \tag{3.4}$$

where d is the distance traveled by the electron and n_0 is the number of primary electrons.
The relationship between the gas gain and the ionization coefficient is

$$ln(G) = \int_{r_a}^{r_c} \alpha_t dr, \tag{3.5}$$

where r_c and r_a are the cathode and anode radii respectively, while dr is an elemental radial distance in the direction of the electric field.
Qualitatively the first ionization coefficient decreases with a decreasing electric field and with a increasing gas pressure, since the smaller electronic mean-free path prevent electrons to reach the energy to cause secondary ionizations. The α_t coefficient thus depends on the reduced electric field S, that in cylindrical geometry is

$$S = \frac{E}{N} = \frac{1}{r} \frac{\Delta V}{ln(r_c/r_a)} \cdot \frac{1}{N}, \tag{3.6}$$

where N is the gas number density and ΔV is the voltage difference between the anode and cathode.
For a uniform electric field the reduced Townsend coefficient α_t/N is a function of the reduced electric field only [44], while for non-uniform electric fields the dependence on the reduced voltage $K = \Delta V/ln(r_c/r_a)$ must also be included [47].
This description of the gas gain has been studied in a work by Colautti et al. [47], and is valid for reduced electric field values exceeding $S^\star = 850 \cdot 10^{-17}\ Vcm^{-2}$, such that reached in mini-TEPCs. In this approach the reduced gas gain is described as

$$\frac{ln(G)}{K} = \int_{S_c}^{S_a} \frac{\alpha_t}{N}(S,K) \frac{1}{S} dS, \tag{3.7}$$

where the reduced Townsend coefficient α_t/N is calculated through

$$\frac{\alpha_t}{N} = \frac{L}{V_i} exp(-MS^{m-1}), \tag{3.8}$$

where V_i is the effective ionization potential of the gas, L and m are gas parameters and M is a function of the reduced voltage

$$M = L \frac{K}{V_i} \Big[exp\Big(\frac{V_i}{K}\Big) - 1 \Big]. \tag{3.9}$$

With this expression of α_t the reduced gas-gain becomes

$$\frac{ln(G)}{K} = \frac{L}{MV_i(1-m)} \Big[exp(-MS_a^{m-1}) - exp(-MS_c^{m-1}) \Big], \tag{3.10}$$

which is known as the *gradient-field model*.
The gas parameters are determined through fitting of the gas-gain data and once known they allow to determine the gas gain as a function of the pressure and the applied voltage. In Figure 3.2 it is presented the variation of the gas gain for a mini-TEPC as a function of the distance from the anode wire.

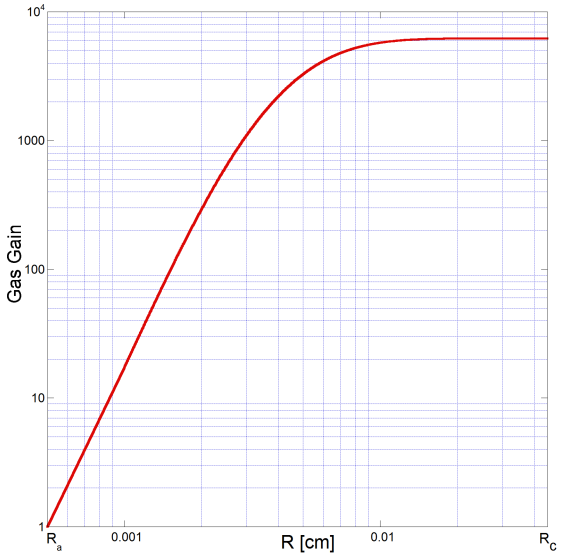

Figure 3.2: Gas gain calculated with the gradient-field model of Equation 3.10 using a mini-TEPC with cathode diameter 0.9 mm, anode diameter 10 μm, filled pure propane at 454 $mbar$ pressure, with an applied voltage difference of 800 V. The gas gain is almost constant up to a distance of about 100μm from the anode wire, while below this value it is dependent on the position. In this particular case the region of constant electronic avalanche occupies approximately in the 98.8% of the SV.

Considerations on mini-TEPCs operation During operations it is fundamental that the multiplication zone is confined near the anode wire, in fact if the avalanche region is small enough, the gas multiplication does not depend on the point of formation of the primary ion/electron pairs.
The gas gain should be increased to achieve a fixed gain value, for example by decreasing the pressure in the cavity. However, lowering the pressure enlarges the fraction of the detector SV occupied by the avalanche, namely the region where the gas gain is dependent on the primary ionization position. This effect leads to a loss in energy resolution of the system. For this reason there is a limit on the pressure or, equivalently, the site size that can be simulated.
The gas multiplication increases quickly with the applied voltage, thus the proportional counter must be operated with very stable voltage supplies.
A condition that has to be avoided while working with mini-TEPCs is the distortion of the electric field inside the counter arising from a build-up of space-charge [51]. This effect is most prominent near the anode wire, where most multiplication takes place. The electrons are quickly collected leaving behind the positive ions, which, due to their greater masses, move about 1000 times more slowly and can cause an electric field screening effect. In this situation the avalanches are not independent and the energy resolution can be affected. In addition this effect arises when inspecting high-rate radiations. For this reason the gas gain must be kept as low as possible, also taking into account the signal to noise requirements.

3.2 Experimental Setup

3.2.1 Mini-TEPCs

The detector used is a cylindrical counter which SV has millimetric dimensions. The small size allows to obtain a high spatial precision and to reduce the pile-up effects that arise when high-rate particle beams are inspected, due to the small number of intercepted particles. In addition, the small diameter allows to house them inside a 8-French cannula for minimally invasive surgery, opening the possibility of an in vivo monitoring of the therapeutic radiation fields.
The performances of a new mini-TEPC designed at the Legnaro National Laboratories were studied.
The AMiCo 6 detector (Adrotherapy Mini Counter) is housed in a cylindrical aluminum shield, with an external diameter of 2.7 mm. Its sensitive volume is approximately a right cylinder with a diameter of 0.9 mm. Two cylindrical cavities are placed at the two ends of the SV (diameter of 150 μm and height of 200 μm) to avoid the potential damage caused by the electronic avalanche to the insulating material surrounding the anode wire. The anodic wire which traverses the sensitive volume is made by gold plated tungsten and its stretching is maintained by means of a spring. Its diameter is 10 μm. The cathode is made of a A-150 plastic, which composition is described in Table 3.1. The electrodes isolation is provided by means of an insulating plastic Rexolite 1422 surrounding the cathode and part of the anode wire.
The sensitive volume has been designed to avoid the perturbation of the electric field inside the cavity that can occur when high-LET radiation are inspected, since the large yield of the positive ions produced can lead to a polarization of the insulating materials surrounding the cavity [49]. The technical design of the detector is not presented due to patenting reasons. Figure 3.3 shows a scheme of a previous detector AMiCo 3 which is identical to the AMiCo 6 detector, apart from the shape of the SV.

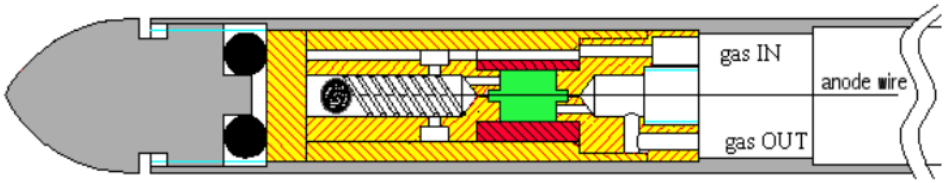

Figure 3.3: Scheme of the AMiCo 3 detector, the green part represents the sensitive volume, the red part is the cathode and the yellow part is the insulating plastic. On the right the pipes for the gas entrance and exit are indicated.

The size of the sensitive volumes of the detector allows to work with intense beams, where the presence of pile-up effects could distort the microdosimetric spectra. In particular, if the minimum time required by the electronics to discriminate a signal is τ, the probability that two different signals will be discriminated is given by [51]

$$P = e^{-\Phi A \tau}, \tag{3.11}$$

where Φ is the flux of particles and A the section of the detector intercepted by the flux of particles. This probability thus decreases with increasing detector section, for a given particle flux. Considering for example a typical flux of therapeutic protons of 10^7 $cm^{-2}s^{-1}$ and a typical shaping time of 250 ns, a commercial spherical

TEPC by Far West Technology, of 1.27 cm in diameter, corresponds to a probability $P = 4\%$, while for the mini-TEPC analyzed in this thesis this probability reaches $P = 98\%$.
The detector is connected to an aluminum box housing the preamplifier, the connections to the gas circuit (described in Section 3.3), the electrical connections for the high (cathode and anode) and low (preamplifier) voltage supply and a sensor to monitor the internal pressure in the detector SV, which full scale range is 1000 $torr \approx 1333$ $mbar$.
A picture of the detector together with the electrical connections is shown in Figure 3.4.

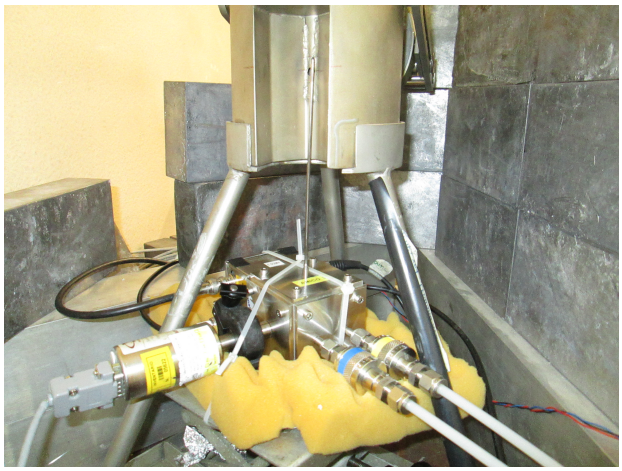

Figure 3.4: Picture of the AMiCo 6 detector, with the gamma irradiator where radioactive sources can be placed during measurements. The hole facing the detector has a diameter of about 6 mm.

3.3 Gas System

For a correct TEPC operation, first a high vacuum level has to be provided to clean the counter (typically $10^{-5} \div 10^{-7}$ $mbar$). This operation must be performed for a sufficiently long time (e.g. two days) to ensure that a steady vacuum condition has been achieved.
After that, the gas mixture can be inserted in the detector cavity. It is not possible to ensure the purity of the gas mixture over time, since gas absorption or degassing phenomena can take place. For example the walls made of TE plastic can adsorb water vapor, releasing electronegative gases. The constancy of the gas mixture is ensured by continuously flowing the gas in the counter, which can be achieved by a feedback-pumping system. This is fundamental to ensure the reproducibility of the measurements and of the results.
The system to provide the vacuum and the gas to the detector is sketched in Figure 3.5.
The high level of vacuum required is provided by means of a turbo pumping station, type HiCube 80 by Pfeiffer Vacuum, which maintains a stationary vacuum level of approximately $10^{-5} \div 10^{-7}$ $mbar$. During the pump operation all the valves shown in Figure 3.5 are opened, apart from the gas valve.
After the vacuum stage, the gas valve is opened and the gas circuit is fed at 10^3 $mbar$. The gas flow inside the counter is controlled by an electronic module, called Mass

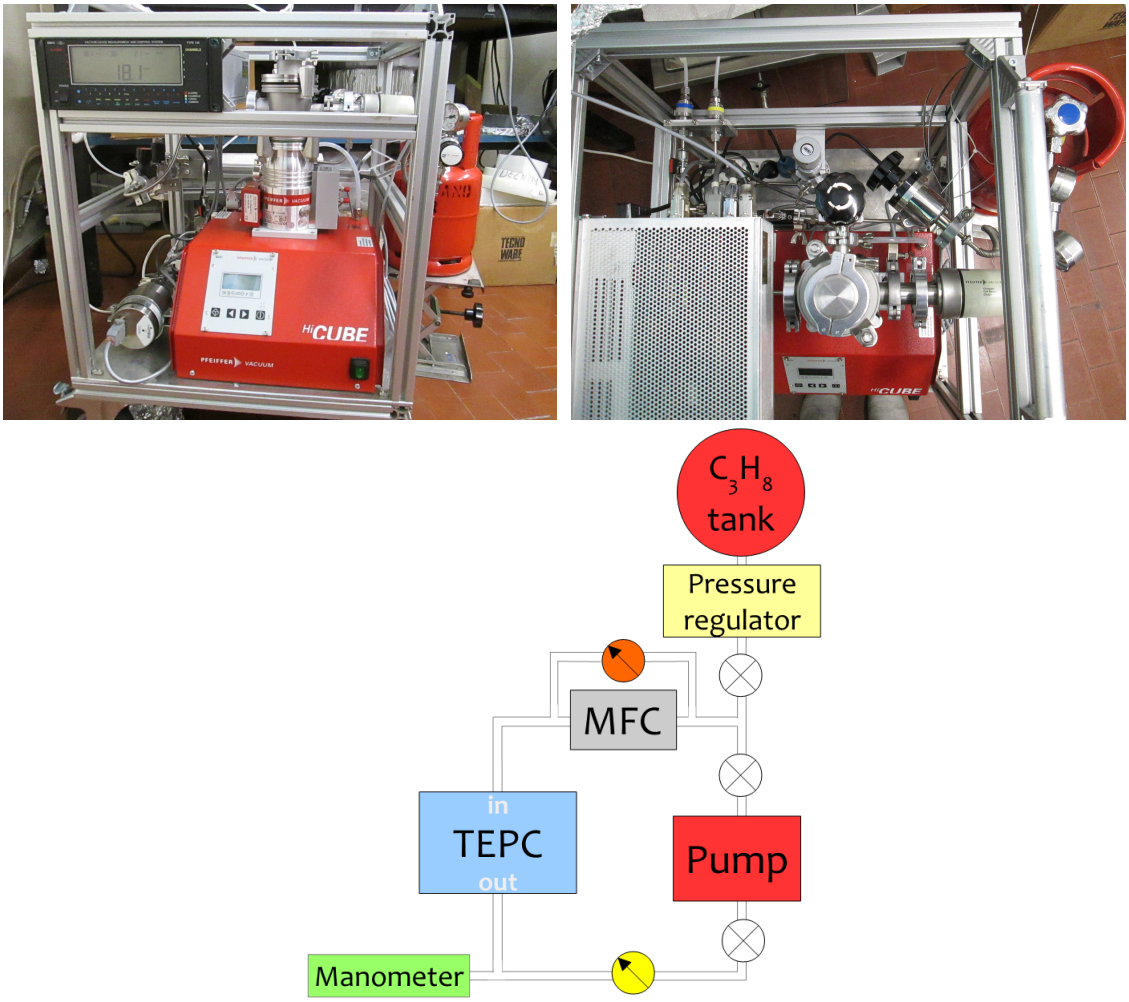

Figure 3.5: Pictures and schematic drawing of the vacuum and gas-flowing system. The C_3H_8 flow is controlled by the MFC module, placed right before the TEPC input. The manometer placed downstream of the detector regulates the opening of the yellow valve, which controls the gas exit.

Flow Controller (MFC). The gas pressure in the detector is maintained to the desired value by means of an an electric valve which regulates the gas exit, which is controlled by a manometer placed downstream of the detector. The detector steady pressure value can be set on the front panel of an electronic module, together with the steady value of the gas flux, which is normally set to 4 cc/min.

3.4 Electronic Chain

The setup used to process the output signals from the detectors is sketched is Figure 3.6.
The detector is coupled to a charge sensitive preamplifier, which output is sent in parallel to three different shaping amplifiers, carrying out the gaussian filtering of the signals, depending on the shaping time set in the front panel. These amplifiers have different gains in order to approximately cover 4 or 5 orders of magnitude of the input signal. The amplifier outputs are sent to three multichannel analyzers that digitize the voltage pulses. Their output is sent via a SCSI-bus to a PC, to

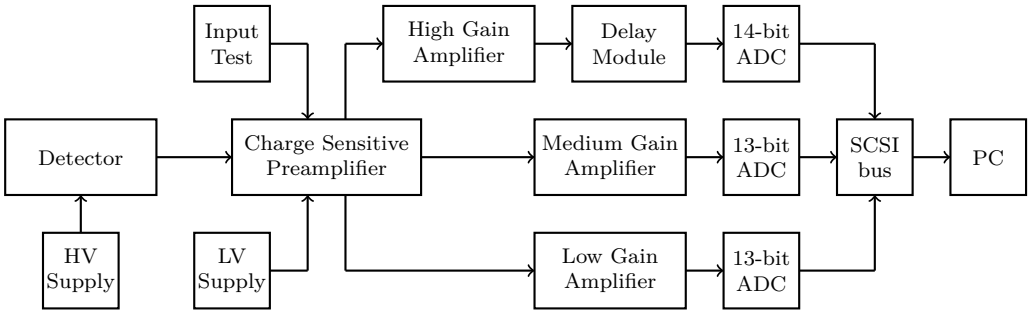

Figure 3.6: Schematic drawing of the electronic chain employed.

acquire the spectra and perform the offline analysis.

Preamplifier The detector is coupled to a charge sensitive preamplifier, which aim is to produce a pulse proportional to the total collected charge Q arising from an event. The rise time of the pulse is chosen as a compromise between the electron and ion collection times in the detector, while the fall time is determined by the time constant of the circuit, product of the feedback resistor R_f and capacitance C_f. The output pulse height of the preamplifier is given by $V_{out} = -Q/C_f$, so the negative signal from the electronic avalanche is converted into a positive output signal.
Due to the high dynamic range of the energy deposition events, the ideal preamplifier should exhibit a linear behavior over 4/5 orders of magnitude and should also have low noise features. The preamplifier is housed within the mini-TEPC in order to minimize its input capacitance, hence the noise.
The preamplifier used during measurements has been specifically built taking into account the low noise requirements for mini-TEPC operation. It has an electronic noise level of approximately $350\mu V$ rms, corresponding to ~ 260 electrons rms, and has a linear behavior over almost 10^5 orders of magnitude corresponding to a range of imparted energies from about $30eV$ to $2MeV$.

Amplifiers The output signal from the preamplifier is fed to three different amplifiers. Their function is to shape the signals that will be send to the ADCs, performins a gaussian filtering. The shaping time can be set in the front panel. During the measurement this has been set to $250ns$, in order to work at high counting rates.
The amplifiers have three different gains, in order to cover the full dynamic range of the preamplifier. The signals are sent in parallel to the amplifiers. The high gain output is gathered after a delay module, preventing the acquisition to be paralyzed when a high-energy signal saturates on this amplifier. The medium- and low-gain amplifier modules have an intrinsic temporal delay of about 3 μs, so an additional delay module is not necessary.

ADCs The gaussians output of the three amplifier is fed to three ADCs having a dynamic range of $0 \div 10V$. The first ADC digitizes low energy signals into $2^{14} = 16384$ channels. The other two are 13 *bit* ADCs ($2^{13} = 8192$ channels) and accept the signals from the medium- and high-LET events. These modules register the number of counts for each energy deposition event.
The spectra recorded exhibit a superposition region, which is necessary to join them to obtain a single microdosimetric spectrum. The maximum event rate which can

be analyzed with this acquisition system is about 100 kHz.

Pulse generator In order to calibrate the electronics, converting the ADC channel number in volts, a precision pulse generator provides a signal simulating the output pulse from the detector. The signal has a finite rise and decay times, which can be set in the front panel of the pulser. A calibration of the electronics can be then performed through a series of precise attenuators, obtaining a correspondence between ADC channels and pulse amplitude. In this way, the linearity of the electronic chain can be tested.

4. Data Analysis

The software used for data analysis was written in C++, with a graphical user interface designed with the Qt framework (qt-project.org).
In the subsequent part the three ADCs with different gains are called low-LET (LL), medium-LET (ML) and high-LET (HL), with reference to the part of the microdosimetric spectrum inspected.
Figure 4.1 shows a flow chart illustrating the main algorithms implemented in the software. Each of the graphs produced can be saved in ".png" format by the user. A "log" containing the analysis output is also produced, and can be saved by the used in ".txt" format.
The software has been used in the measurement shifts with the mini-TEPC described in the following chapters. The short time required for the algorithms execution (few seconds) allows to speed-up the analysis steps, and to have a prompt visual feedback on the validity of the measurement procedure (e.g. to exclude errors in the pulse height calibration or test the constancy of the electronic chain linearity).
For the detailed explanation of the performed operations, the analysis of a ^{137}Cs gamma and a neutron spectra are presented.

4.1 Pulse-height Calibration and Logarithmic Rebinning

The data file with the registered ADC counts can be selected by the user in the main window, together with the work directory that will contain the output files of the analysis. The user can choose the number of ADCs to take into account. Figure 4.2 shows a screenshot of the collected counts due to a neutron source source, where the detected signals fall in the three ADCs.
The pulse height calibration of the spectra is performed through a linear regression of the pulse amplitude data as a function of the ADC channels. As a test input a precision pulser is used, with a series of precise attenuators that can divide the pulse amplitude by the factors $\times 2$, $\times 5$, $\times 10$, $\times 20$, $\times 50$, $\times 100$, $\times 200$, $\times 500$ and $\times 1000$. For each ADC the channel x corresponding to a given pulse is related to the pulse amplitude in mV through the calibration equation

$$y_k[mV] = a_k + b_k \cdot x_k[channels], \tag{4.1}$$

where $k = \{LL, ML, HL\}$. The linear regression algorithm is presented in Appendix A.1. An example of calibration is shown in Figure 4.3 for a test input with 840 mV amplitude.
After the ADC calibration the collected counts in each ADC are rebinned in a logarithmic presentation.
The pulse height abscissa is divided in N decades and B logarithmic intervals per

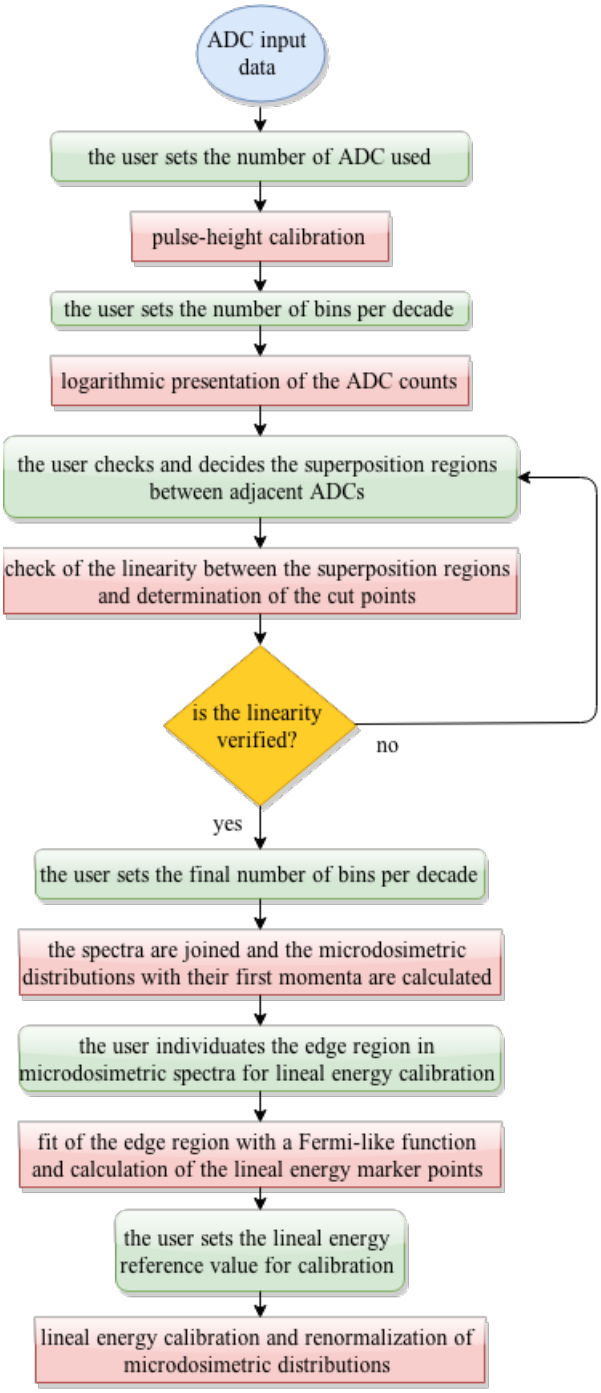

Figure 4.1: Diagram illustrating the analysis steps implemented in the software. The green rounded boxes show the user interactions while the red boxes present the seuence of performed operations. The details on the implemented algorithms are discussed in more detail in the text.

decade, which can be set by the user.
The minimum value of pulse height to consider y_{min} is also given as input by the user.
Starting from y_{min}, the software searches automatically for the maximum mV value registered by the three ADCs, then calculates the number of decades N, the minimum and maximum exponents on 10 to consider (e_{min}, e_{max}) and the lower limit of

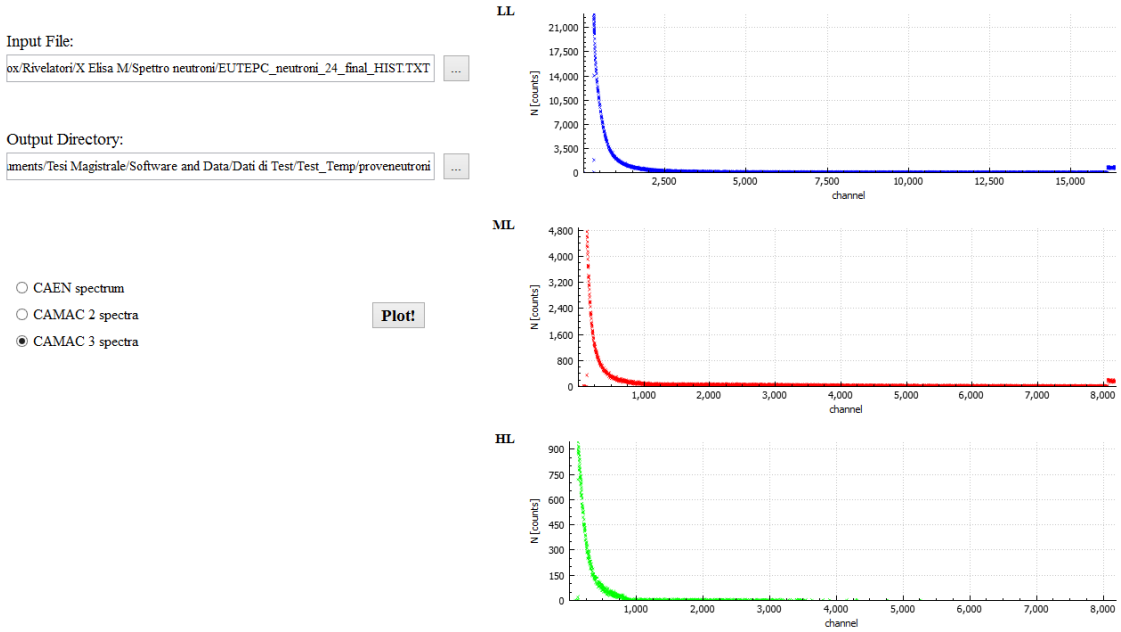

Figure 4.2: Shot of the software plots of the ADC counts registered for a neutron source.

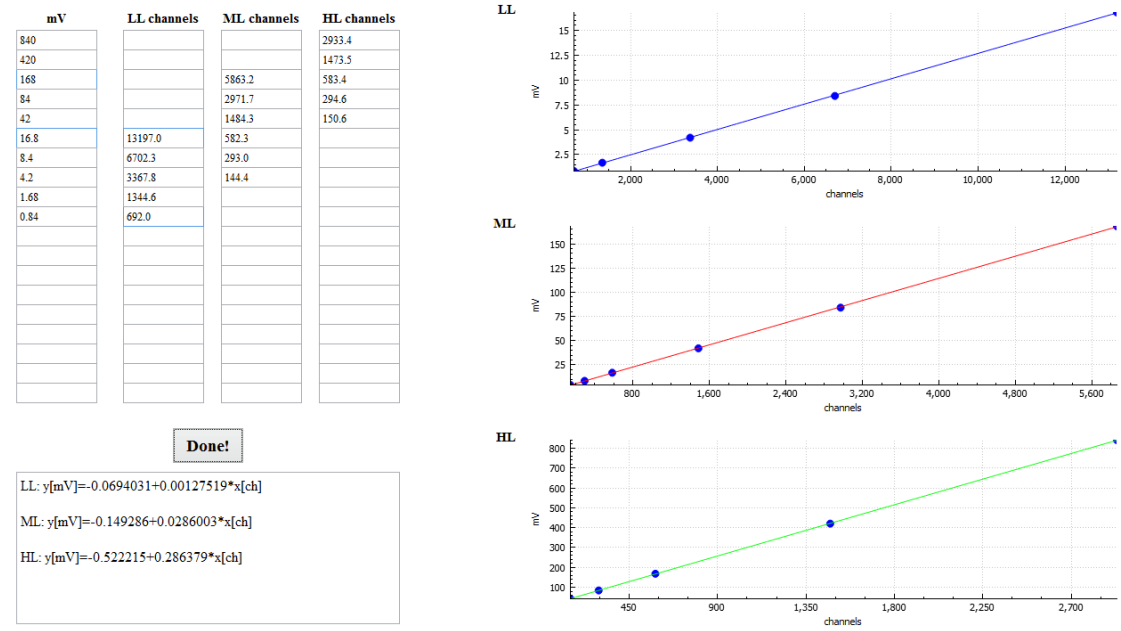

Figure 4.3: ADCs calibration equations using a reference 840 mV pulse amplitude. The channel number corresponding to a given pulse-height is set as input by the user.

each decade

$$y_0^{j=\{0,\dots,N-1\}} = 10^{e_{min}+j}. \tag{4.2}$$

In the decade j, the $k-th$ value of y is calculated as

$$y_k^j = y_0^j 10^{\frac{k-jB}{B}}, \tag{4.3}$$

where k runs from $j \cdot B$ to $(j+1) \cdot B$, namely all the points in the decade.
The widths of the intervals in the full spectrum are then calculated through

$$\Delta y_i = y_i \cdot \left(10^{\frac{B}{2}} - 10^{-\frac{B}{2}}\right), \tag{4.4}$$

where $i = \{0, ..., N \cdot B - 1\}$.
The counts falling in each Δy_i are then averaged, obtaining the rebinned counts N_i.
The corresponding pulse height is set as the middle point of the Δy_i interval.
The new counts are then presented with their density $N(y_i)/\Delta y_i$, as it can be seen in Figure 4.4. The code for calibration and logarithmic rebinning is presented in Appendix A.2.

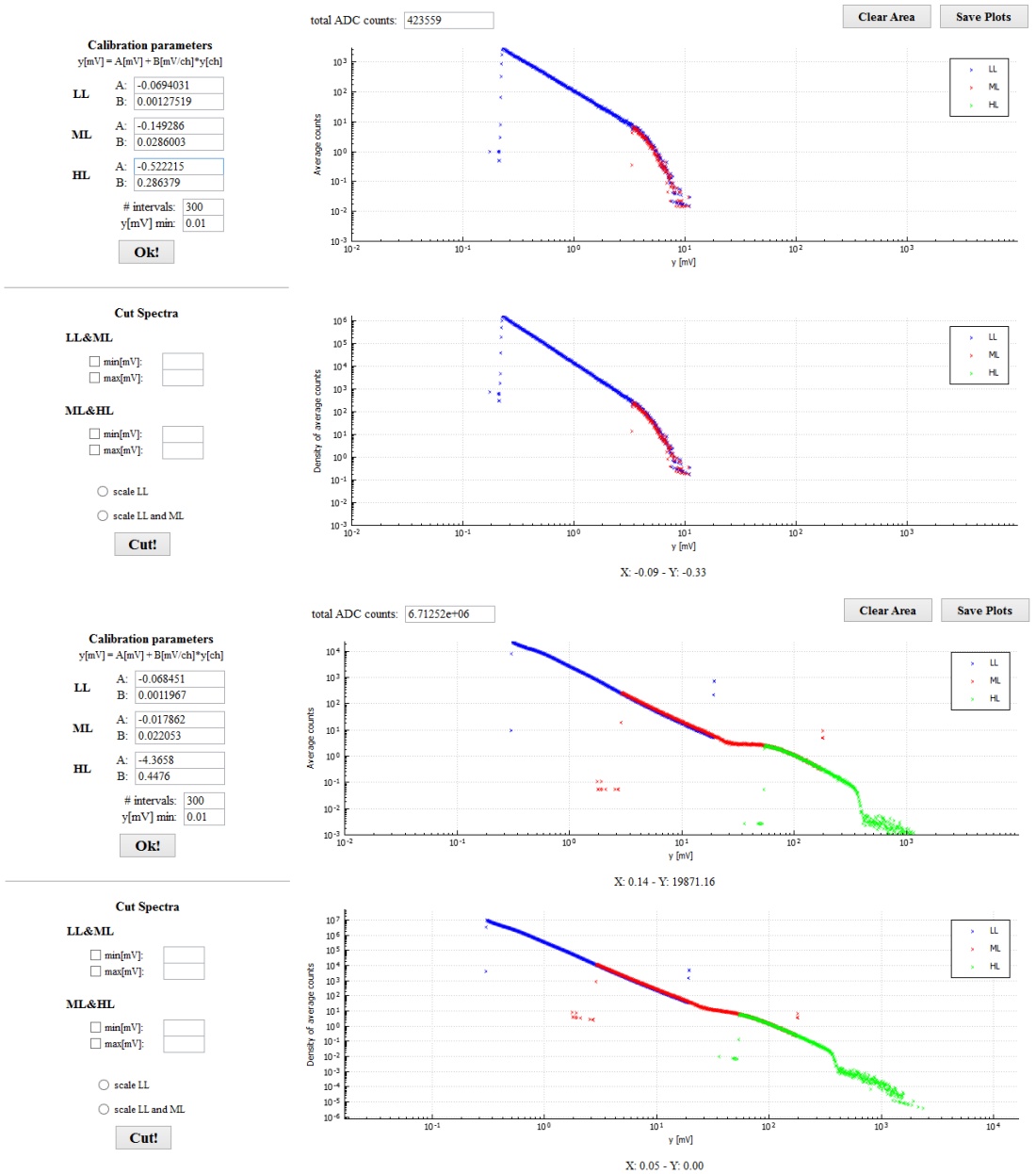

Figure 4.4: ADC counts rebinned with the logarithmic presentation described in Section 4.1 for a ^{137}Cs (upper figure) and a neutron source (lower figure). On the left the calibration equations are shown.

4.2 Superposition Regions and Determination of the Cut Point

The next step consists in joining the ADC spectra. The plots obtained from the previous analysis step, are used to identify the superposition regions between adjacent ADCs. Their lower and upper limits can be selected through a marker, as shown in Figure 4.5.

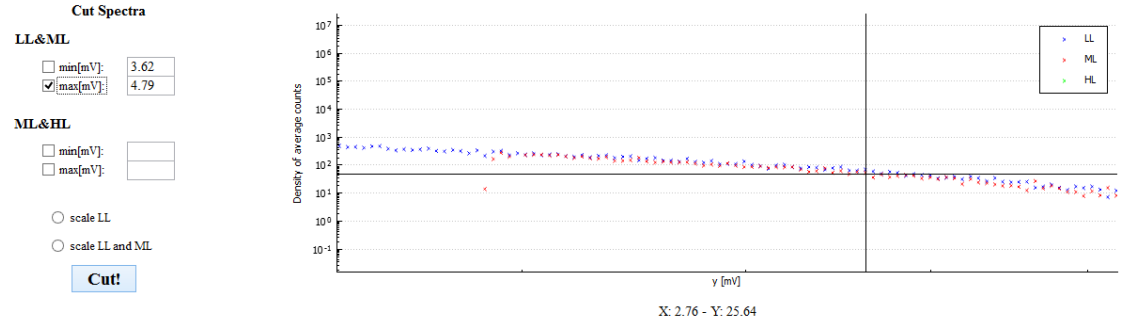

Figure 4.5: Region of superposition of the low- and medium-LET spectra from a ^{137}Cs source. The marker positions is automatically detected and stored in the forms on the left side of the figure.

The logarithmic data corresponding to a region of superposition are fitted using the linear regression algorithm in Appendix A.1. The linearity of the superposition region is checked by calculating the compatibility coefficient λ of the slopes, e.g. for the LL and ML superposition

$$\lambda = \frac{|b_{LL} - b_{ML}|}{\sqrt{\sigma^2_{b_{LL}} + \sigma^2_{b_{ML}}}}. \tag{4.5}$$

The maximum acceptable value of lambda is here set to $\lambda = 2$, above this value the two superposition regions are not considered parallel. The user can repeat the compatibility check by choosing a new superposition region, or can discard the input data.
After the compatibility check, the cut point is calculated. For its determination the relative difference d_i between the counts N_i of the two data sets in each lineal energy interval Δy_i is evaluated through

$$d_i = \frac{N_i^{ML} - N_i^{LL}}{N_i^{LL}}, \tag{4.6}$$

together with its uncertainty, given by

$$\sigma(d_i) = \frac{1}{N_i^{ML}} \sqrt{\sigma^2_{N_i^{LL}} + \left(\frac{N_i^{LL}}{N_i^{ML}}\right)^2 \sigma^2_{N_i^{ML}}}. \tag{4.7}$$

The weighted mean of the differences $\bar{d}$ and the sample variance σ_S are then calculated, through

$$\bar{d} = \sum_{i=1}^{N \cdot B} \frac{d_i}{\sigma^2(d_i)} \Big/ \sum_{i=1}^{N \cdot B} \frac{1}{\sigma^2(d_i)}, \tag{4.8}$$

and

$$\sigma_S = \sum_{i=1}^{N \cdot B} (d_i - \bar{d})^2 \Big/ N \cdot B - 1. \tag{4.9}$$

The variance contribution at each lineal energy value is used to determine the cut point, which is chosen as the central point in the region exhibiting the minimum variance. Figure 4.6 shows an example of junction between the low- and medium-LET spectra from a ^{137}Cs source. The code implementing these operations is presented in Appendix A.3.

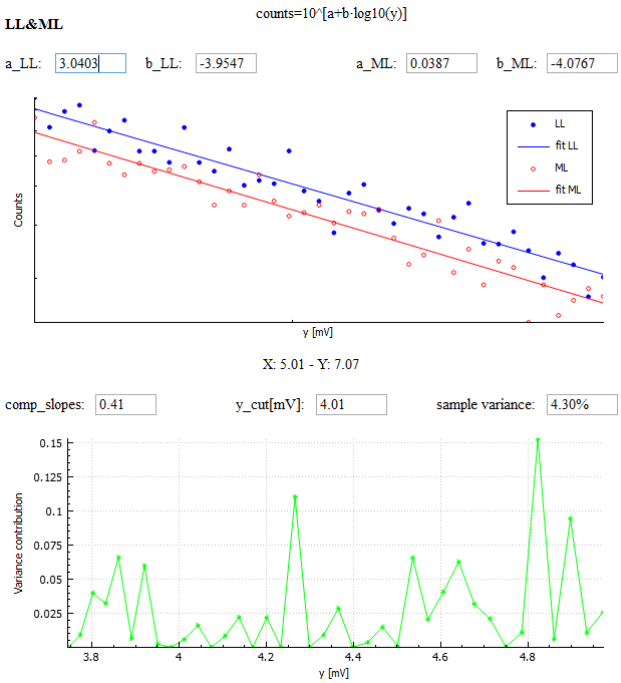

Figure 4.6: Linear fit of the low- and medium-LET data in the superposition region, for a ^{137}Cs source (upper figure) and the relative variance contribution of the differences between data (lower figure). The region of minimum variance in this particular case shows a minimum at about 4 mV.

4.3 Microdosimetric Spectra and Uncertainties

The cut points allow to join the different spectra and to obtain a single spectrum, by using a number of user-specified intervals per decade. This is usually set equal to 60. In fact, when greater values are used the data fluctuations, which can arise for example from a spectrum acquired with poor statistics, become relevant. On the other hand, if the number of intervals is too small there is a loss on the lineal energy resolution of the microdosimetric spectra.
The number of counts $N(y_i)$ in each logarithmic interval Δy_i is divided by the width of the bin, obtaining the normalized density of counts $n(y_i)$.
The width of the bins is constant in the logarithmic presentation, in fact

$$\Delta(log_{10}y) = log_{10}(y_i) - log_{10}(y_{i-1}) = \frac{1}{B}. \tag{4.10}$$

. The logarithmic presentation of the frequency distribution requires

$$\sum_{i=y_0}^{y_{max}} f(y_i)\Delta y_i = \frac{ln(10)}{B} \sum_{i=y_0}^{y_{max}} y_i f(y_i), \tag{4.11}$$

which means that the ordinate is multiplied by the lineal energy size in the semi-logarithmic representation. In the logarithmic presentation $f(y_i)$ is the probability density of the occurrence of the y_i value which has been counted $N_i = n(y_i)\Delta_i$ times, and it is given by

$$f(y_i) = \frac{n(y_i)}{\sum_{y_0}^{y_{max}} n(y_i)\Delta y_i}. \tag{4.12}$$

The same holds for the dose distribution

$$\sum_{i=y_0}^{y_{max}} d(y_i)\Delta y_i = \frac{ln(10)}{B} \sum_{i=y_0}^{y_{max}} y_i d(y_i). \tag{4.13}$$

The weighted probability density of the y_i value is calculated as

$$d(y_i) = \frac{y_i n(y_i)}{\sum_{y_0}^{y_{max}} y_i n(y_i)\Delta y_i}. \tag{4.14}$$

Finally, the frequency-averaged and the dose-average lineal energy values are then calculated through

$$\bar{y}_F = \sum_{y_0}^{y_{max}} y_i f(y_i)\Delta y_i, \tag{4.15}$$

and

$$\bar{y}_D = \sum_{y_0}^{y_{max}} y_i d(y_i)\Delta y_i. \tag{4.16}$$

As for the uncertainties on the calculated data, the standard deviation of the number of counts N_i in each lineal energy interval Δy_i is derived from the Poisson statistics

$$\sigma_{N_i} = \sqrt{N_i}. \tag{4.17}$$

The statistical uncertainty on the frequency density value in the interval Δy_i is calculated following the recommendation of Moro et al. [55]

$$\sigma_{f(y_i)} = \sqrt{\frac{f(y_i)}{\Delta y_i \cdot N_{TOT}}}, \tag{4.18}$$

where N_{TOT} is the sum of all events in the spectrum.
The $\bar{y}_F$ value is calculated with its statistical uncertainty

$$\sigma_{\bar{y}_F} = \sqrt{\sum_{i=0}^{N \cdot B} \left(y_i \Delta y_i \sigma_{f(y_i)} \right)^2}. \tag{4.19}$$

The statistical uncertainty on the dose density value in the interval Δy_i is calculated by recalling Equation 2.4

$$\sigma_{d(y_i)} = d(y_i)\sqrt{\left(\frac{\sigma_{f(y_i)}}{f(y_i)}\right)^2 + \left(\frac{\sigma_{\bar{y}_F}}{\bar{y}_F}\right)^2}. \tag{4.20}$$

Finally, the $\bar{y}_D$ value is calculated with its statistical uncertainty

$$\sigma_{\bar{y}_D} = \sqrt{\sum_{i=0}^{N \cdot B} \left(y_i \Delta y_i \sigma_{d(y_i)} \right)^2}. \tag{4.21}$$

An example of such distributions is shown in Figure 4.7. The code implementing the described algorithms is presented in A.4.

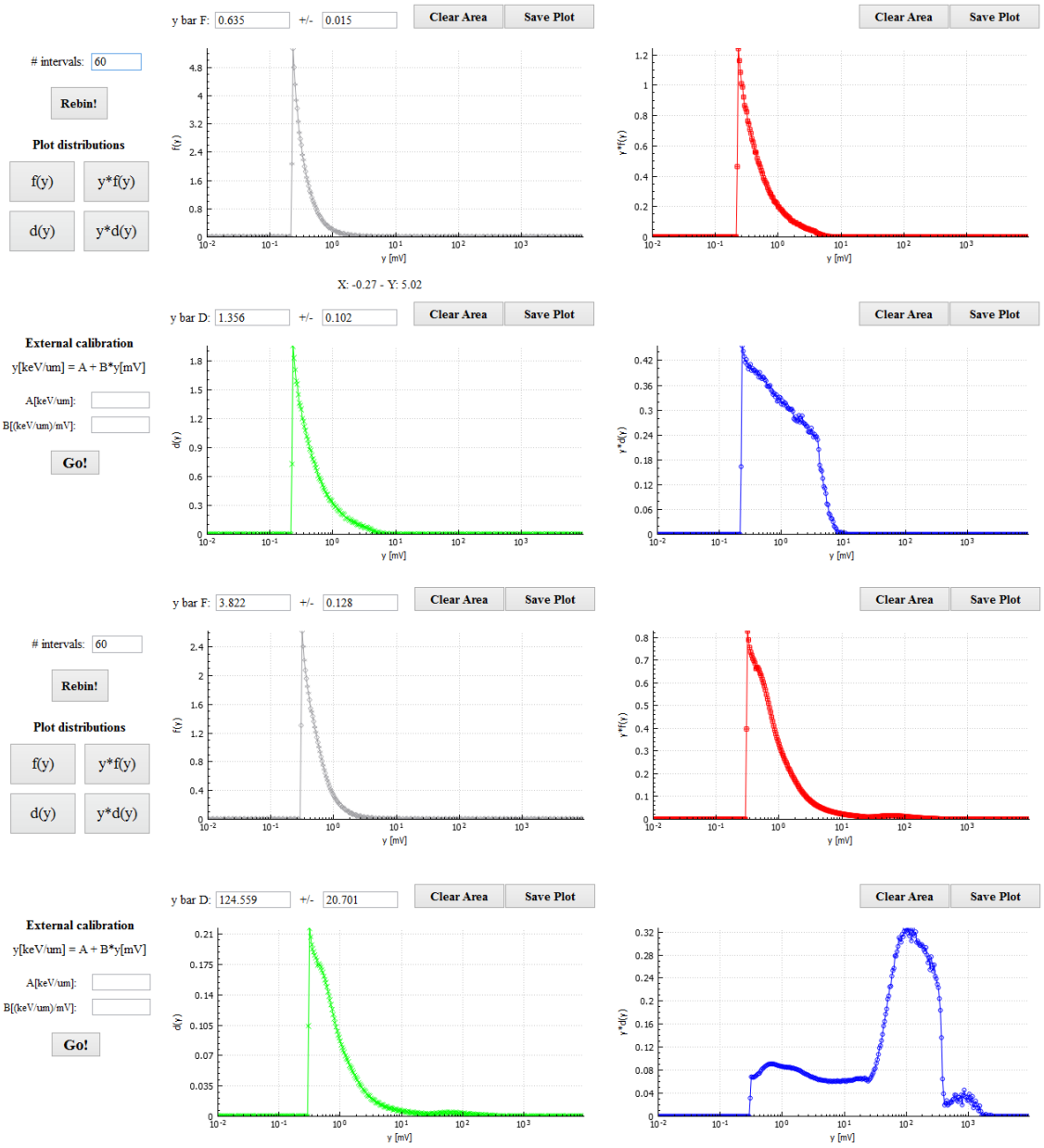

Figure 4.7: Presentation of the frequency and dose density distributions together (upper and bottom right panels) with the calculated $\bar{y}_F$ and $\bar{y}_D$ values, for a ^{137}Cs (upper figure) and a neutron source (lower figure). The differences in the pulse height distribution are more evident in the dose distribution presented at the bottom right, where the contribution of higher pulses is evident for the neutron source.

4.4 Fermi Fit and Energy Calibration

The final step consists in the energy calibration of the spectra. If the calibration parameters are already known they can be inserted directly by the user. Normally microdosimetric spectra in mini-TEPCs are self-calibrated by using the method of the proton or electron edge [56].
This method is based on the identification of a significant marker point in the microdosimetric spectrum to which a well-defined lineal energy value is associated. In

particular, if the microdosimetric spectrum contains a proton or an alpha component (e.g. in a neutron field), this marker point can be found in the so called proton edge or alpha edge. In this region of the spectrum there is a lineal-energy cutoff due to the maximum energy deposition of these particles in the gas-filled cavity of the mini-TEPC. This maximum energy loss E_{max} can be calculated with the energy-range tables, e.g. [59], [60] or [61].
If the proton or alpha components are not present, the electron edge of an external gamma source can be used, although the electron straggling phenomena makes the edge less sharp. In the case of electrons the stopping power decreases monotonically with increasing energy, thus the maximum energy is deposited by the electrons which range exactly matches the diameter of the mini-TEPC sensitive volume (exact stoppers). The corresponding electron energy E_{max} can be found in energy-range tables, e.g. [57] or [58], and the maximum of lineal energy can be found.
In any case, since the mini-TEPCs used are right cylinders with height and diameter equal to D, the mean chord length is $\bar{l} = 2D/3$, thus the maximum of lineal energy is $y_{max} = E_{max}/\bar{l}$. The problem of the correct assignation of this lineal energy value to a given marker point in the microdosimetric spectrum has been described in a work by Conte et al. [56].
The edge region in the $yd(y)$ dose distribution has been experimentally found to be well fitted by a Fermi-like function [56]

$$F(yd(y)) = \frac{A}{1 + exp(B(y - C))}, \tag{4.22}$$

where A is the highest value of the function, C is the position of the inflection point of the function and B related to the slope of the function in the inflection point.
Three different marker values of lineal energy can be recognized in the edge region and are presented in Figure 4.8, showing the electron edge region for a ^{137}Cs gamma source at 1 μm. These are the inflection point itself

$$y_{flex} = C, \tag{4.23}$$

the position of the maximum of the second derivative

$$y_{\partial\partial} = \frac{ln(2 + \sqrt{3})}{B} + C \tag{4.24}$$

and the position of the tangent through the inflection point

$$y_{TC} = \frac{2}{B} + C. \tag{4.25}$$

With reference to Figure 4.8, the marker values are presented in Table **??** for different choices of the fitting intervals.
The value of lineal energy y_{max} is thus assigned to the y_{TC} parameter, which has been proved to be the least affected by variations of the statistics (number of points in the fitting interval) and the various possible fitting intervals.
To perform the fit, the user sets the upper and lower limit of the data set in the edge region by using two markers. The data are then fitted using the least-squares method based on the Levenberg-Marquardt algorithm. For the algorithm implementation the suggestions presented in [62] were adopted. The initial guesses for the parameters

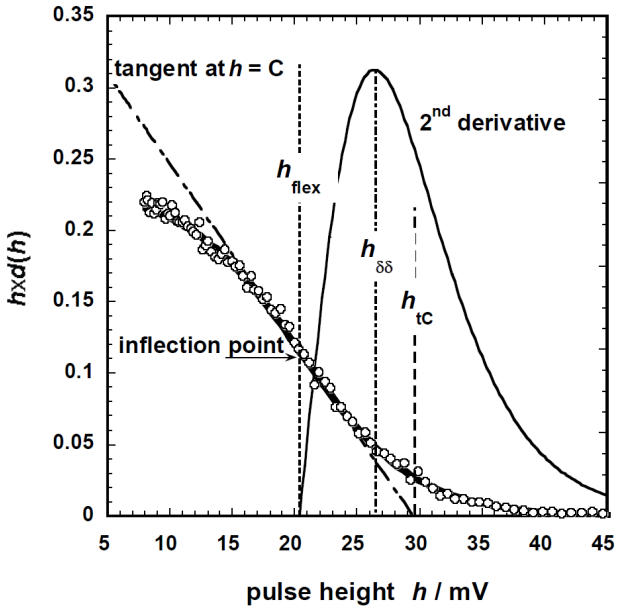

Figure 4.8: Electron-edge region for a ^{137}Cs source source at 1 μm. The open circles are experimental data, the thick line is the Fermi function. The corresponding lineal energy markers are highlighted by the vertical lines, as in [56].

h interval of e-edge region	*A*	*B*	*C*	$\frac{\ln(2+\sqrt{3})}{B}+C$	$\frac{2}{B}+C$
mV		mV^{-1}	mV	mV	mV
6.0 – 60	0.240 ± 0.002	0.208 ± 0.004	20.0 ± 0.1	26.3 ± 0.2	29.6 ± 0.2
6.5 – 60	0.238 ± 0.002	0.210 ± 0.004	20.1 ± 0.1	26.4 ± 0.2	29.6 ± 0.2
7.0 – 60	0.236 ± 0.002	0.213 ± 0.004	20.2 ± 0.1	26.4 ± 0.2	29.6 ± 0.2
7.5 – 60	0.235 ± 0.002	0.214 ± 0.004	20.2 ± 0.1	26.4 ± 0.2	29.6 ± 0.2
8.0 – 60	0.233 ± 0.002	0.217 ± 0.004	20.4 ± 0.1	26.4 ± 0.2	29.6 ± 0.2
8.5 – 60	0.232 ± 0.002	0.218 ± 0.004	20.4 ± 0.1	26.5 ± 0.2	29.6 ± 0.2
9.0 – 60	0.232 ± 0.002	0.218 ± 0.004	20.4 ± 0.1	26.5 ± 0.2	29.6 ± 0.2
9.5 – 60	0.230 ± 0.002	0.222 ± 0.004	20.5 ± 0.1	26.4 ± 0.2	29.5 ± 0.2
10.0 – 60	0.230 ± 0.002	0.221 ± 0.004	20.5 ± 0.1	26.5 ± 0.2	29.6 ± 0.2
Average values	**0.234 ± 0.001**	**0.216 ± 0.002**	**20.32 ± 0.06**	**26.42 ± 0.01**	**29.58 ± 0.01**

Figure 4.9: A, B and C parameters of the Fermi-like function fitting the experimental electron-edge data presented in Figure 4.8, as in [56]. The parameters are obtained by varying the fitting intervals, presented in the left column. The corresponding $y_{\partial\partial}$ and y_{TC} values are also calculated.

are directly calculated by the software.
The procedure gives, after a convergence, the three fit parameters A, B and C, and calculated the corresponding quantities y_{flex}, $y_{\partial\partial}$ and y_{TC}.
The result of the electron edge fit for a ^{137}Cs gamma source is shown in Figure 4.10.
The code is presented in Appendix A.5.
For electrons the dependence of the maximum lineal energy deposition at a given simulated size d in a cylindrical counter filled with TE-propane gas, is described by the formula [56]

$$\frac{y_{e-edge}}{keV/\mu m} = 15.5 \left(\frac{d}{keV/\mu m} \right)^{-0.42}, \tag{4.26}$$

where d is expressed in μm.
For protons and heavier charged particles the maximum stopping power must be

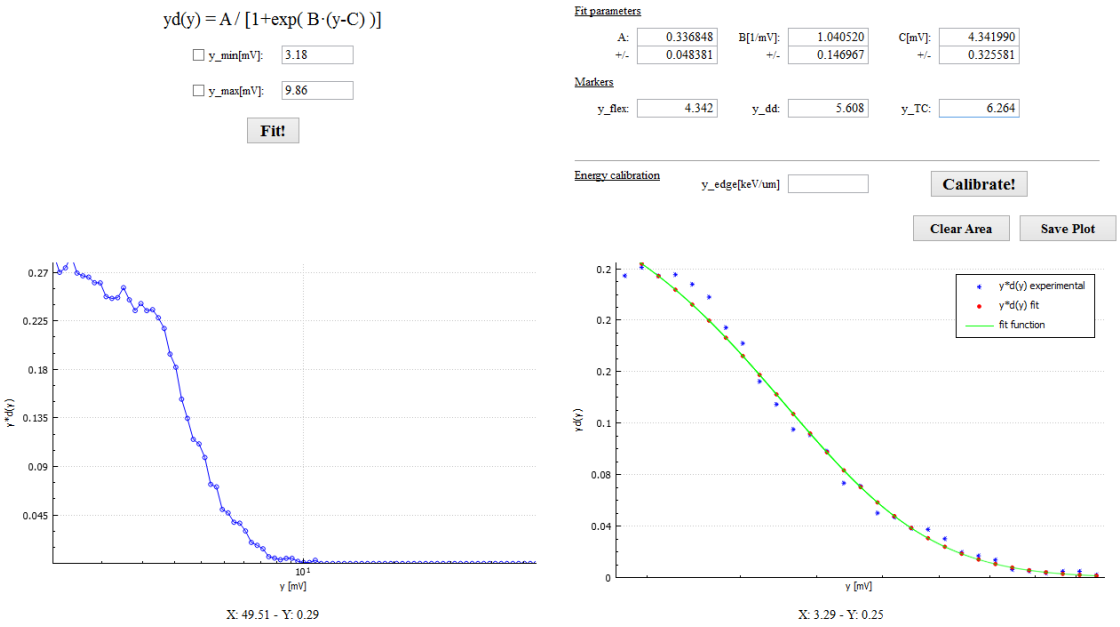

Figure 4.10: Fit with a Fermi-like function of the electron edge region of a ^{137}Cs source. The fitting interval is set in the left graph, where the experimental data are plotted. The fitting parameters with their uncertainties and the calculated lineal energy markers are shown at the upper right. In the graph on the right the fitting Fermi-like function is plotted.

calculated iteratively by employing energy-range tables.
In any case, the user can insert the lineal energy value corresponding to the edge, obtaining the final microdosimetric spectra calibrated in lineal energy.

5. Measurements in low-LET fields

These measurements investigate the AMiCo 6 capability to detect low-LET events. The detector is exposed to a ^{137}Cs source emitting 0.66 MeV γ-rays. The source is housed in a cylindrical lead shield, as in Figure 5.1. The detector sensitive volume is then placed as close as possible to the source.

Figure 5.1: Picture of the AMiCo 6 detector placed in the gamma irradiator housing the radioactive source.

Before the measurements a vacuum level of 10^{-5} mbar has been provided in the whole gas-flowing system.
The filling gas of the detector is pure propane. The gas pressure is set in order to have the same number of ionizations occurring in propane-TE massic sites of 0.3 mg/cm^2, 0.5 mg/cm^2, 1.0 mg/cm^2 and 2.0 mg/cm^2. In particular, the equivalence in the ionization yield prescribes the following relation between the massic sites d in pure and TE-propane [43]

$$d_{C_3H_8-TE}\ [mg/cm^2] = d_{C_3H_8}\ [mg/cm^2] \times 0.75, \tag{5.1}$$

and the pure propane density must be scaled accordingly.
Table 5.1 shows the C_3H_8 pressure corresponding to a massic tissue site d_t ($\rho_t = 1\ g/cm^3$), the corresponding propane massic site $d_{C_3H_8}$, at a temperature of $T = 293\ K$.
The value of 0.3 μm represents the lowest size measurable with the mini-TEPC, in fact by lowering the gas pressure the gas gain increases, but at the same time the

d_t [mg/cm^2]	$d_{C_3H_8}$ [mg/cm^2]	P_g [mbar]
0.3	0.225	136
0.5	0.375	227
1.0	0.75	454
2.0	1.5	908

Table 5.1: Pressure of pure propane and simulated tissue size, calculated with Equation.

multiplication region becomes wider, due to the increase in the mean free ionization path of the produced electrons. This causes an increasing probability that the primary ionization events are located outside the drift region, where the multiplication factor of electrons depends on the distance of the primary ionization point from the anode. The lack of uniformity in the multiplication phenomenon inside the counter causes the decrease in the energy resolution of the system. This is shown in Figure 5.2, where the avalanche extension is presented as a function of the simulated size, when other parameters are kept constant.

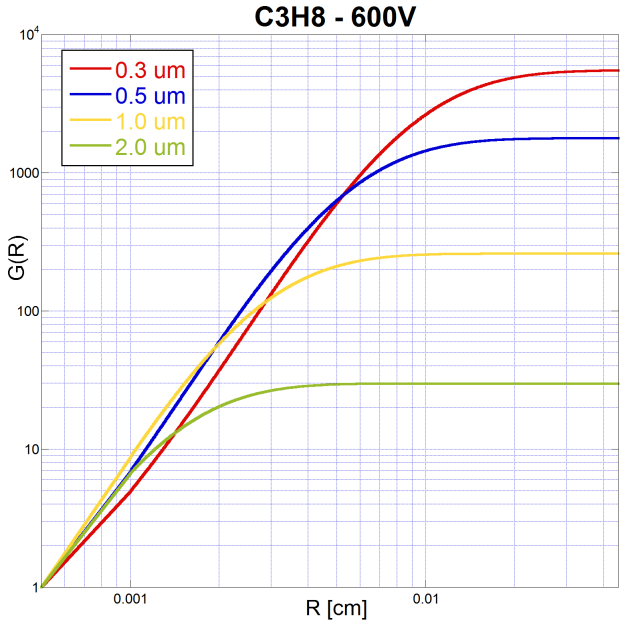

Figure 5.2: Gas gain calculated with the gradient-field model, as a function of the distance from the anodic wire, at different simulated site sizes in pure propane, for a potential difference of 600 V. The avalanche extension with respect to the counter volume is approximately 0.4% for 2.0 μm, 1.9% for 1.0 μm, 7.7% for 0.5 μm and 19.7% for 0.3 μm.

During operation the detector was secured to a support frame to ensure a steady position during the measurements. In fact small movements of the central anode wire can induce microphonic noise at the input of the preamplifier.
At each pressure different voltages were applied between the anode and the cathode. The lowest potential difference for each size is the minimum required to discriminate the detector signal from the noise level.
The ADC calibration has been performed by using a tail pulse from the precision pulser simulating the detector signal, with the characteristics shown in Table 5.2.
Particular attention has been paid to the correct evaluation of the offset in the calibration equation of the high-gain ADC. This parameter has been proved to be

Amplitude	Rate	Rise time	Fall time
890 mV	2.5 kHz	200 ns	500 μs

Table 5.2: Settings of the test input signal to calibrate the electronics.

crucial since when it strongly differs from zero it can lead to a strong deformations in the microdosimetric spectra [54].
The linearity of the electronic chain was tested, and the overlap between the different electronic chains was optimized by properly choosing the amplifier gains. In order to work with the vary intense therapeutic beams, the shaping time was kept as low as possible to reduce potential pile up effects. In these test measurements it was thus set to 250 ns, which is the minimum value settable in the amplifier modules. The presence of a correct pole-zero cancellation was also checked.
The electronic noise level at the preamplifier output has been monitored by means of an oscilloscope, model Tektronix TPS 2012B. During the measurements it ranged in the interval $300 \div 700\ \mu V$.
The microdosimetric spectra are calibrated in energy by using the electron-edge method described in Section 4.4. The values of the electron edge, calculated with Equation 4.26 are presented in Table 5.3.

d_t [mg/cm^2]	y_{e-edge} [keV/μm]
0.3	26.01
0.5	20.88
1.0	15.5
2.0	11.51

Table 5.3: Lineal energy corresponding to the electron edge at different tissue equivalent massic sites, calculated with Equation 4.26.

5.1 Low-LET spectra

The detailed electronic chain employed is presented in Figure 5.3.

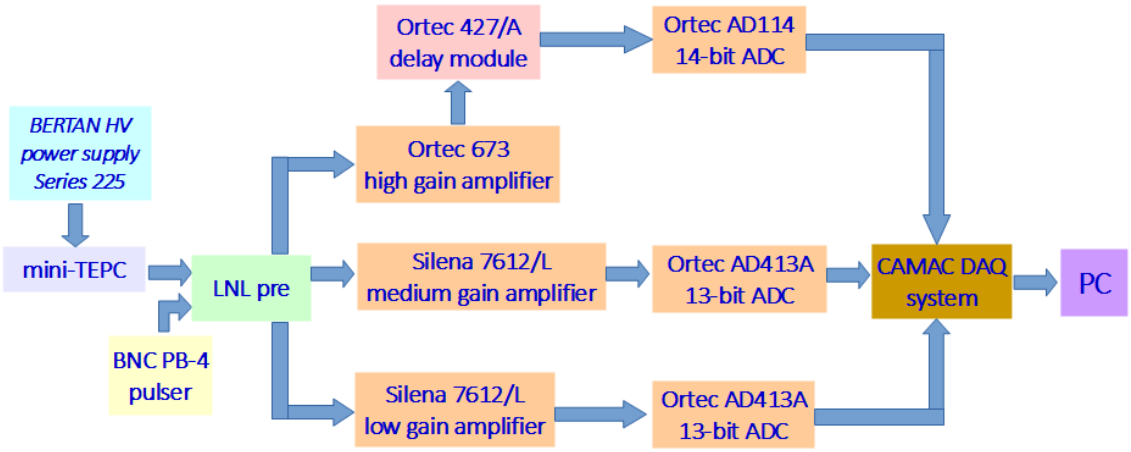

Figure 5.3: Scheme of the electronic chain showing the details of the electronic modules models.

An example of pulse-height spectrum is shown in Figure 5.4, where the normalized $yd(y)$ distributions collected at different voltages for a simulated site size of $d = 2.0\ \mu m$ are shown.

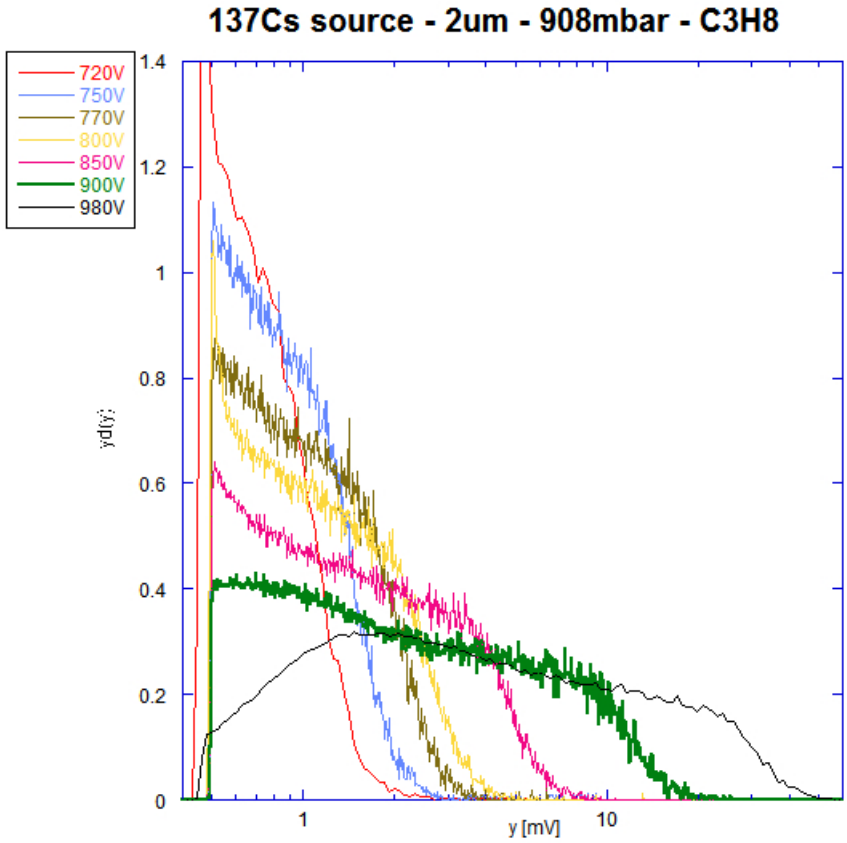

Figure 5.4: Microdosimetric spectra collected for a ^{137}Cs source at different voltages, for a simulated site size of 2.0 μm in pure propane.

It can be seen from Figure 5.4 that the electron edge shifts to higher values with increasing voltage, reflecting an increase in the gas gain. The variations of the Fermi fit intercept with applied voltage are presented in Figure 5.5 for each simulated size. Different pressures correspond to different spatial extensions of the electronic avalanche, as in Figure 5.2, so the multiplication phenomenon starts at a lower voltage difference.
The voltage increase allows to inspect also smaller LET events, causing a steep increase in the counting rate, as shown in Figure 5.6.
The complete set of calibrated spectra is presented in Figures 5.7, 5.8, 5.9 and 5.10.
At each site size it is possible to determine the threshold voltage allowing to resolve the full gamma spectrum. With low voltages just the events corresponding to the energy deposition of the exact stoppers are detected, while at higher voltages the electron "crossers"[1] contribution is also resolved.
The microdosimetric spectra retain their shape with varying voltage, except for the region close to the noise level.

[1]"Crossers" are particles originated outside the sensitive volume that cross the sensitive volume, depositing part of their energy in it.

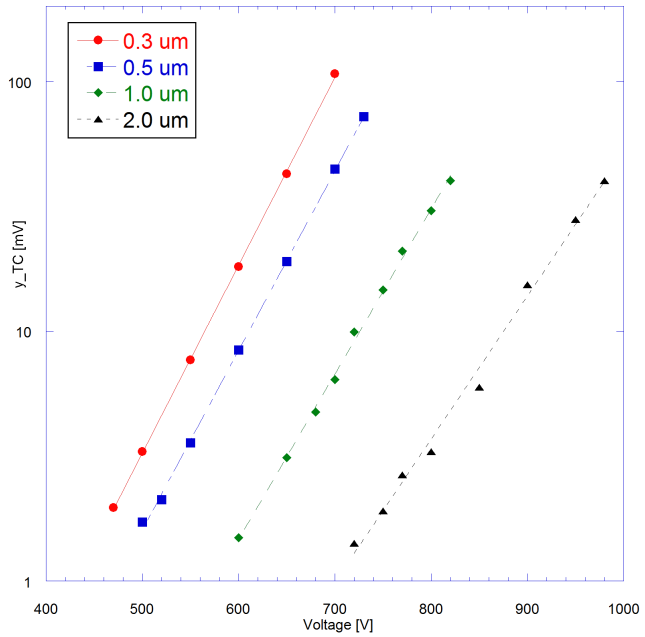

Figure 5.5: Variation of the un-calibrated ^{137}Cs electron-edge position with the applied voltage, for different simulated site sizes in pure propane. The lines represent the exponential curves fitting the experimental data.

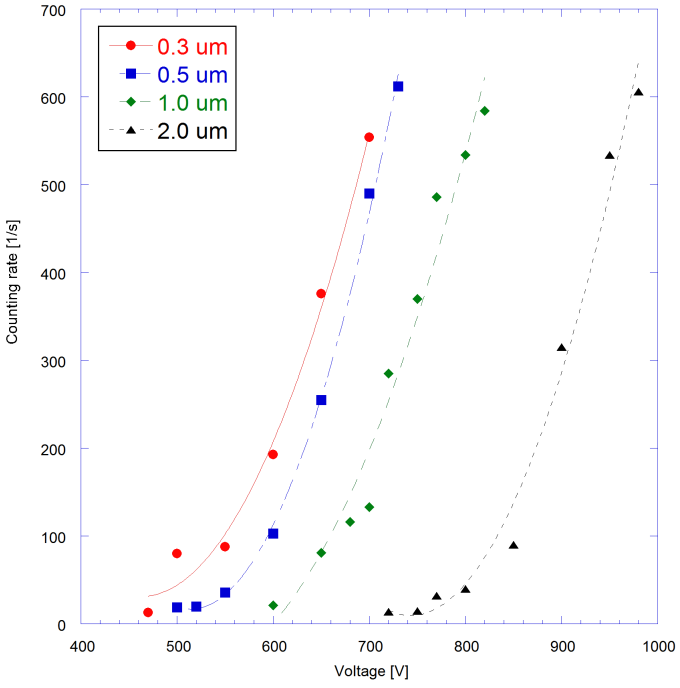

Figure 5.6: Variation of the counting rate for the ^{137}Cs source with the applied voltage, for different simulated site sizes in pure propane.

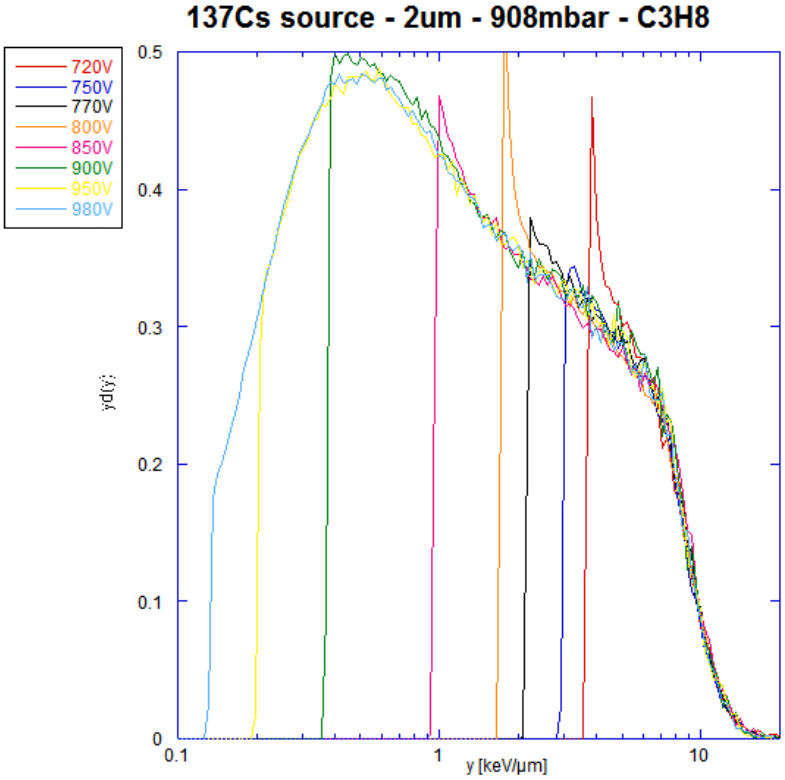

Figure 5.7: Microdosimetric spectra calibrated in lineal energy for a ^{137}Cs source at different voltages, for a simulated site size of 2.0 μm in pure propane.

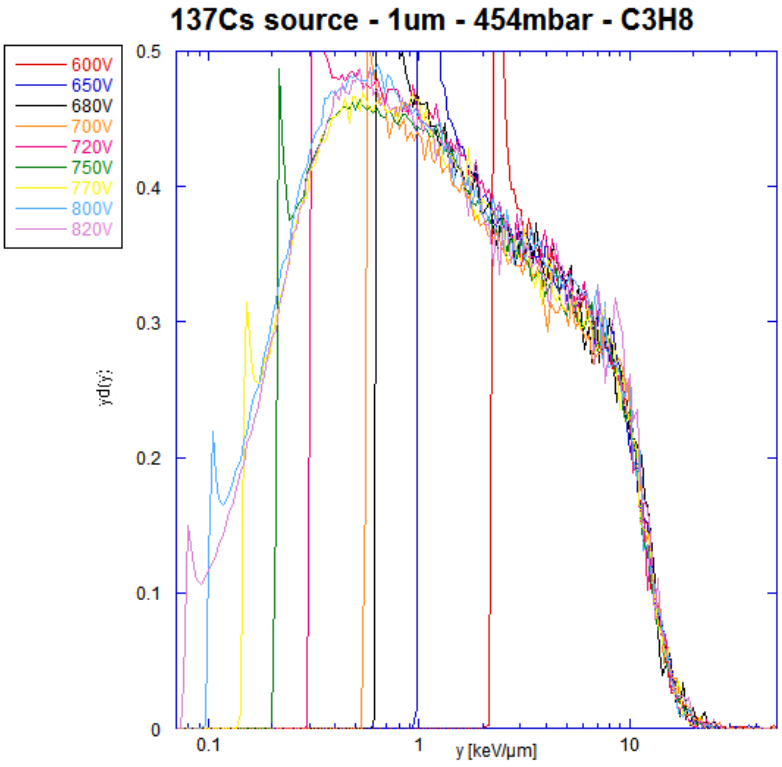

Figure 5.8: Microdosimetric spectra calibrated in lineal energy for a ^{137}Cs source at different voltages, for a simulated site size of 1.0 μm in pure propane.

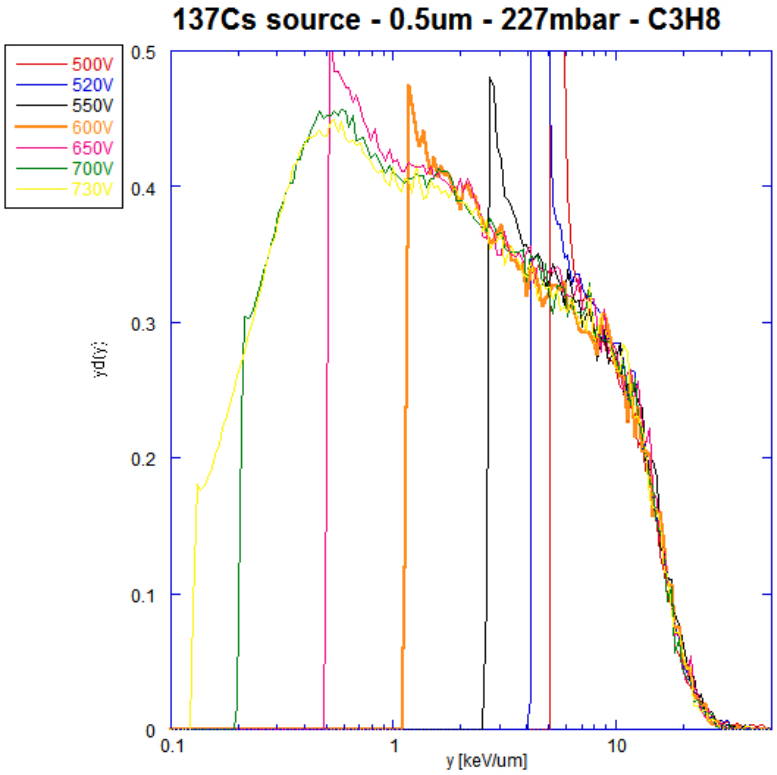

Figure 5.9: Microdosimetric spectra calibrated in lineal energy for a ^{137}Cs source at different voltages, for a simulated site size of 0.5 μm in pure propane.

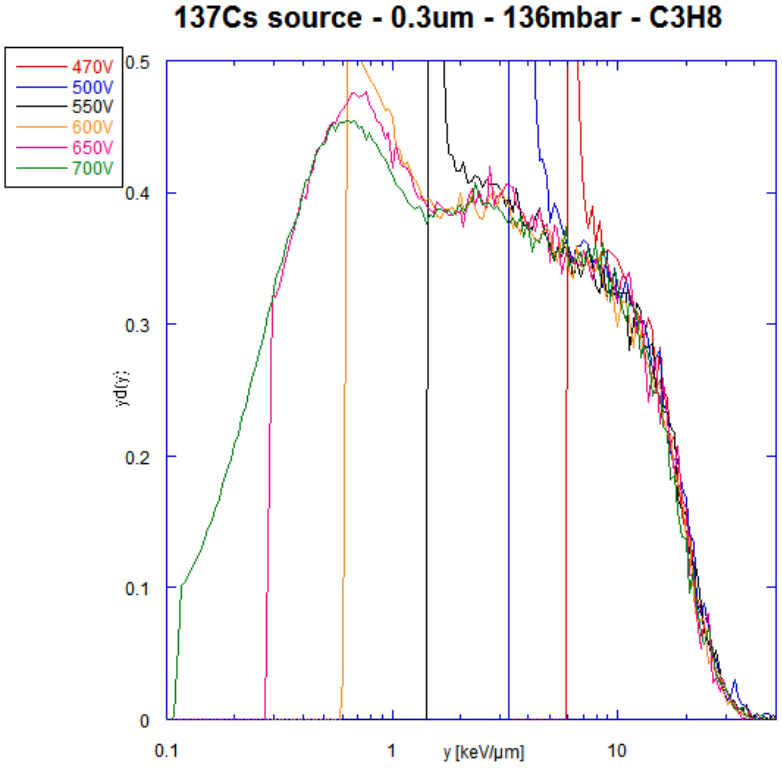

Figure 5.10: Microdosimetric spectra calibrated in lineal energy for a ^{137}Cs source at different voltages, for a simulated site size of 0.3 μm in pure propane.

6. Measurements at the CN accelerator, LNL-INFN

The response of the mini-TEPC AMiCo6 has been investigated in an intense beam of fast neutrons, produced from the reaction of 5.5 MeV deutons on a ^{7}Li target. The neutron projectiles are produced with energies up to 20 MeV, together with a ^{8}Be recoil.
Energetic deutons are provided by the CN accelerator at the LNL-INFN facility, a vertical electrostatic accelerator of the "Van de Graaff" type. The accelerated deutons are directed towards a LiF target through a series of magnetic deflectors. The beam current varied in the range $280 \div 310$ nA.
The position of the microdosimeter SV with respect to the target is shown in Figure 6.1.

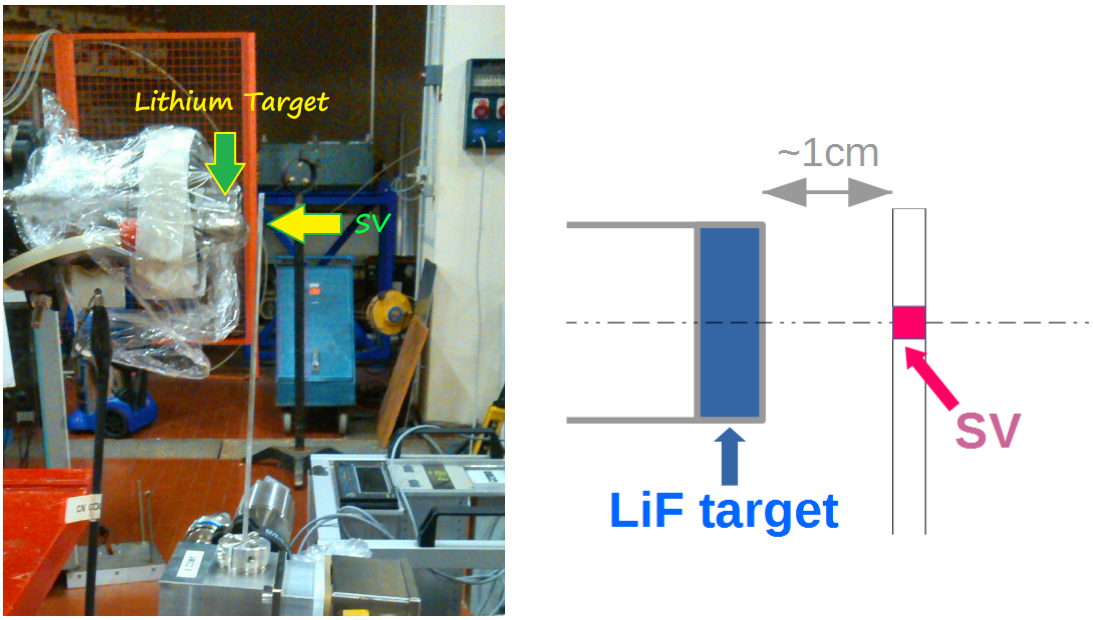

Figure 6.1: Detector position with respect to the lithium target.

Measurements were performed in pure propane by simulating different site sizes of 0.3 μm, 0.5 μm and 2.0 μm. These are intended as tests to find the optimal working conditions for future microdosimetric measurements in therapeutic beams at these simulated sizes.
The corresponding propane pressures have been calculated in Section 5.1. At each simulated size, several voltage differences have been applied in order to analyze the TEPC response at different gas gains. The complete set of measurements is presented in Table 6.1.
The electronic chain optimization procedure is the same as that of the previous sections. The electronic noise level at the preamplifier output was 700 μV rms. The

Site size [μm]	Propane pressure [mbar]	Voltage [ΔV]
0.3	136	470, 500, 550, 600, 650, 700
0.5	227	500, 520, 550, 600, 650, 700, 730
1.0	454	600, 650, 700, 710, 720, 730, 740, 750, 770, 800, 820, 850
2.0	908	720, 750, 770, 800, 850, 900, 950, 980

Table 6.1: Set of measurements performed the CN accelerator.

shaping time of the amplifiers was set to 250 ns. During the measurements the constancy of the ADC calibration has been repeatedly checked.
For the lineal energy calibration of the spectra, parallel measurements with a ^{137}Cs source were performed.

6.1 Results

When interacting with the tissue equivalent plastic constituting the counter cathode, fast neutrons mainly collide with the hydrogen nuclei through elastic collisions [53], leading to the presence of a proton peak in the microdosimetric spectra, responsible for the majority of the absorbed dose. The proton edge can be distinctly identified at a lineal energy around 150 $keV/\mu m$, while the contribution of α particles resulting from (n,α) can be identified at higher lineal energies.
For the lineal energy calibration the proton-edge was used. Its values for different simulated sizes are reported in Table 6.2.

Site size [μm]	y_{p-edge} [keV/μm]
0.3	152.0
0.5	150.0
1.0	146.3
2.0	136.8

Table 6.2: Lineal energies corresponding to the proton edge for different simulated site sizes [61].

The collected spectra calibrated in lineal energy are presented in Figures 6.2, 6.3, 6.4 and 6.5 for different simulated sizes.
At each simulated size, some features of the microdosimetric spectra depend on the applied voltage.
In the case of a simulated size of 0.3 μm, at 470 V to 500 V the proton and alpha peak are evident, and the only variation in the spectra shape is due to the improvements in the lower energy threshold with the higher gas gain (voltage). The further voltage increase allows to inspect lower energy deposition events due to the gamma component of neutron induced reactions. As a drawback, the high-LET part of the spectra begins to shrink, which is evident at 600 V. This feature is ascribed to a self-screening effect in the electric field inside the counter when high-LET events are inspected. This phenomenon marks the saturation point of the electronic avalanche. In this situation the higher-LET events are detected as lower energy events, with a strong modification of the spectra shape.
These features are presented at each simulated size.
The set of voltages that can be applied at each size without loosing the information

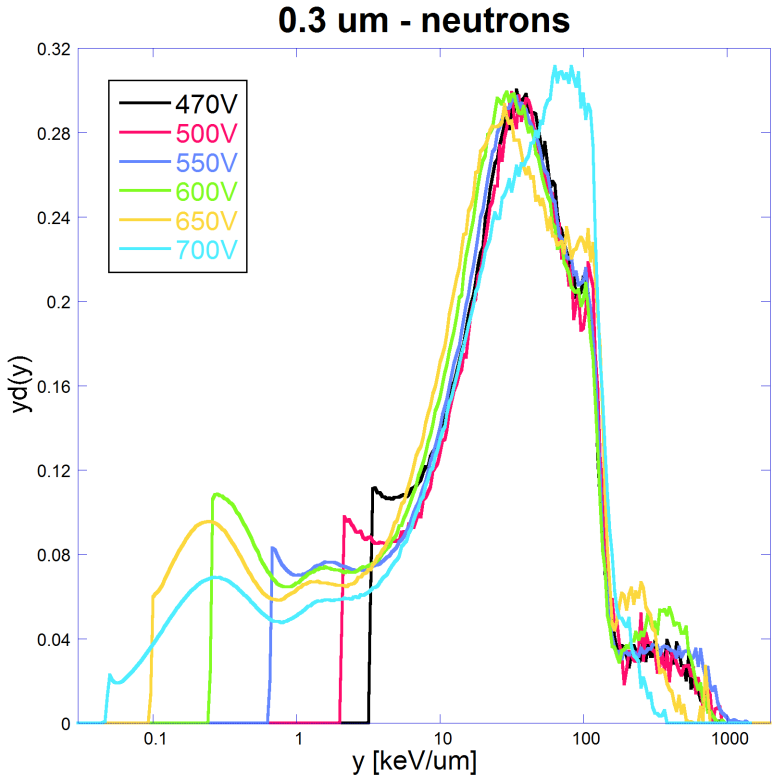

Figure 6.2: Microdosimetric spectra calibrated in lineal energy in a neutron field at different voltages, for a simulated site size of 0.3 μm in pure propane.

on the high-LET events and changing the spectra shape, is presented in Table 6.3, together with the lowest lineal energy measurable y_{th}. It is to be noted that low-LET

Site size [μm]	ΔV [V]	y_{th} [keV/μm]
0.3	470÷550	0.67
0.5	500÷600	0.76
1.0	600÷720	0.34
2.0	800÷850	0.47

Table 6.3: Optimal voltage ranges for the mini-TEPC application at different simulated sizes.

events also include the gamma component due to target activation. This is not fixed during time, and it is difficult to evaluate. As an example, the measurement at a simulated size of 2.0 μm at 800 V was repeated at two different times in the measurement shift. The result is presented in Figure 6.6, where the gamma component in the second measurement is increased of a factor of about 1.2.
The analysis of the neutron data is still ongoing, since the measurements were performed in late March 2015. The obtained results will be fundamental for the next measurement campaign at the LNS-INFN laboratories, where the mini-TEPC will investigate a fixed beam of carbon ions for eye therapy.

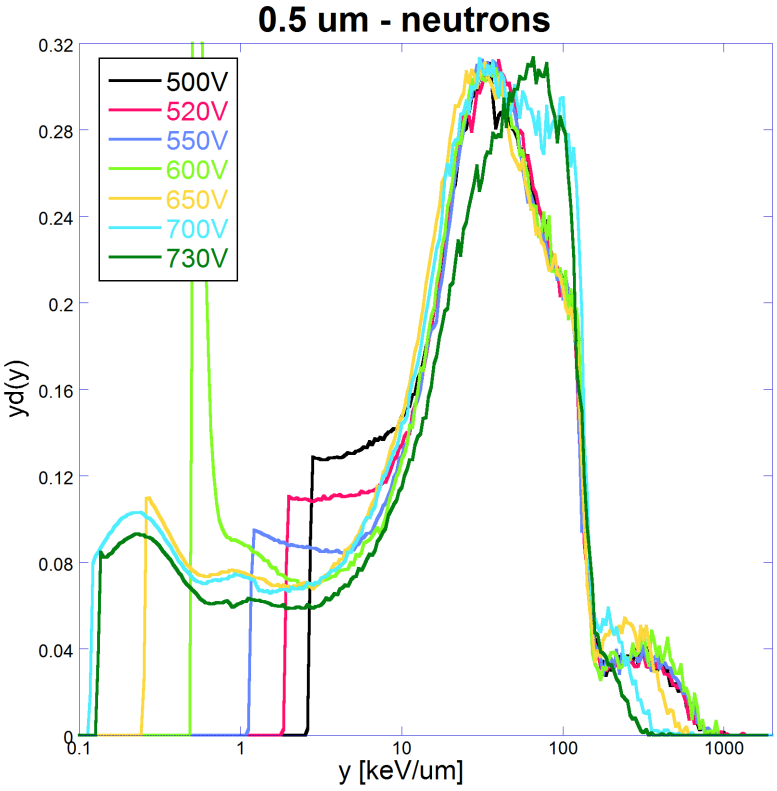

Figure 6.3: Microdosimetric spectra calibrated in lineal energy in a neutron field at different voltages, for a simulated site size of 0.5 μm in pure propane.

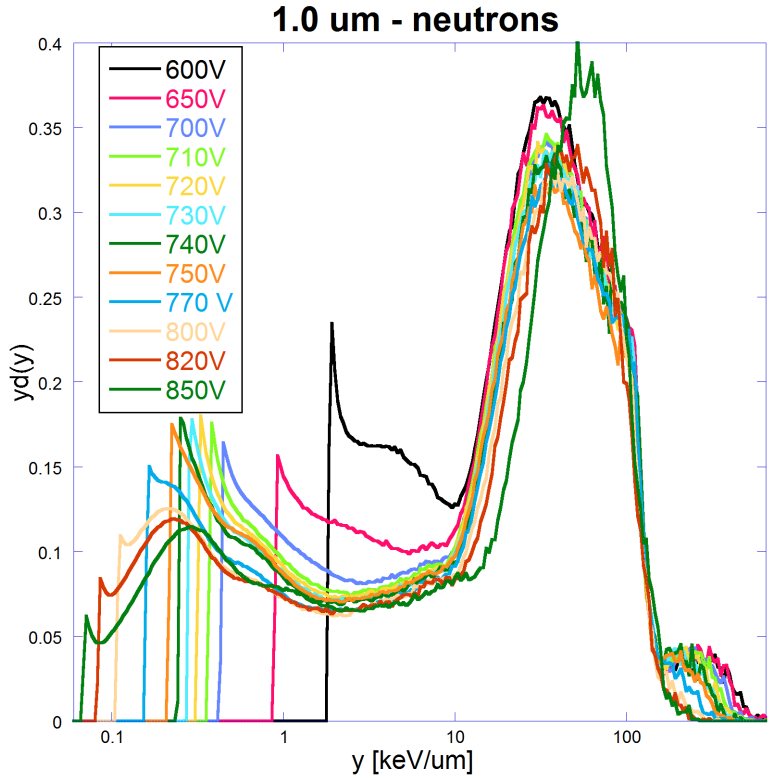

Figure 6.4: Microdosimetric spectra calibrated in lineal energy in a neutron field at different voltages, for a simulated site size of 1.0 μm in pure propane.

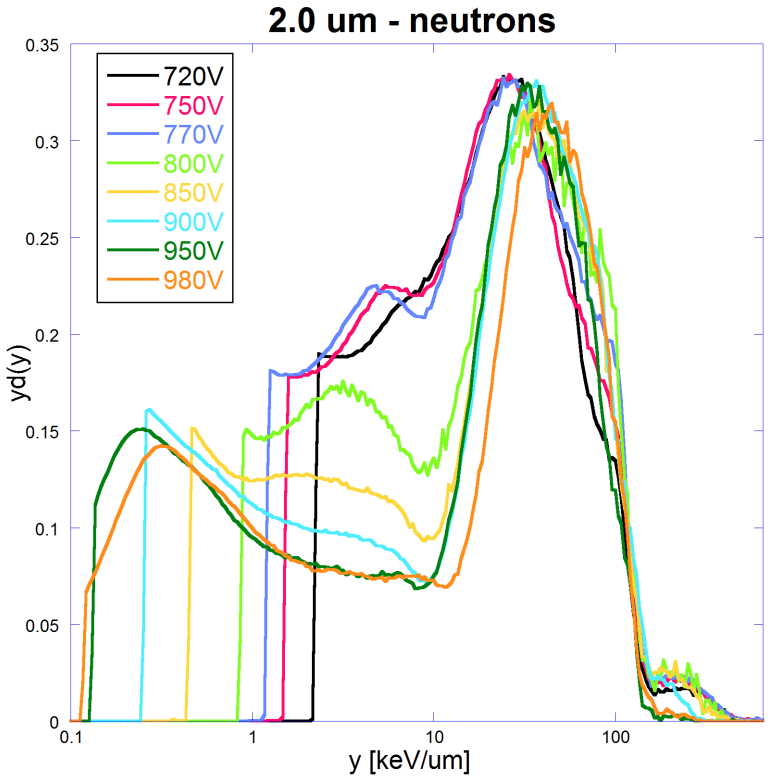

Figure 6.5: Microdosimetric spectra calibrated in lineal energy in a neutron field at different voltages, for a simulated site size of 2.0 μm in pure propane.

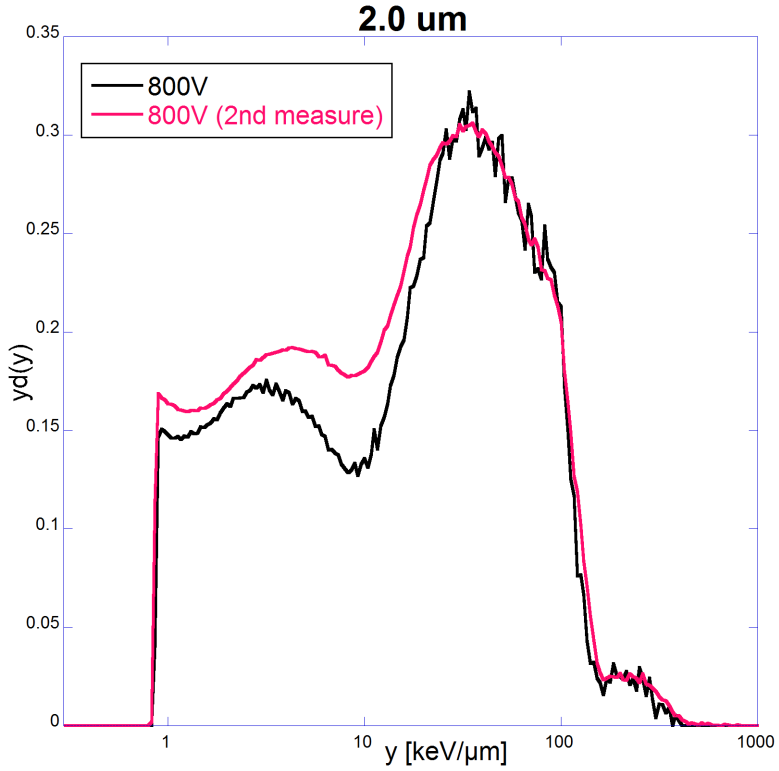

Figure 6.6: Microdosimetric spectra for a simulated site size of 2.0 μm in pure propane at 800 V, collected at different times.

7. Measurements at CNAO, Pavia

The AMiCo 6 mini-TEPC has been tested using a therapeutic carbon beam at the CNAO facility in Pavia.
The aim of these measurements is to investigate the TEPC performances when high fluxes of high-LET particles are inspected. Up to now the majority of microdosimetric measurements with carbon ions are not made with clinical beams. The test of the microdosimeter response in a real therapeutic plan is crucial to study the feasibility of a microdosimetric assessment of the clinical beam RBE.

7.1 Beam Characteristics

At the CNAO facility the carbon ions are accelerated by a synchrotron of 25 m diameter, and the extracted beam (spill) can be brought to three different treatment rooms. During the treatment an active beam scanning modality is used. The tumor to be treated is divided into slices perpendicular to the beam direction, each reached by particles with the same range. The energy is automatically varied by the synchrotron so as to choose the proper slice to treat. Each slice is then "painted" with the particle beam, which moves within the slice thanks to two scanning magnets. A sketch of the active beam system is presented in Figure 7.1.

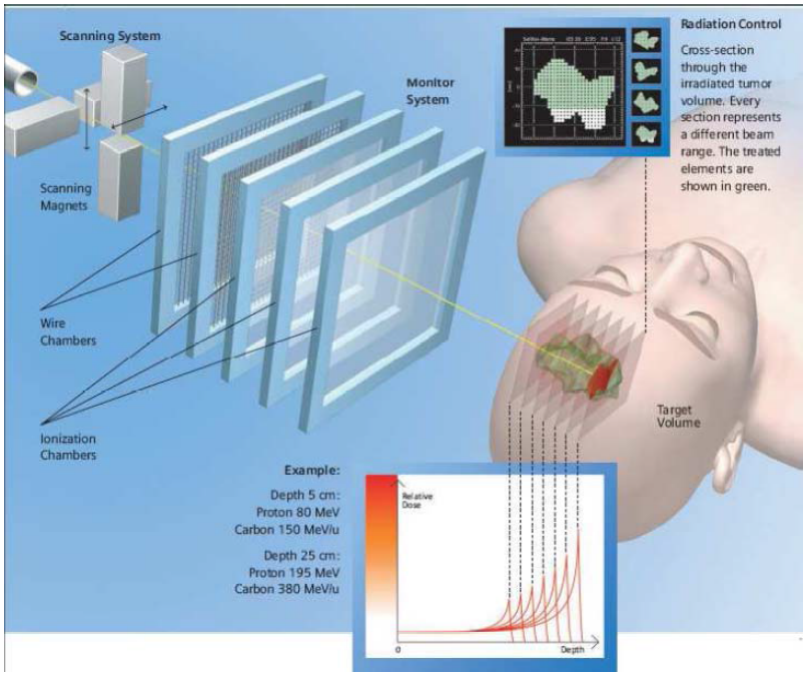

Figure 7.1: Illustration of the active scanning system.

The measurements were performed with a monoenergetic carbon ion beam with energy 195.2 MeV/amu, equivalent to a 80 mm range in water.
Due to its narrowness, the Bragg peak was widened by using two ripple filters (passive energy modulators) to better investigate the Bragg peak region. The reference depth-dose curves with and without the double ripple filter for a single pencil beam are shown in Figure 7.2. The zero position is set at the isocenter of the therapeutic beam, which is a reference point marked by laser light in the treatment room.

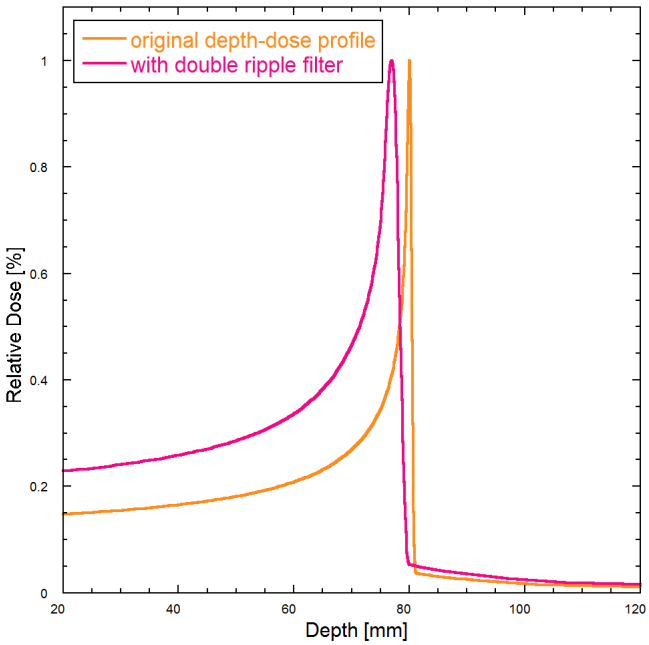

Figure 7.2: Depth-dose curves with and without the double ripple filter for a 195.2 MeV/amu carbon beam.

The field irradiates a water phantom where the mini-TEPC can be inserted, covering a square of area 3×3 cm^2, centered at the isocenter. The square is then divided into 15×15 voxels. The irradiation is performed by scanning each of the 225 spots in sequence, repeating this procedure 10 times. The FWHM of the beam changes from aabount 0.7 mm to 6.2 mm, when using the double ripple filter. A scheme of the spatial distribution of the irradiated spots is shown in Figure 7.3.
Each measurement (2250 irradiated spots) consists approximately of 90 spills, each spill covering 25 spots. From the temporal point of view the spills last 1 s with a pause of approximately 4.5 s between them. The intensity of particles is 10^6 per spill. The spots are irradiated with a dose driven method, when the desired dose value is reached the beam is displaced to the next spot.

7.2 Measurements Description

In order to perform the measurements the mini-TEPC was inserted in a phantom made of a PMMA box filled with water, with the entrance window placed perpendicularly to the beam direction. The mini-TEPC was housed inside a Lucite support, that in turn is fixed to a movable rod connected to the PMMA box. The water phantom with the detector is shown in Figure 7.4, together with the .

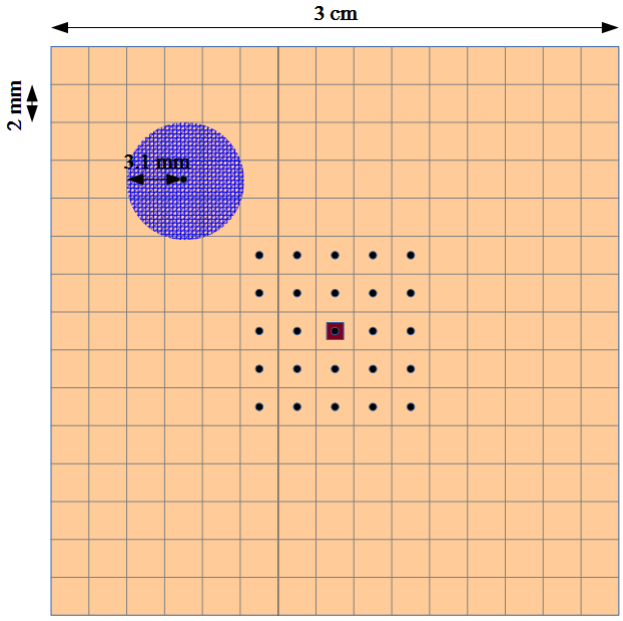

Figure 7.3: Schematic drawing of the spatial characteristics of the field. Each square represents a voxel, the irradiation spot is at its center. The blue circle indicates the transversal extension of the beam, covering more than one spot at each irradiation step. The red square indicates the detector position in the phantom, and the points indicate the spots contributing to the SV irradiation.

The measurements are performed in an actual treatment room at the CNAO facility. The adopted experimental setup is shown in Figure 7.5.
The microdosimetric measurements were performed at different water equivalent depths, by simulating a tissue-equivalent size is 1 μm with pure propane. As shown in the previous sections, this corresponds to a gas pressure of $P_{C3H8} = 454\ mbar$.
At each position, it was chosen to collect the microdosimetric spectra at two distinct voltage differences between the electrodes of the SV, as suggested from the previous experience in the high-LET neutron fields. Due to the limited measuring time available, the acquisition with two voltages was not performed for all depths. The complete set of measurements together with the applied voltages is presented in Table 7.1 and in Figure 7.6.

Distance from isocenter [mm]	DDP position [mm]	Voltage [V]
48.5	40.2	600, 750
68.5	60.2	600, 750
83.3	75	600, 750
84.3	76	600
85.4	77	600, 750
86	77.7	600, 750
86.6	78.3	600, 750

Table 7.1: Set of measurements performed at CNAO. The left column indicates the position of the sensitive volume in the water phantom, with respect to the isocenter. The middle column shows the equivalent position of the detector in the depth-dose profile with the double ripple filter, shown in Figure 7.2.

The setup and optimization of the electronic chain was carried out by performing the steps described in the previous sections.
In order to optimize the time available to perform the measurements and to have a reliable estimate of the counting rate in the detector, it was planned to use an Ether-

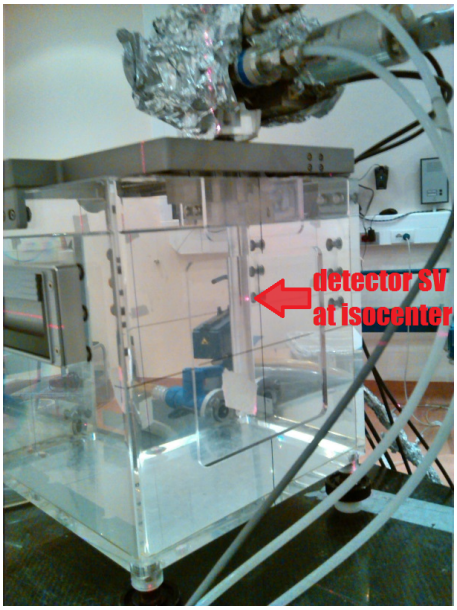

Figure 7.4: Picture showing the water phantom irradiated with the CNAO carbon beam, where the detector position in emphasized.

net cable for the remote control of the acquisition PC, placed in the treatment room. In this condition the electronic noise caused an obscuration of the first 1150 channels of the 14-bits ADC. The remote control of the acquisition computer was then performed using the internal LAN network of the CNAO facility. In this condition the noise level covered the first 740 ADC channels of the 14-bits ADC. To further reduce the electronic noise contribution it was then chosen to operate by manually starting and stopping the acquisition between each measurement. With this choice the electronic noise level was reduced to 300 channels. The noise level measured by means of the oscilloscope was approximately 600 μV at the preamplifier output. The shaping time of the amplifiers was set to 250 ns. During the measurement shift the constancy of the ADC calibration has been repeatedly checked.

7.3 Results

The spectra acquired with the two different voltages were joined together after the identification of a proper superposition region at 100 $keV/\mu m$. The collected microdosimetric spectra calibrated in lineal energy, are shown in Figure 7.7.
The lineal energy calibration has been performed by using the carbon edge region in the pulse height spectra, which is evident at a water equivalent depth of 77.7 mm. This is fitted with a Fermi function and used as reference for the energy calibration of the spectra. The carbon edge has been assigned to the lineal energy of 1397 $keV/\mu m$, corresponding to the maximum energy released in 1 μm of liquid water [**?**].

The shape of the microdosimetric spectra, hence the dose fraction imparted in same lineal energy intervals, strongly varies with depth, the contribution of high-LET events strongly increasing in the Bragg peak region.
For the two spectra collected before the Bragg peak, the fast carbon ions cross the

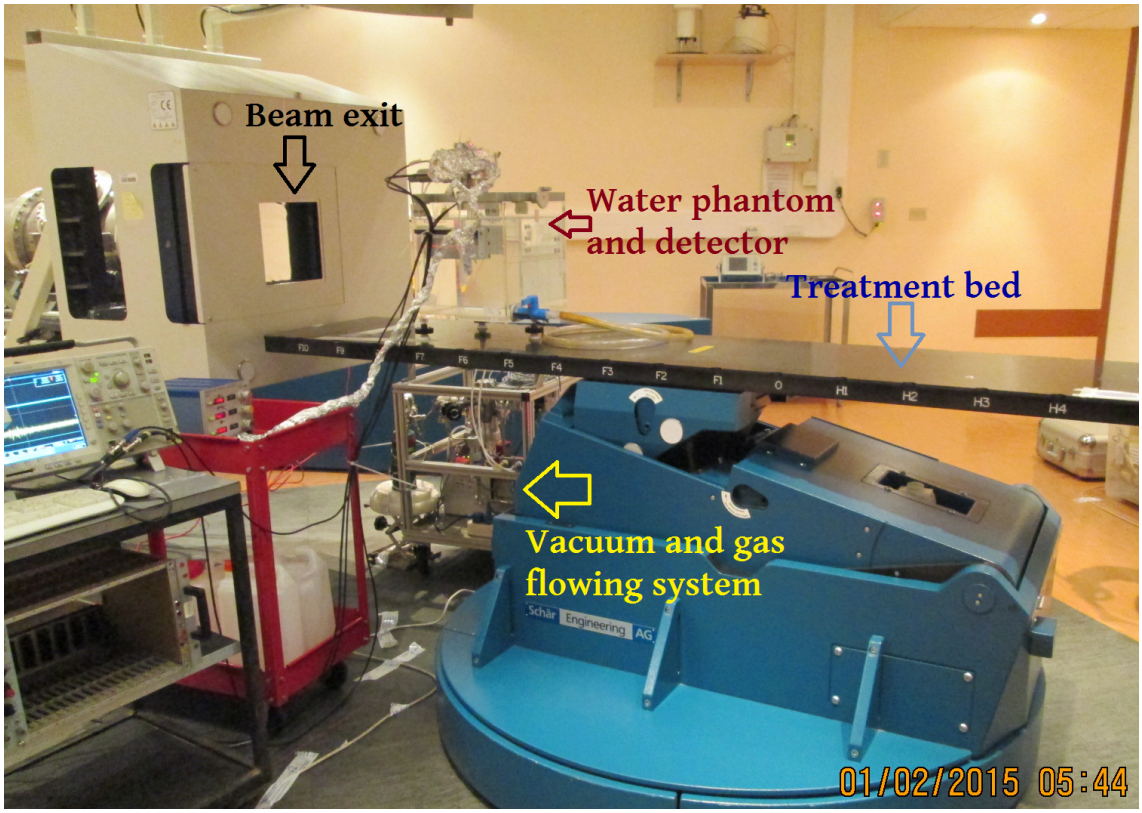

Figure 7.5: Picture showing the CNAO treatment room in which the measurements were performed. The height of the treatment bed is adjusted so that the isocenter position matches the detector SV. The electronic modules for data processing are placed on the left.

SV by releasing just part of their energy inside it. This energy deposition modality constitutes the 92% of the absorbed dose for those depths.
The carbon peak shifts to higher energy values with increasing depth, until the carbon edge is reached. At a depth of 77.7 mm the carbon edge is evident, and the relative importance of high-LET events begins to increase.
Nuclear reactions occurring in the energy range of interest in hadron therapy have been studied experimentally and through Monte Carlo simulations, e.g. in [66], [67], [69], [70]. The most frequent nuclear reactions that carbons undergo are peripheral collisions with the target atoms, namely the carbons constituting the tissue equivalent plastic of the counter walls. These interactions result in the projectile breakup, giving a mixed field of secondary charged (from Z=5 to Z=1) and neutral (fast neutrons) particles, which contribute to an energy deposition beyond the Bragg peak, and with a broad angular distribution. Monte Carlo simulations [67] suggest that the major dose contribution just behind the Bragg peak is due to boron fragments. At higher depths hydrogen and helium fragments constitute the major component, due to their longest range.
Due to these facts low-LET events become dominant in the distal part after the Bragg peak. In particular, two peaks arise in the dose distribution at 10 $keV/\mu m$ and 50 $keV/\mu m$, the former attributed to energy depositions from protons and α particles, the latter from α and boron ions.
In order to verify the consistency between experimental and calculated data, Monte Carlo simulations with the transport code FLUKA, have been performed **??**. Figure

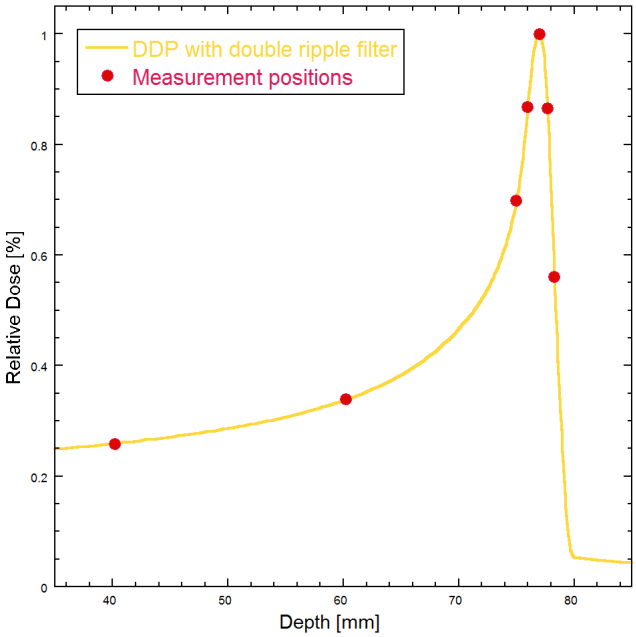

Figure 7.6: Investigated positions with reference to the enlarged depth-dose profile.

7.8 shows the experimental spectrum corresponding to a water equivalent depth of 77.7 mm, and the calculated microdosimetric spectra for a fixed carbon beam targeting the detector SV and when the same beam covers stochastically the irradiated area of 3×3 cm^2. For lineal energy values below 100 $keV/\mu m$ the best approximation of the experimental microdosimetric distribution is obtained by using the spatially varying carbon beam. This shows that energy deposition events taking place in the transversal direction with respect to the primary carbon beam give rise to a non negligible low-LET events contribution inside the counter.
The microdosimetric spectra can be used to assess the actual absorbed dose in the sensitive volume of the detector. For a cylindrical sensitive volume with height and diameter equal to d the relation between the single-event imparted energy and the lineal energy, for a simulated material of density $\rho = 1$ g/cm^3, is given by [48]

$$z[Gy] = \frac{0.136}{[d(\mu m)]^2} y\,[keV/\mu m]\,. \tag{7.1}$$

In a microscopic volume with a large number of events, the dose D is proportional to $\bar{y}_F$, in fact

$$D[Gy] \sim n\bar{z}_{1F}[Gy] = n\frac{0.136}{[d(\mu m)]^2}\bar{y}_F\,[keV/\mu m]\,, \tag{7.2}$$

where n is the number of the events corresponding to the energy deposition events giving rise to the specific energies with mean value D, while $\bar{z}_{1F}$ is the first momentum of the single event imparted energy distribution. Multiplying the average frequency lineal energy value for the number of events will thus give an indication of the actual dose imparted in the microdosimeter.
In order to evaluate the $\bar{y}_F$ values a first operation consists in the linear extrapolation of the counts of the microdosimetric spectra from the measurement threshold to the value of 0.01 $keV/\mu m$, considered as the threshold of ionizing events. The

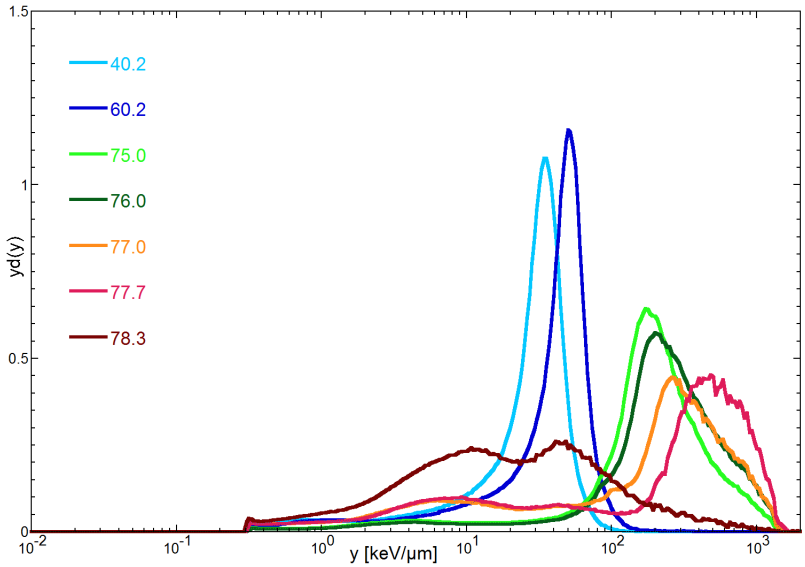

Figure 7.7: Microdosimetric spectra calibrated in lineal energy, for a 195.2 MeV/amu carbon ion beam at different water-equivalent depths (in mm).

uncertainty in the $\bar{y}_F$ values, including the extrapolation and the lineal energy contribution, has been calculated as in [55].
The extrapolated lineal energy spectra are presented in Figure 7.9.
Since the microdosimetric spectra are normalized at unitary dose, the $\bar{y}_F$ as a function of depth will have the same trend as the absorbed dose. In Figure 7.10 the $\bar{y}_F$ value corresponding to the the maximum of the depth-dose curve ($\bar{y}_F \approx 40\ keV/\mu m$), has been set equal to 1. The other $\bar{y}_F$ values are normalized to this maximum value. The uncertainty associated with the position is $\pm$ 0.3 mm. It can be seen that the $\bar{y}_F$ values reproduce the trend of the absorbed dose profile, apart from an offset of about 0.5 mm in the TEPC position.
This procedure shows that the use of microdosimetric data from measurements with two different gas gain allow leads to consistent results.

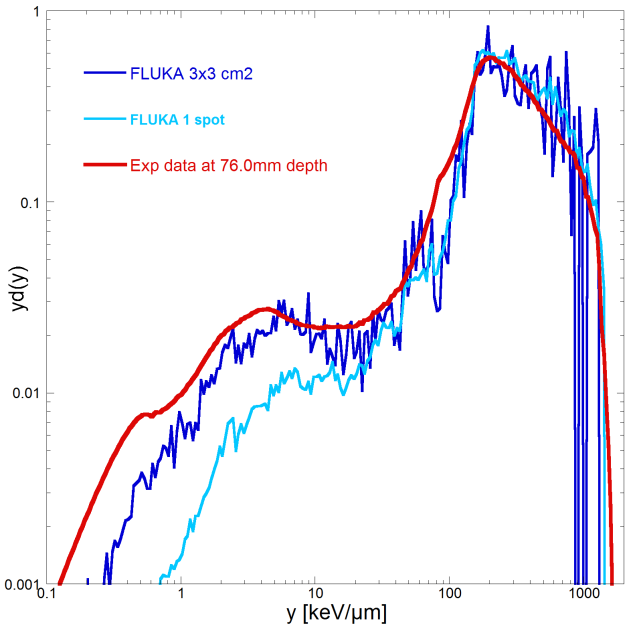

Figure 7.8: Experimental (red line) and simulated data, for a fixed (light blue line) and spatially varying (blue line) 195.2 MeV/amu carbon ion beam hitting the detector sensitive volume, using the FLUKA transport code, as in [68].

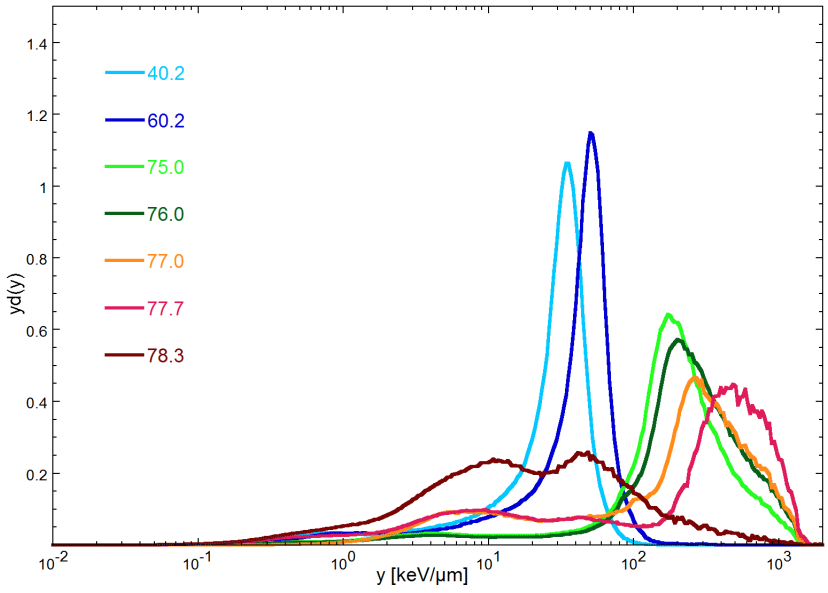

Figure 7.9: Extrapolated microdosimetric spectra calibrated in lineal energy, for a 195.2 MeV/amu carbon ion beam at different water-equivalent depths (in mm).

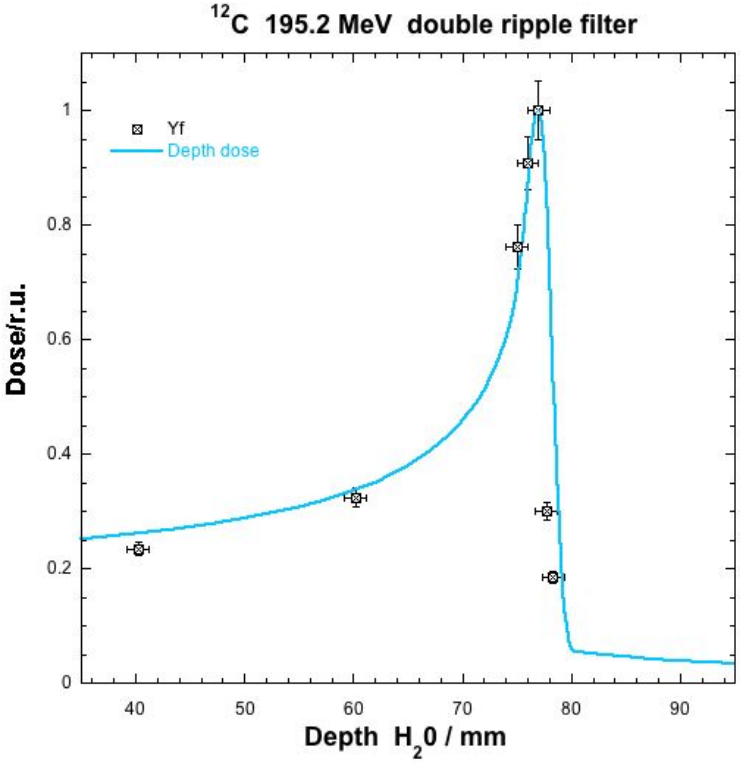

Figure 7.10: Relative values of $\bar{y}_F$ with error bars for a 195.2 MeV/amu carbon ion beam at different water-equivalent depths.

8. Conclusions

The response of new mini-TEPC designed and built in at the LNL-INFN laboratories has been tested in several irradiation fields.
Lineal energy distributions have been collected for a variety of simulated sizes employing pure propane as filling gas, both in high- and low-LET fields.
Experimental data show that for low-LET fields the microdosimetric spectra retain the same shape with changes in the gas gain, apart from an improvement of the lower energy size detectable.
At the moment it has been observed that for high-LET events the spectra shape suffer a distortion when high gas gains are employed, while at lower applied voltages in the counter the spectra shape retain the same shape. For this reason, in order to work with a large range of event sizes (with ion and neutron beams), the best option seems to acquire the microdosimetric distributions with two different gas gains. The two spectra are joined offline, in order to retain the information on the full lineal energy range.
This method has been employed at the CNAO facility, investigating the response of a pulsed carbon ion beam employed in radiation therapy. A sign of the consistency of this method is given by the evaluation of the dose imparted in the microdosimeter, which conforms to the dosimetric measurements performed for the same beam. For the interpretation of the dose contribution due to the low-LET fragments produced by the carbon fragmentation, the experimental data have been compared with Monte Carlo simulations.
The CNAO measurements are among the first microdosimetric measurements performed in therapeutic carbon ion beams. The results obtained will be useful in the next scheduled measurement campaign which will investigate the mini-TEPC response in the fixed carbon beam of the CATANA facility at LNS-INFN. Microdosimetric measurements will be compared to the carbon data collected at CNAO, and will give an insight on the difference between the mini-TEPC response in fixed and pulsed beams.
The data analysis has been performed with a software having a graphical user interface written in C++, which allows to perform a quick spectra calibration and the calculation of the microdosimetric distributions, optimizing the elaboration time. Its further development is planned, with the extension of the number of implemented algorithms tailored for mini-TEPC applications.

A. C++ sources

A.1 Linear Regression

```
void lin_regr(int dim, double x[], double y[], double &intercept, double &slope, double
    &sigma_intercept, double &sigma_slope, double &sigma_y){

    double sum_x=0., sum_x2=0., sum_y=0., sum_xy=0.;
    for(int i=0;i<dim;i++){
        sum_x+=x[i];
        sum_x2+=pow(x[i],2.);
        sum_y+=y[i];
        sum_xy+=x[i]*y[i];
    }

    double Delta=dim*sum_x2-pow(sum_x,2.);
    intercept=(sum_x2*sum_y-sum_x*sum_xy)/Delta;
    slope=(dim*sum_xy-sum_x*sum_y)/Delta;

    double denominator_sigma_y=0.;
    for(int i=0; i<dim; i++){
        denominator_sigma_y+=pow(intercept+slope*x[i]-y[i],2.);
    }
    sigma_y=sqrt(denominator_sigma_y/(dim-2));
    sigma_intercept=sigma_y*sqrt(sum_x2/Delta);
    sigma_slope=sigma_y*sqrt(dim/Delta);

    return;
}
```

A.2 Calibration and Rebinning

```
int calib_and_comp(string nomefile, string workdir, long double int_LL, long double
    slo_LL, long double int_ML, long double slo_ML, long double int_HL, long double
    slo_HL, int no_intervals, long double y_min)
{
    char inputfile[400], outputfileLL[400], outputfileML[400], outputfileHL[400];
    strcpy(inputfile, nomefile.c_str());

int B = no_intervals; //numero intervallini per decade

long double LL[16384], ML[16384], HL[16384];
for(int i=0;i<16384;i++){LL[i]=0., ML[i]=0., HL[i]=0.;}

ifstream InputFile;
InputFile.open(inputfile);
```

```
if (!InputFile) {return 0;}

char empty1, empty2, empty3;
InputFile >> empty1 >> empty2 >> empty3;
double empty4, empty5, empty6;
InputFile >> empty4 >> empty5 >> empty6;

//LETTURA DEL FILE IN INPUT E INIZIALIZZAZIONE DEGLI ARRAY
for(int i=0;i<16384;i++) {
InputFile >> LL[i];
InputFile >> ML[i];
InputFile >> HL[i];
}
InputFile.close();

/*****************************************************************************************/

//CALIBRAZIONE DEI CANALI IN mV
long double mV_LL[16384], mV_ML[16384], mV_HL[16384];
for(int i=0;i<16384;i++){
mV_LL[i]=int_LL+(i+1)*slo_LL;
mV_ML[i]=int_ML+(i+1)*slo_ML;
mV_HL[i]=int_HL+(i+1)*slo_HL;
}

/*****************************************************************************************/

//SETTAGGIO DEGLI ESPONENTI DI 10 MINIMO E MASSIMO DELLO SPETTRO MICRODOSIMETRICO
long double min_mV=y_min, max_mV=1.;
for(int i=0;i<16384;i++) {
  //if(mV_LL[i]<min_mV && mV_LL[i]>0.){min_mV=mV_LL[i];}
  if(mV_LL[i]>max_mV){max_mV=mV_LL[i];}
  if(mV_ML[i]>max_mV){max_mV=mV_ML[i];}
  if(mV_HL[i]>max_mV){max_mV=mV_HL[i];}
}

int e_min, e_max;
 { long double temp1=log10(min_mV); e_min=floor(temp1);
   long double temp2=log10(max_mV); e_max=floor(temp2+1.);}

int N=e_max-e_min; //numero di decadi

//SETTAGGIO DEGLI ESTREMI DELLE DECADI

long double y0[N+1];
for(int i=0;i<N+1;i++){y0[i]=pow(10,e_min+i);}

/*****************************************************************************************/

//DEFINIZIONE DEGLI ARRAY PER IL COMPATTAMENTO E INIZIALIZZAZIONE A ZERO
int size=N*B;
double y_comp[size], N_LL[size], N_ML[size], N_HL[size];
for(int i=0;i<size;i++){y_comp[i]=0., N_LL[i]=0., N_ML[i]=0., N_HL[i]=0.;}

//CALCOLO DELLE y COMPATTATE

for(int j=0;j<N;j++){for(int i=j*B;i<(j+1)*B;i++){
  double a=i*1., b=j*1., c=B*1., exp=(a-b*c)/c;
  y_comp[i]=y0[j]*pow(10.,exp);
}}
```

```
//CALCOLO DEGLI INTERVALLI DELTA_y
double Dy[size];
for(int i=0;i<size;i++){Dy[i]=0.;}
for(int i=0;i<size;i++){Dy[i]=y_comp[i]*(pow(10,0.5/B)-pow(10,-0.5/B));}

//COUNTERS

int counter_LL[size], counter_ML[size], counter_HL[size];
for(int i=0;i<size;i++){counter_LL[i]=0, counter_ML[i]=0, counter_HL[i]=0;}

//REBINNING DELLE ORDINATE

for(int i=0;i<16384;i++){
  if(mV_LL[i]!=0.&&LL[i]!=0.){
  for(int j=0;j<size;j++){
    double Delta_inf, Delta_sup;
    if(j==0){Delta_inf=0.;} else {Delta_inf=(y_comp[j]-y_comp[j-1])*0.5;}
    if(j==size-1){Delta_sup=0.;} else {Delta_sup=(y_comp[j+1]-y_comp[j])*0.5;}

    if(mV_LL[i]>=y_comp[j]-Delta_inf && mV_LL[i]<y_comp[j]+Delta_sup){N_LL[j]+=LL[i];}
}}}

for(int i=0;i<16384;i++){
  if(mV_ML[i]!=0.&&ML[i]!=0.){
  for(int j=0;j<size;j++){
    double Delta_inf, Delta_sup;
    if(j==0){Delta_inf=0.;} else {Delta_inf=(y_comp[j]-y_comp[j-1])*0.5;}
    if(j==size-1){Delta_sup=0.;} else {Delta_sup=(y_comp[j+1]-y_comp[j])*0.5;}

    if(mV_ML[i]>=y_comp[j]-Delta_inf && mV_ML[i]<y_comp[j]+Delta_sup){N_ML[j]+=ML[i];}
}}}

for(int i=0;i<16384;i++){
  if(mV_HL[i]!=0.&&HL[i]!=0.){
  for(int j=0;j<size;j++){
    double Delta_inf, Delta_sup;
    if(j==0){Delta_inf=0.;} else {Delta_inf=(y_comp[j]-y_comp[j-1])*0.5;}
    if(j==size-1){Delta_sup=0.;} else {Delta_sup=(y_comp[j+1]-y_comp[j])*0.5;}

    if(mV_HL[i]>=y_comp[j]-Delta_inf && mV_HL[i]<y_comp[j]+Delta_sup){N_HL[j]+=HL[i];}
}}}

for(int i=0;i<16384;i++){
    for(int j=1;j<size-1;j++){
        if(mV_LL[i]>=y_comp[j]-(y_comp[j]-y_comp[j-1])*0.5 &&
            mV_LL[i]<y_comp[j]+(y_comp[j+1]-y_comp[j])*0.5) counter_LL[j]++;
        if(mV_ML[i]>=y_comp[j]-(y_comp[j]-y_comp[j-1])*0.5 &&
            mV_ML[i]<y_comp[j]+(y_comp[j+1]-y_comp[j])*0.5) counter_ML[j]++;
        if(mV_HL[i]>=y_comp[j]-(y_comp[j]-y_comp[j-1])*0.5 &&
            mV_HL[i]<y_comp[j]+(y_comp[j+1]-y_comp[j])*0.5) counter_HL[j]++;
    }
}

//CALCOLO MEDIE
double average_LL[size], average_ML[size], average_HL[size];
for(int i=0;i<size;i++){average_LL[i]=0., average_ML[i]=0., average_HL[i]=0.;}
for(int i=0;i<size;i++){
    if(counter_LL[i]!=0.) average_LL[i]=N_LL[i]/counter_LL[i];
    if(counter_ML[i]!=0.) average_ML[i]=N_ML[i]/counter_ML[i];
```

```
    if(counter_HL[i]!=0.) average_HL[i]=N_HL[i]/counter_HL[i];
}
//SCALING
for(int i=0;i<size;i++){
     double temp1=average_ML[i]; average_ML[i]=(slo_LL/slo_ML)*temp1;
     double temp2=average_HL[i]; average_HL[i]=(slo_LL/slo_HL)*temp2;
}

//NORMALIZZAZIONE DELLE ORDINATE
double n_LL[size], n_ML[size], n_HL[size];
for(int i=0;i<size;i++){n_LL[i]=0., n_ML[i]=0., n_HL[i]=0.;}
for(int i=0;i<size;i++){
    if(Dy[i]!=0.){n_LL[i]=average_LL[i]/Dy[i];}
    if(Dy[i]!=0.){n_ML[i]=average_ML[i]/Dy[i];}
    if(Dy[i]!=0.){n_HL[i]=average_HL[i]/Dy[i];}
}
double total_events_LL=0., total_events_ML=0., total_events_HL=0.;
for(int i=0;i<size;i++){total_events_LL+=average_LL[i], total_events_ML+=average_ML[i],
    total_events_HL+=average_HL[i];}

//CALCOLO DISTRIBUZIONE IN FREQUENZA
double f_LL[size], f_ML[size], f_HL[size];
for(int i=0;i<size;i++){f_LL[i]=0., f_ML[i]=0., f_HL[i]=0.;}
double normalization_f_LL=0., normalization_f_ML=0., normalization_f_HL=0.;
for(int i=0;i<size;i++){normalization_f_LL+=average_LL[i]*Dy[i],
    normalization_f_ML+=average_ML[i]*Dy[i], normalization_f_HL+=average_HL[i]*Dy[i];}
for(int i=0;i<size;i++){f_LL[i]=average_LL[i]/normalization_f_LL,
    f_ML[i]=average_ML[i]/normalization_f_ML, f_HL[i]=average_HL[i]/normalization_f_HL;}

/*Codice x verifica normalizzazione della distribuzione f(y)*/
//double sum_f_LL=0., sum_f_ML=0., sum_f_HL=0.;
//for(int i=0;i<size;i++){sum_f_LL+=f_LL[i]*Dy[i], sum_f_ML+=f_ML[i]*Dy[i],
    sum_f_HL+=f_HL[i]*Dy[i];}
//qDebug() << sum_f_LL << " - " << sum_f_ML << " - " << sum_f_HL;

//CALCOLO ERRORI
double sigma_average_LL[size], sigma_average_ML[size], sigma_average_HL[size];
for(int i=0;i<size;i++){sigma_average_LL[i]=0., sigma_average_ML[i]=0.,
    sigma_average_HL[i]=0.;}
for(int i=0;i<size;i++){
    if(counter_LL[i]!=0.) sigma_average_LL[i]=sqrt(average_LL[i]);
    if(counter_ML[i]!=0.) sigma_average_ML[i]=sqrt(average_ML[i]);
    if(counter_HL[i]!=0.) sigma_average_HL[i]=sqrt(average_HL[i]);
}
double sigma_n_LL[size], sigma_n_ML[size], sigma_n_HL[size];
for(int i=0;i<size;i++){sigma_n_LL[i]=0., sigma_n_ML[i]=0., sigma_n_HL[i]=0.;}
/*vecchi errori n[i]*/
for(int i=0;i<size;i++){
    if(counter_LL[i]!=0.) sigma_n_LL[i]=sqrt(n_LL[i]/Dy[i]);
    if(counter_ML[i]!=0.) sigma_n_ML[i]=sqrt(n_ML[i]/Dy[i]);
    if(counter_HL[i]!=0.) sigma_n_HL[i]=sqrt(n_HL[i]/Dy[i]);
}

//SCRITTURA DEL FILE DI OUTPUT
string outfileLL=workdir+"/LL_calibrated.txt";
strcpy(outputfileLL, outfileLL.c_str());
ofstream OutputFileLL;
OutputFileLL.open(outputfileLL);
for(int i=0;i<size;i++) {
```

```
    OutputFileLL << y_comp[i] << " " << N_LL[i] << " " << counter_LL[i] << " " <<
        average_LL[i] << " " << sigma_average_LL[i] << " " << n_LL[i] << " " <<
        sigma_n_LL[i] << endl;
}
OutputFileLL.close();
string outfileML=workdir+"/ML_calibrated.txt";
strcpy(outputfileML, outfileML.c_str());
ofstream OutputFileML;
OutputFileML.open(outputfileML);
for(int i=0;i<size;i++) {
    OutputFileML << y_comp[i] << " " << N_ML[i] << " " << counter_ML[i] << " " <<
        average_ML[i] << " " << sigma_average_ML[i] << " " << n_ML[i] << " " <<
        sigma_n_ML[i] << endl;
}
OutputFileML.close();
string outfileHL=workdir+"/HL_calibrated.txt";
strcpy(outputfileHL, outfileHL.c_str());
ofstream OutputFileHL;
OutputFileHL.open(outputfileHL);
for(int i=0;i<size;i++) {
    OutputFileHL << y_comp[i] << " " << N_HL[i] << " " << counter_HL[i] << " " <<
        average_HL[i] << " " << sigma_average_HL[i] << " " << n_HL[i] << " " <<
        sigma_n_HL[i] << endl;
}
OutputFileHL.close();

return N;
}
```

A.3 Determination of the Cut Point

```
int giunta_2(std::string workdir, double y_min_1, double y_max_1, bool scalingLL, bool
    scalingLL_ML){

    char inputfileLL[400],inputfileML[400];
    string infileLL=workdir+"/LL_calibrated.txt";
    strcpy(inputfileLL, infileLL.c_str());
    string infileML=workdir+"/ML_calibrated.txt";
    if(scalingLL_ML==1){infileML=workdir+"/ML_calibrated_new.txt";}
    strcpy(inputfileML, infileML.c_str());

//LETTURA DIMENSIONE DEGLI ARRAY
ifstream InLL;
InLL.open(inputfileLL);
if (!InLL) {return 0;}
string sLL;
int DIMLL=0;
while(!InLL.eof()){getline(InLL,sLL,'\n');DIMLL++;}
InLL.close();
ifstream InML;
InML.open(inputfileML);
if (!InML) {return 0;}
string sML;
int DIMML=0;
while(!InML.eof()){getline(InML,sML,'\n');DIMML++;}
InML.close();
```

```
//LETTURA DEL FILE IN INPUT E INIZIALIZZAZIONE DEGLI ARRAY
ifstream InputFileLL;
InputFileLL.open(inputfileLL);
double y_mV[DIMLL-1], N_LL[DIMLL-1], counter_LL[DIMLL-1], average_LL[DIMLL-1],
    sigma_average_LL[DIMLL-1], n_LL[DIMLL-1], sigma_n_LL[DIMLL-1];
for(int i=0;i<DIMLL-1;i++){
InputFileLL >> y_mV[i] >> N_LL[i] >> counter_LL[i] >> average_LL[i] >>
    sigma_average_LL[i] >> n_LL[i] >> sigma_n_LL[i];
}
InputFileLL.close();
ifstream InputFileML;
InputFileML.open(inputfileML);
double N_ML[DIMML-1], counter_ML[DIMML-1], average_ML[DIMML-1],
    sigma_average_ML[DIMML-1], n_ML[DIMML-1], sigma_n_ML[DIMML-1];
for(int i=0;i<DIMML-1;i++){
InputFileML >> y_mV[i] >> N_ML[i] >> counter_ML[i] >> average_ML[i] >>
    sigma_average_ML[i] >> n_ML[i] >> sigma_n_ML[i];
}
InputFileML.close();

//IDENTIFICAZIONE DELLE REGIONI DI SOVRAPPOSIZIONE SCELTE DALL'UTENTE
int N_1=0, min_1=0, max_1=0;
for(int i=0;i<DIMLL-2;i++){
    if(y_mV[i]<=y_min_1) min_1=i+1;
    if(y_mV[i]>y_min_1 && y_mV[i]<=y_max_1) max_1=i;
}
N_1=max_1-min_1+1;

// CALCOLO COEFFICIENTI DEL FIT LINEARE DEI DATI
double x[N_1], yLL[N_1], yML[N_1], sigma_yLL[N_1], sigma_yML[N_1];
for(int i=0;i<N_1;i++){
   x[i]=log10(y_mV[min_1+i]);
   yLL[i]=log10(average_LL[min_1+i]);
   yML[i]=log10(average_ML[min_1+i]);
}

double intLL=0., sloLL=0., sigma_intLL=0., sigma_sloLL=0., devLL=0.;
double intML=0., sloML=0., sigma_intML=0., sigma_sloML=0., devML=0.;

lin_regr(N_1, x, yLL, intLL, sloLL, sigma_intLL, sigma_sloLL, devLL);
lin_regr(N_1, x, yML, intML, sloML, sigma_intML, sigma_sloML, devML);

// CALCOLO COMPATIBILITA' PENDENZE
double comp1=0.;
if(sloML>sloLL)
    comp1=(sloML-sloLL)*pow(sigma_sloLL*sigma_sloLL+sigma_sloML*sigma_sloML,-0.5);
if(sloML<sloLL)
    comp1=-(sloML-sloLL)*pow(sigma_sloLL*sigma_sloLL+sigma_sloML*sigma_sloML,-0.5);

qDebug() << "********";
qDebug() << sloLL << "+/-" << sigma_sloLL;
qDebug() << sloML << "+/-" << sigma_sloML;
qDebug() << "********";

//VALORI DEI CONTEGGI DAI FIT
double fit_LL[N_1], fit_ML[N_1];
for(int i=0;i<N_1;i++){
    fit_LL[i]=pow(10.,intLL+sloLL*x[i]);
    fit_ML[i]=pow(10.,intML+sloML*x[i]);
}
```

```
char junct1[400];
string out1=workdir+"/fit_junction_1.txt";
strcpy(junct1, out1.c_str());
ofstream OutputJunct1;
OutputJunct1.open(junct1);
OutputJunct1 << intLL << " " << sloLL << " " << devLL << intML << " " << sloML << " " <<
    devML << " " << comp1 << endl;
for(int i=0;i<N_1;i++){
    OutputJunct1 << y_mV[min_1+i] << " " << average_LL[min_1+i] << " " << fit_LL[i] << "
        " << y_mV[min_1+i] << " " << average_ML[min_1+i] << " " << fit_ML[i] << endl;
}
OutputJunct1.close();

/*****************************************************************************************/

if(scalingLL==1 || scalingLL_ML==1){
    for(int i=0;i<DIMLL-1;i++){
        double exp1=intML+(sloML/sloLL)*(log10(n_LL[i])-intLL);
        n_LL[i]=pow(10.,exp1);
        double exp2=intML+(sloML/sloLL)*(log10(average_LL[i])-intLL);
        average_LL[i]=pow(10.,exp2);
    }
    char out_LL_new[400];
    string out=workdir+"/LL_calibrated_new.txt";
    strcpy(out_LL_new, out.c_str());
    ofstream Output_LL_new;
    Output_LL_new.open(out_LL_new);
    for(int i=0;i<DIMLL-1;i++){
    Output_LL_new << y_mV[i] << " " << N_LL[i] << " " << counter_LL[i] << " " <<
        average_LL[i] << " " << sigma_average_LL[i] << " " << n_LL[i] << " " <<
        sigma_n_LL[i] << endl;
    }
    Output_LL_new.close();
}

//CALCOLO DIFFERENZE RELATIVE TRA SERIE DATI IN LOGARITMICO
double diff_log[N_1];
for(int i=0;i<N_1;i++) {
    double a=sloLL*x[i]+intLL;
    double b=sloML*x[i]+intML;
    diff_log[i]=(1.-b/a);
}

//ARRAY CON GLI ERRORI SULLE DIFFERENZE IN LOGARITMICO
double sigma_diff_log[N_1];
for(int i=0;i<N_1;i++){sigma_diff_log[i]=0.;}

for(int i=0;i<N_1;i++){
    double a=sloLL*x[i]+intLL;
    double b=sloML*x[i]+intML;
    double var_a=pow(sigma_sloLL*x[i],2.)+pow(sigma_intLL,2.);
    double var_b=pow(sigma_sloML*x[i],2.)+pow(sigma_intML,2.);
    sigma_diff_log[i]=pow(b*b*var_a/(a*a)+var_b,0.5)/a;
}

//CALCOLO DIFFERENZE RELATIVE TRA SERIE DATI IN LINEARE
double diff[N_1];
for(int i=0;i<N_1;i++) {
    double a=sloLL*x[i]+intLL;
```

```
    diff[i]=1.-pow(10.,-diff_log[i]*a);
}

//ARRAY CON GLI ERRORI SULLE DIFFERENZE IN LINEARE
double sigma_diff[N_1];
for(int i=0;i<N_1;i++){sigma_diff[i]=0.;}

for(int i=0;i<N_1;i++){
    double a=sloLL*x[i]+intLL;
    double var_a=pow(sigma_sloLL*x[i],2.)+pow(sigma_intLL,2.);
    sigma_diff[i]=pow(a*a*sigma_diff_log[i]*sigma_diff_log[i]+diff_log[i]*diff_log[i]*var_a,0.5)*log(10.);
}

//CALCOLO MEDIA PESATA DELLE DIFFERENZE TRA CONTEGGI
double sum_weights=0., num=0.;
double sigma_diff_counts[N_1];
for(int i=0;i<N_1;i++){sigma_diff_counts[i]=0.;}
for(int i=0;i<N_1;i++){
    sigma_diff_counts[i]=sqrt(sigma_average_LL[min_1+i]*sigma_average_LL[min_1+i]
    +sigma_average_ML[min_1+i]*sigma_average_ML[min_1+i]*average_LL[min_1+i]*average_LL[min_1+i]/
    (average_ML[min_1+i]*average_ML[min_1+i]))/average_ML[min_1+i];
}
for(int i=0;i<N_1;i++){sum_weights+=pow(sigma_diff_counts[i],-2.);}
for(int
     i=0;i<N_1;i++){num+=(1.-average_LL[min_1+i]/average_ML[min_1+i])*pow(sigma_diff_counts[i],-2.);}
double weighted_mean=num/sum_weights;
double sigma_mean=pow(sum_weights,-0.5);
qDebug() << "Media pesata campione 1:" << weighted_mean << "+/-" << sigma_mean;

//CALCOLO VARIANZA CAMPIONE DELLE DIFFERENZE TRA CONTEGGI
double single_var[N_1];
for(int
     i=0;i<N_1;i++){single_var[i]=pow((1.-average_LL[min_1+i]/average_ML[min_1+i])-weighted_mean,2.);}
double num_var=0.;
for(int i=0;i<N_1;i++){num_var+=single_var[i];}
double den_var=(N_1*1.-1.);
double var_sample=num_var/den_var;
qDebug() << "Varianza pesata campione 1:" << var_sample;

//CALCOLO DEI PUNTI DI TAGLIO, REGIONE DI MINIMO
double medie_var[N_1];
medie_var[0]=(single_var[0]+single_var[1]+single_var[2])/3.;
medie_var[1]=(single_var[0]+single_var[1]+single_var[2]+single_var[3])/4.;
medie_var[N_1-2]=(single_var[N_1-1]+single_var[N_1-2]+single_var[N_1-3]+single_var[N_1-4])/4.;
medie_var[N_1-1]=(single_var[N_1-1]+single_var[N_1-2]+single_var[N_1-3])/3.;
for(int i=2;i<N_1-2;i++){
    medie_var[i]=(single_var[i-2]+single_var[i-1]+single_var[i]+single_var[i+1]+single_var[i+2])/5.;
}

double min_var=medie_var[0], y_min_var=y_mV[min_1];
int index_min_var=0;
for(int i=0;i<N_1;i++){
    if(medie_var[i]<=min_var){min_var=medie_var[i], index_min_var=i;}
}
y_min_var=y_mV[min_1+index_min_var];

char outputvar1[400];
string outvar1=workdir+"/variances1.txt";
strcpy(outputvar1, outvar1.c_str());
ofstream OutputFileVar1;
```

```
OutputFileVar1.open(outputvar1);
OutputFileVar1 << y_min_var << " " << var_sample << endl;
for(int i=0;i<N_1;i++){
    OutputFileVar1 << y_mV[min_1+i] << " " << single_var[i]/(var_sample*den_var) << endl;
}
OutputFileVar1.close();

return DIMLL;
}

int giunta_3(std::string workdir, double y_min_2, double y_max_2, bool scalingLL_ML){

    char inputfileML[400],inputfileHL[400];
    string infileML=workdir+"/ML_calibrated.txt";
    strcpy(inputfileML, infileML.c_str());
    string infileHL=workdir+"/HL_calibrated.txt";
    strcpy(inputfileHL, infileHL.c_str());

//LETTURA DIMENSIONE DEGLI ARRAY
ifstream InML;
InML.open(inputfileML);
if (!InML) {return 0;}
string sML;
int DIMML=0;
while(!InML.eof()){getline(InML,sML,'\n');DIMML++;}
InML.close();
ifstream InHL;
InHL.open(inputfileHL);
if (!InHL) {return 0;}
string sHL;
int DIMHL=0;
while(!InHL.eof()){getline(InHL,sHL,'\n');DIMHL++;}
InHL.close();

//LETTURA DEL FILE IN INPUT E INIZIALIZZAZIONE DEGLI ARRAY
ifstream InputFileML;
InputFileML.open(inputfileML);
double y_mV[DIMML-1], N_ML[DIMML-1], counter_ML[DIMML-1], average_ML[DIMML-1],
    sigma_average_ML[DIMML-1], n_ML[DIMML-1], sigma_n_ML[DIMML-1];
for(int i=0;i<DIMML-1;i++){
InputFileML >> y_mV[i] >> N_ML[i] >> counter_ML[i] >> average_ML[i] >>
    sigma_average_ML[i] >> n_ML[i] >> sigma_n_ML[i];
}
InputFileML.close();
ifstream InputFileHL;
InputFileHL.open(inputfileHL);
double N_HL[DIMHL-1], counter_HL[DIMHL-1], average_HL[DIMHL-1],
    sigma_average_HL[DIMHL-1], n_HL[DIMHL-1], sigma_n_HL[DIMHL-1];
for(int i=0;i<DIMHL-1;i++){
InputFileHL >> y_mV[i] >> N_HL[i] >> counter_HL[i] >> average_HL[i] >>
    sigma_average_HL[i] >> n_HL[i] >> sigma_n_HL[i];
}
InputFileHL.close();

//IDENTIFICAZIONE DEMLE REGIONI DI SOVRAPPOSIZIONE SCELTE DALL'UTENTE
int N_1=0, min_1=0, max_1=0;
for(int i=0;i<DIMHL-2;i++){
    if(y_mV[i]<=y_min_2) min_1=i+1;
    if(y_mV[i]>y_min_2 && y_mV[i]<=y_max_2) max_1=i;
}
```

```
N_1=max_1-min_1+1;

// CALCOLO COEFFICIENTI DEL FIT LINEARE DEI DATI
double x[N_1], yML[N_1], yHL[N_1], sigma_yML[N_1], sigma_yHL[N_1];
for(int i=0;i<N_1;i++){
   x[i]=log10(y_mV[min_1+i]);
   yML[i]=log10(average_ML[min_1+i]);
   yHL[i]=log10(average_HL[min_1+i]);
}

double intML=0., sloML=0., sigma_intML=0., sigma_sloML=0., devML=0.;
double intHL=0., sloHL=0., sigma_intHL=0., sigma_sloHL=0., devHL=0.;

lin_regr(N_1, x, yML, intML, sloML, sigma_intML, sigma_sloML, devML);
lin_regr(N_1, x, yHL, intHL, sloHL, sigma_intHL, sigma_sloHL, devHL);

// CALCOLO COMPATIBILITA' PENDENZE
double comp1=0.;
if(sloHL>sloML)
    comp1=(sloHL-sloML)*pow(sigma_sloML*sigma_sloML+sigma_sloHL*sigma_sloHL,-0.5);
if(sloHL<sloML)
    comp1=-(sloHL-sloML)*pow(sigma_sloML*sigma_sloML+sigma_sloHL*sigma_sloHL,-0.5);

qDebug() << "********";
qDebug() << sloML << "+/-" << sigma_sloML;
qDebug() << sloHL << "+/-" << sigma_sloHL;
qDebug() << "********";

//VALORI DEI CONTEGGI DAI FIT
double fit_ML[N_1], fit_HL[N_1];
for(int i=0;i<N_1;i++){
    fit_ML[i]=pow(10.,intML+sloML*x[i]);
    fit_HL[i]=pow(10.,intHL+sloHL*x[i]);
}

char junct1[400];
string out1=workdir+"/fit_junction_2.txt";
strcpy(junct1, out1.c_str());
ofstream OutputJunct1;
OutputJunct1.open(junct1);
OutputJunct1 << intML << " " << sloML << " " << devML << intHL << " " << sloHL << " " <<
    devHL << " " << comp1 << endl;
for(int i=0;i<N_1;i++){
    OutputJunct1 << y_mV[min_1+i] << " " << average_ML[min_1+i] << " " << fit_ML[i] << "
        " << y_mV[min_1+i] << " " << average_HL[min_1+i] << " " << fit_HL[i] << endl;
}
OutputJunct1.close();

/*****************************************************************************************/

if(scalingLL_ML==1){
    for(int i=0;i<DIMML-1;i++){
        double exp1=intHL+(sloHL/sloML)*(log10(n_ML[i])-intML);
        n_ML[i]=pow(10.,exp1);
        double exp2=intHL+(sloHL/sloML)*(log10(average_ML[i])-intML);
        average_ML[i]=pow(10.,exp2);
    }
    char out_ML_new[400];
    string out=workdir+"/ML_calibrated_new.txt";
    strcpy(out_ML_new, out.c_str());
```

```
    ofstream Output_ML_new;
    Output_ML_new.open(out_ML_new);
    for(int i=0;i<DIMML-1;i++){
    Output_ML_new << y_mV[i] << " " << N_ML[i] << " " << counter_ML[i] << " " <<
        average_ML[i] << " " << sigma_average_ML[i] << " " << n_ML[i] << " " <<
        sigma_n_ML[i] << endl;
    }
    Output_ML_new.close();
}

//CALCOLO DIFFERENZE RELATIVE TRA SERIE DATI IN LOGARITMICO
double diff_log[N_1];
for(int i=0;i<N_1;i++) {
    double a=sloML*x[i]+intML;
    double b=sloHL*x[i]+intHL;
    diff_log[i]=(1.-b/a);
}

//ARRAY CON GLI ERRORI SULLE DIFFERENZE IN LOGARITMICO
double sigma_diff_log[N_1];
for(int i=0;i<N_1;i++){sigma_diff_log[i]=0.;}

for(int i=0;i<N_1;i++){
    double a=sloML*x[i]+intML;
    double b=sloHL*x[i]+intHL;
    double var_a=pow(sigma_sloML*x[i],2.)+pow(sigma_intML,2.);
    double var_b=pow(sigma_sloHL*x[i],2.)+pow(sigma_intHL,2.);
    sigma_diff_log[i]=pow(b*b*var_a/(a*a)+var_b,0.5)/a;
}

//CALCOLO DIFFERENZE RELATIVE TRA SERIE DATI IN LINEARE
double diff[N_1];
for(int i=0;i<N_1;i++) {
    double a=sloML*x[i]+intML;
    diff[i]=1.-pow(10.,-diff_log[i]*a);
}

//ARRAY CON GLI ERRORI SULLE DIFFERENZE IN LINEARE
double sigma_diff[N_1];
for(int i=0;i<N_1;i++){sigma_diff[i]=0.;}

for(int i=0;i<N_1;i++){
    double a=sloML*x[i]+intML;
    double var_a=pow(sigma_sloML*x[i],2.)+pow(sigma_intML,2.);
    sigma_diff[i]=pow(a*a*sigma_diff_log[i]*sigma_diff_log[i]
    +diff_log[i]*diff_log[i]*var_a,0.5)*log(10.);
}

//CALCOLO MEDIA PESATA DELLE DIFFERENZE TRA CONTEGGI
double sum_weights=0., num=0.;
double sigma_diff_counts[N_1];
for(int i=0;i<N_1;i++){sigma_diff_counts[i]=0.;}
for(int i=0;i<N_1;i++){
    sigma_diff_counts[i]=sqrt(sigma_average_ML[min_1+i]*sigma_average_ML[min_1+i]
    +sigma_average_HL[min_1+i]*sigma_average_HL[min_1+i]*average_ML[min_1+i]*average_ML[min_1+i]
    /(average_HL[min_1+i]*average_HL[min_1+i]))/average_HL[min_1+i];
}
for(int i=0;i<N_1;i++){sum_weights+=pow(sigma_diff_counts[i],-2.);}
for(int
     i=0;i<N_1;i++){num+=(1.-average_ML[min_1+i]/average_HL[min_1+i])*pow(sigma_diff_counts[i],-2.);}
```

```
double weighted_mean=num/sum_weights;
double sigma_mean=pow(sum_weights,-0.5);
qDebug() << "Media pesata campione 2:" << weighted_mean << "+/-" << sigma_mean;

//CALCOLO VARIANZA CAMPIONE DELLE DIFFERENZE TRA CONTEGGI
double single_var[N_1];
for(int
     i=0;i<N_1;i++){single_var[i]=pow((1.-average_ML[min_1+i]/average_HL[min_1+i])-weighted_mean,2.);}
double num_var=0.;
for(int i=0;i<N_1;i++){num_var+=single_var[i];}
double den_var=(N_1*1.-1.);
double var_sample=num_var/den_var;
qDebug() << "Varianza pesata campione 2:" << var_sample;

//CALCOLO DEI PUNTI DI TAGLIO, REGIONE DI MINIMO
double medie_var[N_1];
medie_var[0]=(single_var[0]+single_var[1]+single_var[2])/3.;
medie_var[1]=(single_var[0]+single_var[1]+single_var[2]+single_var[3])/4.;
medie_var[N_1-2]=(single_var[N_1-1]+single_var[N_1-2]+single_var[N_1-3]+single_var[N_1-4])/4.;
medie_var[N_1-1]=(single_var[N_1-1]+single_var[N_1-2]+single_var[N_1-3])/3.;
for(int i=2;i<N_1-2;i++){
    medie_var[i]=(single_var[i-2]+single_var[i-1]+single_var[i]+single_var[i+1]+single_var[i+2])/5.;
}

double min_var=medie_var[0], y_min_var=0.;
int index_min_var=0;
for(int i=0;i<N_1;i++){
    if(medie_var[i]<=min_var){
        min_var=medie_var[i];
        index_min_var=i;
}}
y_min_var=y_mV[min_1+index_min_var];

char outputvar1[400];
string outvar1=workdir+"/variances2.txt";
strcpy(outputvar1, outvar1.c_str());
ofstream OutputFileVar1;
OutputFileVar1.open(outputvar1);
OutputFileVar1 << y_min_var << " " << var_sample << endl;
for(int i=0;i<N_1;i++){
    OutputFileVar1 << y_mV[min_1+i] << " " << single_var[i]/(var_sample*den_var) << endl;
}
OutputFileVar1.close();

return DIMHL;
}

void join_spectra(std::string workdir, double cut12, double cut23, bool check2or3, bool
     scalingLL, bool scalingLL_ML){

    char inputfileLL[400],inputfileML[400],inputfileHL[400];
    string infileLL;
    if(scalingLL==0){infileLL=workdir+"/LL_calibrated.txt";}
    if(scalingLL==1 || scalingLL_ML==1){infileLL=workdir+"/LL_calibrated_new.txt";}
    strcpy(inputfileLL, infileLL.c_str());

    string infileML;
    if(scalingLL_ML==0){infileML=workdir+"/ML_calibrated.txt";}
    if(scalingLL_ML==1){infileML=workdir+"/ML_calibrated_new.txt";}
    strcpy(inputfileML, infileML.c_str());
```

```
string infileHL=workdir+"/HL_calibrated.txt";
strcpy(inputfileHL, infileHL.c_str());

//LETTURA DIMENSIONE DEGLI ARRAY
ifstream InLL;
InLL.open(inputfileLL);
if (!InLL) {return;}
string sLL;
int DIMLL=0;
while(!InLL.eof()){getline(InLL,sLL,'\n');DIMLL++;}
InLL.close();
ifstream InML;
InML.open(inputfileML);
if (!InML) {return;}
string sML;
int DIMML=0;
while(!InML.eof()){getline(InML,sML,'\n');DIMML++;}
InML.close();
ifstream InHL;
InHL.open(inputfileHL);
if (!InHL) {return;}
string sHL;
int DIMHL=0;
while(!InHL.eof()){getline(InHL,sHL,'\n');DIMHL++;}
InHL.close();

//LETTURA DEL FILE IN INPUT E INIZIALIZZAZIONE DEGLI ARRAY
ifstream InputFileLL;
InputFileLL.open(inputfileLL);
double y_mV[DIMLL-1], N_LL[DIMLL-1], counter_LL[DIMLL-1], average_LL[DIMLL-1],
    sigma_average_LL[DIMLL-1], n_LL[DIMLL-1], sigma_n_LL[DIMLL-1];
for(int i=0;i<DIMLL-1;i++){
InputFileLL >> y_mV[i] >> N_LL[i] >> counter_LL[i] >> average_LL[i] >>
    sigma_average_LL[i] >> n_LL[i] >> sigma_n_LL[i];
}
InputFileLL.close();
ifstream InputFileML;
InputFileML.open(inputfileML);
double N_ML[DIMML-1], counter_ML[DIMML-1], average_ML[DIMML-1],
    sigma_average_ML[DIMML-1], n_ML[DIMML-1], sigma_n_ML[DIMML-1];
for(int i=0;i<DIMML-1;i++){
InputFileML >> y_mV[i] >> N_ML[i] >> counter_ML[i] >> average_ML[i] >>
    sigma_average_ML[i] >> n_ML[i] >> sigma_n_ML[i];
}
InputFileML.close();
ifstream InputFileHL;
InputFileHL.open(inputfileHL);
double N_HL[DIMHL-1], counter_HL[DIMHL-1], average_HL[DIMHL-1],
    sigma_average_HL[DIMHL-1], n_HL[DIMHL-1], sigma_n_HL[DIMHL-1];
for(int i=0;i<DIMHL-1;i++){
InputFileHL >> y_mV[i] >> N_HL[i] >> counter_HL[i] >> average_HL[i] >>
    sigma_average_HL[i] >> n_HL[i] >> sigma_n_HL[i];
}
InputFileHL.close();

char outputfile[400];
string outfile=workdir+"/giunta.txt";
strcpy(outputfile, outfile.c_str());
ofstream OutputFile;
```

```
    OutputFile.open(outputfile);

    if(check2or3==0){
    for(int i=0;i<DIMLL-2;i++) {
      if(y_mV[i]<=cut12){OutputFile << y_mV[i] << " " << N_LL[i] << " " << counter_LL[i]
          << " " << average_LL[i] << " " << sigma_average_LL[i] << " " << n_LL[i] << " "
          << sigma_n_LL[i] << endl;}
      if(y_mV[i]>cut12){OutputFile << y_mV[i] << " " << N_ML[i] << " " << counter_ML[i]
          << " " << average_ML[i] << " " << sigma_average_ML[i] << " " << n_ML[i] << " "
          << sigma_n_ML[i] << endl;}
    }
    }
    if(check2or3==1){
    for(int i=0;i<DIMLL-2;i++) {
      if(y_mV[i]<=cut12){OutputFile << y_mV[i] << " " << N_LL[i] << " " << counter_LL[i]
          << " " << average_LL[i] << " " << sigma_average_LL[i] << " " << n_LL[i] << " "
          << sigma_n_LL[i] << endl;}
      if(y_mV[i]>cut12 && y_mV[i]<=cut23){OutputFile << y_mV[i] << " " << N_ML[i] << " "
          << counter_ML[i] << " " << average_ML[i] << " " << sigma_average_ML[i] << " "
          << n_ML[i] << " " << sigma_n_ML[i] << endl;}
      if(y_mV[i]>cut23){ OutputFile << y_mV[i] << " " << N_HL[i] << " " << counter_HL[i]
          << " " << average_HL[i] << " " << sigma_average_HL[i] << " " << n_HL[i] << " "
          << sigma_n_HL[i] << endl;}
    }
    }

    OutputFile.close();
}
```

A.4 Microdosimetric Spectra and Uncertainties

```
int rebin(std::string workdir, int no_intervals, long double y_min, double total_counts){

    char inputfile[400];
    string infile=workdir+"/giunta.txt";
    strcpy(inputfile, infile.c_str());

int B = no_intervals; //numero intervallini per decade

//LETTURA DIMENSIONE DEGLI ARRAY
ifstream In;
In.open(inputfile);
if (!In) {return 0;}
string s;
int DIM=0;
while(!In.eof()){getline(In,s,'\n');DIM++;}
In.close();

//LETTURA DEL FILE IN INPUT E INIZIALIZZAZIONE DEGLI ARRAY
ifstream InputFile;
InputFile.open(inputfile);
double y_mV[DIM-1], N_old[DIM-1], counter_old[DIM-1], average_old[DIM-1],
    sigma_average_old[DIM-1], n_old[DIM-1], sigma_n_old[DIM-1];
for(int i=0;i<DIM-1;i++){
InputFile >> y_mV[i] >> N_old[i] >> counter_old[i] >> average_old[i] >>
    sigma_average_old[i] >> n_old[i] >> sigma_n_old[i];
}
```

```
InputFile.close();

/*****************************************************************************************/

//SETTAGGIO DEGLI ESPONENTI DI 10 MINIMO E MASSIMO DELLO SPETTRO MICRODOSIMETRICO
double min_mV=y_min, max_mV=1.;
for(int i=0;i<DIM;i++) {
  if(y_mV[i]>max_mV){max_mV=y_mV[i];}
}

int e_min, e_max;
 { long double temp1=log10(min_mV); e_min=floor(temp1);
   long double temp2=log10(max_mV); e_max=floor(temp2+1.);}
int Num=e_max-e_min; //numero di decadi

//SETTAGGIO DEGLI ESTREMI DELLE DECADI

long double y0[Num+1];
for(int i=0;i<Num+1;i++){y0[i]=pow(10,e_min+i);}

/*****************************************************************************************/

//DEFINIZIONE DEGLI ARRAY PER IL COMPATTAMENTO E INIZIALIZZAZIONE A ZERO
int D=Num*B;
double y_comp[D], N[D];
for(int i=0;i<D;i++){y_comp[i]=0., N[i]=0.;}

//CALCOLO DELLE y COMPATTATE
for(int j=0;j<Num;j++){for(int i=j*B;i<(j+1)*B;i++){
  double a=i*1., b=j*1., c=B*1., exp=(a-b*c)/c;
  y_comp[i]=y0[j]*pow(10.,exp);
}}

//CALCOLO DEGLI INTERVALLI DELTA_y
double Dy[D];
for(int i=0;i<D;i++){Dy[i]=0.;}
for(int i=0;i<D;i++){Dy[i]=y_comp[i]*(pow(10,0.5/B)-pow(10,-0.5/B));}

//COUNTER
int counter[D];
for(int i=0;i<D;i++){counter[i]=0;}

//REBINNING DELLE ORDINATE
for(int i=0;i<DIM;i++){
  if(y_mV[i]!=0.&&N_old[i]!=0.){
  for(int j=0;j<D;j++){
    double Delta_inf, Delta_sup;
    if(j==0){Delta_inf=0.;} else {Delta_inf=(y_comp[j]-y_comp[j-1])*0.5;}
    if(j==D-1){Delta_sup=0.;} else {Delta_sup=(y_comp[j+1]-y_comp[j])*0.5;}

    if(y_mV[i]>=y_comp[j]-Delta_inf && y_mV[i]<y_comp[j]+Delta_sup){N[j]+=average_old[i];}
}}}

for(int i=0;i<DIM;i++){
    for(int j=1;j<D-1;j++){
        if(y_mV[i]>=y_comp[j]-(y_comp[j]-y_comp[j-1])*0.5 &&
            y_mV[i]<y_comp[j]+(y_comp[j+1]-y_comp[j])*0.5) counter[j]++;
    }
}
```

```
//CALCOLO MEDIE
double average[D];
for(int i=0;i<D;i++){average[i]=0.;}
for(int i=0;i<D;i++){
    if(counter[i]!=0.) average[i]=N[i]/counter[i];
}

//NORMALIZZAZIONE DELLE ORDINATE
double n[D];
for(int i=0;i<D;i++){n[i]=0.;}
for(int i=0;i<D;i++){
    if(Dy[i]!=0.){n[i]=average[i]/Dy[i];}
}

//FATTORE DI NORMALIZZAZIONE PER LA DISTRIBUZIONE IN FREQUENZA
    double norma_F=0.;
    for(int i=0;i<D;i++){norma_F+=average[i]*Dy[i];}

//FATTORE DI NORMALIZZAZIONE PER LA DISTRIBUZIONE IN DOSE
    double norma_D=0.;
    for(int i=0;i<D;i++){norma_D+=average[i]*y_comp[i]*Dy[i];}

//CALCOLO DISTRIBUZIONE IN FREQUENZA
    double f_y[D];
    for(int i=0;i<D;i++){f_y[i]=average[i]/norma_F;}

//CALCOLO DISTRIBUZIONE IN DOSE
    double d_y[D];
    for(int i=0;i<D;i++){d_y[i]=y_comp[i]*average[i]/norma_D;}

/*****************************************************************************************/

//SCRITTURA DEI FILES DI OUTPUT
char outputfile[400];
string outfile=workdir+"/giunta_compat.txt";
strcpy(outputfile, outfile.c_str());
ofstream OutputFile;
OutputFile.open(outputfile);
    for(int i=0;i<D;i++) {
      OutputFile << y_comp[i] << " " << N[i] << " " << average[i] << " " << Dy[i] << " "
          << f_y[i]
                << " " << d_y[i] << " " << y_comp[i]*f_y[i] << " " << y_comp[i]*d_y[i] <<
                    endl;
    }

//VERIFICA DELLA NORMALIZZAZIONE DELLE DISTRIBUZIONI
    double integr_F=0., integr_D=0.;
    for(int i=0;i<D;i++) {integr_F+=Dy[i]*f_y[i]; integr_D+=Dy[i]*d_y[i];}
    qDebug() << "Integrale in frequenza pari a " << integr_F << ", integrale in dose pari
        a " << integr_D;

OutputFile.close();

/*****************************************************************************************/

//CALCOLO ERRORI
double no_events=total_counts;

double sigma_average[D];
for(int i=0;i<D;i++){sigma_average[i]=0.;}
```

```
for(int i=0;i<D;i++){
    sigma_average[i]=sqrt(average[i]);
}

double sigma_n[D];
for(int i=0;i<D;i++){sigma_n[i]=0.;}
for(int i=0;i<D;i++){
    if(Dy[i]!=0.) sigma_n[i]=sqrt(n[i]/Dy[i]);
}

double sigma_f_y[D], sigma_d_y[D], sigma_yf_y[D], sigma_yd_y[D];
for(int i=0;i<D;i++){sigma_f_y[i]=0., sigma_d_y[i]=0., sigma_yf_y[i]=0.,
    sigma_yd_y[i]=0.;}

//nuovo sigma f(y)
for(int i=0;i<D;i++){sigma_f_y[i]=sqrt(f_y[i]/(Dy[i]*no_events));}

//nuovo sigma y*f(y)
for(int i=0;i<D;i++){sigma_yf_y[i]=sigma_f_y[i]*y_comp[i];}

//calcolo y_bar_F
double y_bar_F=0., sigma_y_bar_F=0., sum_for_sigma_y_bar_F=0.;
for(int i=0;i<D;i++){y_bar_F+=y_comp[i]*f_y[i]*Dy[i];}
for(int j=0;j<D;j++){
for(int i=0;i<D;i++){sum_for_sigma_y_bar_F+=pow(y_comp[i]*Dy[i]*sigma_f_y[i],2.);}
}
sigma_y_bar_F=sqrt(sum_for_sigma_y_bar_F);

qDebug() << "y_bar_F" << y_bar_F << "+/-" << sigma_y_bar_F;

double sum_for_sigma_d_y[D];
for(int i=0;i<D;i++){sum_for_sigma_d_y[i]=0.;}
for(int i=0;i<D;i++){
    for(int j=0;j<D;j++){
        if(j!=i && average[j]!=0.)
        {sum_for_sigma_d_y[i]+=pow(d_y[i]*d_y[j]*Dy[j]*sigma_average[j]/average[j],2.);}
    }
}
for(int i=0;i<D;i++){
    if(average[i]=!0.){sigma_d_y[i]=pow(d_y[i]*(1-d_y[i]*Dy[i])*sigma_average[i]/average[i],2.);}
}
for(int i=0;i<D;i++){sigma_d_y[i]+=sum_for_sigma_d_y[i];}

//nuovo sigma d(y)
for(int i=0;i<D;i++){if(f_y[i]!=0.)
    sigma_d_y[i]=d_y[i]*sqrt(pow(sigma_f_y[i]/f_y[i],2.)+pow(sigma_y_bar_F/y_bar_F,2.));}

//nuovo sigma y*d(y)
for(int i=0;i<D;i++){sigma_yd_y[i]=sigma_d_y[i]*y_comp[i];}

char outputfile_errori[400];
string outfile_errori=workdir+"/giunta_compat_errori.txt";
strcpy(outputfile_errori, outfile_errori.c_str());
ofstream OutputFile_errori;
OutputFile_errori.open(outputfile_errori);
    for(int i=0;i<D;i++) {
      OutputFile_errori << y_comp[i] << " " << sigma_average[i] << " " << sigma_f_y[i] <<
          " " << sigma_d_y[i] << " " << sigma_yf_y[i] << " " << sigma_yd_y[i] << endl;
    }
```

```
OutputFile_errori.close();

return D;
}
```

A.5 Fermi Fit

```
void error_matrix(double A, double B, double C, int D, double x[], double y[], double
     sigma_y[], double& sigma_A, double& sigma_B, double& sigma_C){
    double dy_dA[D], dy_dB[D], dy_dC[D];
    for(int i=0;i<D;i++){
      dy_dA[i]=pow(1.+exp(B*x[i]-B*C),-1);
      dy_dB[i]=-A*pow(dy_dA[i],2)*exp(B*x[i]-B*C)*(x[i]-C);
      dy_dC[i]=-dy_dB[i]*B/(x[i]-C);
    }

    double a[3][3];
    for(int i=0;i<3;i++){a[0][i]=0., a[1][i]=0., a[2][i]=0.;}
    for(int i=0;i<D;i++){a[0][0]+=pow(dy_dA[i],2)/(sigma_y[i]*sigma_y[i]);}
    for(int i=0;i<D;i++){a[1][1]+=pow(dy_dB[i],2)/(sigma_y[i]*sigma_y[i]);}
    for(int i=0;i<D;i++){a[2][2]+=pow(dy_dC[i],2)/(sigma_y[i]*sigma_y[i]);}
    for(int i=0;i<D;i++){a[0][1]+=dy_dA[i]*dy_dB[i]/(sigma_y[i]*sigma_y[i]);}
    for(int i=0;i<D;i++){a[0][2]+=dy_dA[i]*dy_dC[i]/(sigma_y[i]*sigma_y[i]);}
    for(int i=0;i<D;i++){a[1][2]+=dy_dB[i]*dy_dC[i]/(sigma_y[i]*sigma_y[i]);}
    a[1][0]=a[0][1];
    a[2][0]=a[0][2];
    a[2][1]=a[1][2];

    double det=a[0][0]*(a[1][1]*a[2][2]-a[2][1]*a[1][2])-a[0][1]*(a[1][0]*a[2][2]
             -a[2][0]*a[1][2])+a[0][2]*(a[1][0]*a[2][1]-a[2][0]*a[1][1]);

    double inv[3][3];
    inv[0][0]=(a[1][1]*a[2][2]-a[1][2]*a[2][1])/det;
    inv[0][1]=(a[0][2]*a[2][1]-a[0][1]*a[2][2])/det;
    inv[0][2]=(a[0][1]*a[1][2]-a[0][2]*a[1][1])/det;

    inv[1][0]=(a[1][2]*a[2][0]-a[1][0]*a[2][2])/det;
    inv[1][1]=(a[0][0]*a[2][2]-a[0][2]*a[2][0])/det;
    inv[1][2]=(a[0][2]*a[1][0]-a[0][0]*a[1][2])/det;

    inv[2][0]=(a[1][0]*a[2][1]-a[1][1]*a[2][0])/det;
    inv[2][1]=(a[0][1]*a[2][0]-a[2][1]*a[0][0])/det;
    inv[2][2]=(a[0][0]*a[1][1]-a[0][1]*a[1][0])/det;

    sigma_A=sqrt(inv[0][0]);
    sigma_B=pow(inv[1][1],0.5);
    sigma_C=pow(inv[2][2],0.5);
}

//-----------------------------------------------------------------------------------------------------------------

double fit(double& lambda, double& guess_A, double& guess_B, double& guess_C, int D,
     double x[], double y[], double sigma_y[]){

    double chisquare=0.;
    double f_x[D];
    for(int i=0;i<D;i++){f_x[i]=guess_A*pow(1.+exp(guess_B*x[i]-guess_B*guess_C),-1);}
```

```
    for(int i=0;i<D;i++){
      chisquare+=pow(y[i]-f_x[i],2)/y[i];
    }

    qDebug() << "old chi-square: " << chisquare;

/*****************************************************************************************************/

    double dy_dA[D], dy_dB[D], dy_dC[D];
    for(int i=0;i<D;i++){
      dy_dA[i]=pow(1.+exp(guess_B*x[i]-guess_B*guess_C),-1);
      dy_dB[i]=-guess_A*pow(dy_dA[i],2)*exp(guess_B*x[i]-guess_B*guess_C)*(x[i]-guess_C);
      dy_dC[i]=-dy_dB[i]*guess_B/(x[i]-guess_C);
    }

    double alpha[3][3];
    for(int i=0;i<3;i++){alpha[0][i]=0., alpha[1][i]=0., alpha[2][i]=0.;}
    for(int i=0;i<D;i++){alpha[0][0]+=pow(dy_dA[i],2)/(sigma_y[i]*sigma_y[i]);}
    for(int i=0;i<D;i++){alpha[1][1]+=pow(dy_dB[i],2)/(sigma_y[i]*sigma_y[i]);}
    for(int i=0;i<D;i++){alpha[2][2]+=pow(dy_dC[i],2)/(sigma_y[i]*sigma_y[i]);}
    for(int i=0;i<D;i++){alpha[0][1]+=dy_dA[i]*dy_dB[i]/(sigma_y[i]*sigma_y[i]);}
    for(int i=0;i<D;i++){alpha[0][2]+=dy_dA[i]*dy_dC[i]/(sigma_y[i]*sigma_y[i]);}
    for(int i=0;i<D;i++){alpha[1][2]+=dy_dB[i]*dy_dC[i]/(sigma_y[i]*sigma_y[i]);}
    alpha[1][0]=alpha[0][1];
    alpha[2][0]=alpha[0][2];
    alpha[2][1]=alpha[1][2];

    double alpha_new[3][3];

    for(int k=0;k<3;k++){
        for(int l=0;l<3;l++){
            if(k==l) alpha_new[k][l]=alpha[k][l]*(1.+lambda);
            if(k!=l) alpha_new[k][l]=alpha[k][l];
        }
    }

    double X[3][3]; //The inverse of alpha_new
    double det; //The determinant of alpha_new

    double a = alpha_new[0][0]*( alpha_new[1][1]*alpha_new[2][2] -
        alpha_new[2][1]*alpha_new[1][2] );
    double b = alpha_new[0][1]*( alpha_new[1][0]*alpha_new[2][2] -
        alpha_new[2][0]*alpha_new[1][2] );
    double c = alpha_new[0][2]*( alpha_new[1][0]*alpha_new[2][1] -
        alpha_new[2][0]*alpha_new[1][1] );
    det = a - b + c;

    // Calculate the inverse matrix
    X[0][0]=(alpha_new[1][1]*alpha_new[2][2]-alpha_new[1][2]*alpha_new[2][1])/det;
    X[0][1]=(alpha_new[0][2]*alpha_new[2][1]-alpha_new[0][1]*alpha_new[2][2])/det;
    X[0][2]=(alpha_new[0][1]*alpha_new[1][2]-alpha_new[0][2]*alpha_new[1][1])/det;

    X[1][0]=(alpha_new[1][2]*alpha_new[2][0]-alpha_new[1][0]*alpha_new[2][2])/det;
    X[1][1]=(alpha_new[0][0]*alpha_new[2][2]-alpha_new[0][2]*alpha_new[2][0])/det;
    X[1][2]=(alpha_new[0][2]*alpha_new[1][0]-alpha_new[0][0]*alpha_new[1][2])/det;

    X[2][0]=(alpha_new[1][0]*alpha_new[2][1]-alpha_new[1][1]*alpha_new[2][0])/det;
    X[2][1]=(alpha_new[0][1]*alpha_new[2][0]-alpha_new[2][1]*alpha_new[0][0])/det;
    X[2][2]=(alpha_new[0][0]*alpha_new[1][1]-alpha_new[0][1]*alpha_new[1][0])/det;
```

```
    //increments
    double dA=0., dB=0., dC=0.;

    double beta[3];
    for(int k=0;k<3;k++){beta[k]=0.;}

    for(int i=0;i<D;i++){beta[0]+=(y[i]-f_x[i])*dy_dA[i]/(sigma_y[i]*sigma_y[i]);}
    for(int i=0;i<D;i++){beta[1]+=(y[i]-f_x[i])*dy_dB[i]/(sigma_y[i]*sigma_y[i]);}
    for(int i=0;i<D;i++){beta[2]+=(y[i]-f_x[i])*dy_dC[i]/(sigma_y[i]*sigma_y[i]);}

    for(int k=0;k<3;k++){dA+=beta[k]*X[0][k], dB+=beta[k]*X[1][k], dC+=beta[k]*X[2][k];}

    double chisquare_new=0.;
    double f_x_new[D];
    for(int
        i=0;i<D;i++){f_x_new[i]=(guess_A+dA)*pow(1.+exp((guess_B+dB)*x[i]-(guess_B+dB)*(guess_C+dC)),-1);}

    for(int i=0;i<D;i++){
      chisquare_new+=pow(y[i]-f_x_new[i],2)/y[i];
    }
    qDebug() << "new chi-square: " << chisquare_new;

    qDebug() << "A= " << guess_A << " + " << dA;
    qDebug() << "B= " << guess_B << " + " << dB;
    qDebug() << "C= " << guess_C << " + " << dC << endl;

    if(chisquare_new>=chisquare) {double temp=lambda; lambda=temp*10.;}//lambda=temp*1.1
    if(chisquare_new<chisquare) {double temp=lambda; lambda=temp/10.;
        guess_A+=dA,guess_B+=dB,guess_C+=dC;}//lambda=temp/1.1

    double diff;
    if(chisquare_new>=chisquare) diff=chisquare_new-chisquare;
    if(chisquare_new<chisquare) diff=chisquare-chisquare_new;

  return diff;
}

//-------------------------------------------------------------------------------------------------------------------

int exp_fit(std::string workdir, double start, double stop){

    char inputfile[400];
    string infile=workdir+"/giunta_compat.txt";
    strcpy(inputfile, infile.c_str());
    char inputfile_errors[400];
    string infile_errors=workdir+"/giunta_compat_errori.txt";
    strcpy(inputfile_errors, infile_errors.c_str());
    char outputfile[400];
    string outfile=workdir+"/fermi_fit.txt";
    strcpy(outputfile, outfile.c_str());

    ifstream In;
    In.open(inputfile);

    if (!In) {return 0;}
    string s;
    int DIM=0;
    while(!In.eof()){getline(In,s,'\n');DIM++;}
```

```
    In.close();

/*****************************************************************************************************/

    ifstream InputFile;
    InputFile.open(inputfile);

    double y_comp[DIM-1], average[DIM-1], n_norm_comp[DIM-1], Dy[DIM-1], f_y[DIM-1],
        d_y[DIM-1], yf_y[DIM-1], yd_y[DIM-1];
    for(int i=0;i<DIM-1;i++){y_comp[0]=0., average[0]=0., n_norm_comp[0]=0., Dy[0]=0.,
        f_y[0]=0., d_y[0]=0., yf_y[0]=0., yd_y[0]=0.;}

    for(int i=0;i<DIM-1;i++){
    InputFile >> y_comp[i] >> average[i] >> n_norm_comp[i] >> Dy[i] >> f_y[i] >> d_y[i]
        >> yf_y[i] >> yd_y[i];
    }
    InputFile.close();

    ifstream InputFile_errors;
    InputFile_errors.open(inputfile_errors);

    double sigma_average[DIM-1], sigma_f_y[DIM-1], sigma_d_y[DIM-1], sigma_yf_y[DIM-1],
        sigma_yd_y[DIM-1];
    for(int i=0;i<DIM-1;i++){sigma_average[0]=0., sigma_f_y[0]=0., sigma_d_y[0]=0.,
        sigma_yf_y[0]=0., sigma_yd_y[0]=0.;}

    for(int i=0;i<DIM-1;i++){
    InputFile_errors >> y_comp[i] >> sigma_average[i] >> sigma_f_y[i] >> sigma_d_y[i] >>
        sigma_yf_y[i] >> sigma_yd_y[i];
    }
    InputFile_errors.close();


/*****************************************************************************************************/

    int N=0, min=0, max=0;
    for(int i=0;i<DIM-1;i++){
        if(start>=y_comp[i] && start<y_comp[i+1]) min=i;
        if(stop>=y_comp[i] && stop<y_comp[i+1]) max=i;
    }

    N=max-min;

    double mV_data[N+1], yd_y_data[N+1], sigma_yd_y_data[N+1];
    for(int i=0;i<N+1;i++){mV_data[i]=0., yd_y_data[i]=0., sigma_yd_y_data[i]=0.;}
    for(int i=0;i<N+1;i++){
        mV_data[i]=(y_comp[min+i]);
        yd_y_data[i]=yd_y[min+i];
        sigma_yd_y_data[i]=yd_y_data[min+i];
    }

    double max_value=yd_y_data[0], max_key=mV_data[0];
    for(int i=0;i<N+1;i++){if(yd_y_data[i]>max_value) {max_value=yd_y_data[i],
         max_key=mV_data[i];}}

    double min_value=yd_y_data[0], min_key=mV_data[0];
    for(int i=0;i<N+1;i++){if(yd_y_data[i]<min_value) {min_value=yd_y_data[i],
         min_key=mV_data[i];}}

    double guess_A=max_value-min_value;
```

```
    double guess_C=0.5*(min_key+max_key)*(2./3.);

    double sum_guess_B=0.; int counts=0;
    for(int i=0;i<N+1;i++){
        if(guess_A/yd_y_data[i]-1.>0){sum_guess_B+=log(guess_A/yd_y_data[i]-1.)/(mV_data[i]-guess_C);
            counts++;}
    }
    double guess_B=sum_guess_B/(1.*counts);

    qDebug() << "Initial set: " << guess_A << " " << guess_B << " " << guess_C;

/*****************************************************************************************************/

    double lambda=0.001;//lambda=0.1

    double diff=fit(lambda,guess_A,guess_B,guess_C, N+1, mV_data, yd_y_data,
        sigma_yd_y_data);

    int counter=0;
    while(diff>=0.003){
        diff=fit(lambda,guess_A,guess_B,guess_C, N+1, mV_data, yd_y_data,
            sigma_yd_y_data); counter++;
        qDebug() << " --- iteration no.: " << counter;
        qDebug() << "A: " << guess_A << ", B: " << guess_B << ", C: " << guess_C << ",
            lambda: " << lambda;
    }

    qDebug() << "Final set: " << guess_A << " " << guess_B << " " << guess_C << " ---
        iteration no.: " << counter;

    double A=guess_A, B=guess_B, C=guess_C;

    double sigma_A=0., sigma_B=0., sigma_C=0.;

    error_matrix(A, B, C, N+1, mV_data, yd_y_data, sigma_yd_y_data, sigma_A, sigma_B,
        sigma_C);

/*****************************************************************************************************/

    ofstream OutputFile;
    OutputFile.open(outputfile);

    OutputFile << A << " " << B << " " << C << endl;
    OutputFile << sigma_A << " " << sigma_B << " " << sigma_C << endl;

    for(int i=0;i<N+1;i++){
        OutputFile << mV_data[i] << " " << yd_y_data[i] << " " <<
            A/(1.+exp(B*(mV_data[i]-C))) << endl;
    }
    OutputFile.close();

    return DIM;
}
```

Bibliography

[1] R. Orecchia et al. - *Particle Beam Therapy: Basis for Interest and Clinical Experience* - European Journal of Cancer vol. 4, 459-468 (1998)

[2] International Commission on Radiation Units and Measurements - *Linear Energy Transfer, ICRU Report no. 16*- Bethesda, MD (1970)

[3] International Commission on Radiation Units and Measurements - *Fundamental Quantities and Units for Ionizing Radiation (Revised), ICRU Report no. 85*- Bethesda, MD (2011)

[4] U. Amaldi, G. Kraft - *Radiotherapy with Beams of Carbon Ions* - Reports on Progress in Physics vol. 68, 1861-1882 (2005)

[5] J. Wilkens, U. Oelfke - *Direct Comparison of Biologically Optimized Spread-Out Bragg Peaks for Protons and Carbon Ions* - International Journal of Radiation Oncology • Biology • Physics vol. 70, 262-266 (2008)

[6] F.J. Currell (Ed.) - *The Physics of Multiply and Highly Charged Ions. Volume 1: Sources, Applications and Fundamental Processes* - Kluwer Academic Publishers (2003)

[7] A. Peeters, J.P.C. Grutters, M. Pijls-Johannesma, S. Reimoser, D. De Ruysscher, J.L. Severens, M.A. Joore, P. Lambin - *How Costly is Particle Therapy? Cost Analysis of External Beam Radiotherapy with Carbon-Ions, Protons and Photons* - Radiotherapy and Oncology vol. 95, 45–53 (2010)

[8] B. Douglas, J. Fowler - *The Effect of Multiple Small Doses of X Rays on Skin Reactions in the Mouse and a Basic Interpretation* - Radiation Research vol. 66, 401-426 (1976)

[9] G.W. Barendsen - *Impairment of the Proliferative Capacity of Human Cells in Culture by α-Particles with Differing Linear Energy Transfer* - International Journal of Radiation Biology vol. 8, 453–466 (1964)

[10] B.S. Sørensen, J. Overgaard, N. Bassler - *In Vitro RBE-LET Dependence for Multiple Particle Types* - Acta Oncologica vol. 50, 757-762 (2011)

[11] N. Matsufuji, T. Kanai, N. Kanematsu, T. Miyamoto, M. Baba, T. Kamada, H. Kato, S. Yamada, J. Mitzoe, H. Tsujii - *Specification of Carbon Ion Dose at the National Institute of Radiological Sciences (NIRS)* - Journal of Radiation Research vol. 48, A81-A86 (2007)

[12] H. Tsujii, T. Kamada, T. Shirai, K. Noda, H. Tsuji, K. Karasawa - *Carbon-Ion Radiotherapy. Principles, Practices, and Treatment Planning* - Springer Japan (2014)

[13] J. Gueulette, A. Wambersie - *Comparison of the Methods of Specifying Carbon Ion Doses at NIRS and GSI* - Journal of Radiation Research vol. 48, A97-A102 (2007)

[14] M. Scholz, A.M. Kellerer, W. Kraft-Weyrather, G. Kraft - *Computation of cell survival in heavy ion beams for therapy. The model and its approximation* - Radiation and Environmental Biophysics vol. 36, 59-66 (1997)

[15] M.A. Hill. - *Radiation Damage to DNA: the Importance of Track Structure* - Radiation Measurements vol. 31, 15-23 (1999)

[16] M.R. Raju - *Proton Radiobiology, Radiosurgery and Radiotherapy* - International Journal of Radiation Biology vol. 67, 237-259 (1995)

[17] H. Paganetti - *Significance and implementation of RBE variations in proton beam therapy* - Technology in Cancer Research and Treatment vol. 2, 413-26 (2003)

[18] F.M. Khan - *The Physics of Radiation Therapy* - Lippincott Williams & Wilkins (2003)

[19] M.R. Raju - *Heavy Particle Radiotherapy* - Academic Press (1980)

[20] K.R. Kase, B.E. Bjärngard, F.H.Attix - *The Dosimetry of Ionizing Radiation, Volume II* - Academic Press, Inc. (1987)

[21] H.H. Rossi - *The Role of Microdosimetry in Radiobiology* - Radiation and Environmental Biophysics vol. 17, 29-40 (1979)

[22] P. Olko - *Fluctuations of Energy Deposited in Biological Targets by Ionising Radiation* - Thesis at the Institute of Nuclear Physics of Krakow (1989)

[23] P. Pihet, H.G. Menzel, R.Schmidt, M. Beauduin, A. Wambersie - *Biological Weighting Function for RBE Specification of Neutron Therapy Beams. Intercomparison of 9 European Centres* - Radiation Protection Dosimetry vol. 31, 437-442 (1990)

[24] T. Loncol, V. Cosgrove, J.M. Denis, J. gueulette, A. Mazal, H.G. Menzel, P. Pihet, R. Sabattier - *Radiobiological Effectiveness of Radiation Beams with Broad LET Spectra: Microdosimetric Analysis Using Biological Weighting Functions* - Radiation Protection Dosimetry vol. 52, 347-352 (1994)

[25] L. De Nardo, V. Cesari, N. Iborra, V. Conte, P. Colautti, J. Hérault, G. Tornielli, P. Chauvel - *Microdosimetric Assessment of Nice Therapeutic Proton Beam Biological Quality* - Physica Medica vol. XX, 71-77 (2004)

[26] A. Tilikidis, B. Lindt, P. Näfstadius, A. Brahme - *An Estimation of Relative Biological Effectiveness of 50 MV Bremsstrahlung Beams by Microdosimetric Techniques* - Physics in Medicine and Biology vol. 41, 55-69 (1996)

[27] Y. Kase et al. - *Microdosimetric Measurements and Estimation of Human Cell Survival for Heavy-Ion Beams* - Radiation Research vol. 166, 629-638 (2006)

[28] Y. Kase et al. - *Biophysical Calculation of Cell Survival Probabilities Using Amorphous Track Structure Models for Heavy-Ion Irradiation* - Physics in Medicine and Biology vol. 53, 37-59 (2008)

[29] International Commission on Radiation Units and Measurements - *Prescribing, Recording, and Reporting Proton-Beam Therapy, ICRU Report no. 78*- Journal of the ICRU vol. 7 (2007)

[30] H. Paganetti, A. Niemierko, M. Ancukiewicz, L.E. Gerweck, M. Goitein, J.S. Loeffler, H.D. Suit - *Relative biological effectiveness (RBE) values for proton beam therapy* - International Journal of Radiation Oncology Biology Physics vol. 53, 407–421 (2002)

[31] H. Suit, T. DeLaney, S. Goldberg, H. Paganetti, B. Claise, L. Gerweck, A. Niemierko, E. Hall, J. Flanz, J. Hallman, A. Trofimov - *Proton vs Carbon Ion Beams in the Definitive Radiation Treatment of Cancer Patients* - Radiotherapy and Oncology vol. 95, 3–22 (2010)

[32] H.G. Menze, L. Lindborg, T. Schmitz, H. Schuhmacher, A.J. Waker - *Intercomparison fo Dose Equivalent Meters Based on Microdosimetric Techniques: Detailed Analysis and Conclusions* - Radiation Protection Dosimetry vol. 29, 55-68 (1989)

[33] International Commission on Radiation Units and Measurements - *Radiation Quantities and Units, ICRU Report no. 33*- Journal of the ICRU vol. 7 (1980)

[34] A.M. Kellerer, H.H. Rossi - *The Theory of Dual Radiation Action* - Current Topics in Radiation Research vol. 8, 85-156 (1974)

[35] D.T. Goodhead - *Energy Deposition Stochastics and Track Structure: What About the Target?* - Radiation Protection Dosimetry vol. 122, 3–15 (2006)

[36] R.B. Hawkins - *A Microdosimetric-Kinetic Model for the Effect of Non-Poisson Distribution of Lethal Lesions on the Variation of RBE with LET* - Radiation Research vol. 160, 61–69 (2003)

[37] L. Lindborg, M. Hultqvist, Å. Carlsson Tedgren, H. Nikjoo - *Lineal Energy and Radiation Quality in Radiation Therapy: Model Calculations and Comparison With Experiments* - Physics in Medicine and Biology vol. 58, 3089-3105 (2013)

[38] R.R. Wilson - *Radiological use of fast protons* - Radiology vol. 47, 487-491 (1946)

[39] W.P. Levin, H. Kooy, J.S. Loeffler, T.F. DeLaney - *Proton beam therapy* - British Journal of Cancer vol. 93, 849-854 (2005)

[40] H.H. Rossi, M. Zaider - *Microdosimetry and Its Applications* - Springer-Verlag (1996)

[41] U. Fano - *Note on the Bragg-Gray Cavity Principle for Measuring Energy Dissipation* - Radiation Research vol. 1, 237-240 (1954)

[42] International Commission on Radiation Units and Measurements - *Microdosimetry, ICRU Report no. 36* - Bethesda, MD (1983)

[43] S. Chiriotti, D. Moro, P. Colautti, V. Conte, B. Grosswendt - *Equivalence of Pure Propane and Propane-TE Gases for Microdosimetric Measurements* - LNL-INFN Annual Report (2013)

[44] P.J. Campion - *The operation of proportional counters at low pressures for microdensity* - Physics in Medicine and Biology vol. 16, 611-616 (1971)

[45] D. Moro, S. Chiriotti, P. Colautti, V. Conte - *TEPC Gas Gain Measurements in Propane* - Radiation Protection Dosimetry vol. 161, 459-463 (2014)

[46] A.J. Waker - *Gas Gain Characteristics of Some Walled Proportional Counters Used in Microdosimetry* - Microdosimetry Proceedings of the Eighth Symposium, Report EUR 8395 (1982)

[47] P. Ségur, P. Olko, P. Colautti - *Numerical Modelling of Tissue-Equivalent Proportional Counters* - Radiation Protection Dosimetry vol. 61, 323-350 (1995)

[48] A.M. Kellerer - *Fundamentals of microdosimetry* - in K.R. Kase, B.E. Bjamgard, F.H. Attix - *Dosimetry of Ionizing Radiation. Volume I* - Academic Press, 77-162 (1985)

[49] D. Moro, V. Conte, S. Chiriotti, P. Colautti - *The study of a mini TEPC for carbon ion therapy* - LNL-INFN Annual Report (2013)

[50] D. Moro, L. De Nardo, P. Colautti, V. Conte, et al. - *EuTEPC (European Tissue Equivalent Proportional Counter): a Microdosimeter for the Assessment of the Radiation Quality at the International Space Station* - LNL-INFN Annual Report (2011)

[51] G.F. Knoll - *Radiation Detection and Measurement*, 3rd ed. - John Wiley & Sons Inc. (2000)

[52] V.T. Jordanov, G.F. Knoll - *Digital Synthesis of Pulse Shapes in Real Time for High Resolution Radiation Spectroscopy* - Nuclear Instruments and Methods in Physics Research A vol. 345, 337-345 (1994)

[53] A.J. Waker - *Principles of Experimental Microdosimetry* - Radiation Protection Dosimetry vol. 61, 297-308 (1995)

[54] S.Gerdung, P. Pihet, J.E. Grindborg, H. Roos, U.J. Schrewe, H. Schuhmacher - *Operation and Application of Tissue-Equivalent Proportional Counters* - Radiation Protection Dosimetry vol. 61, 381-404 (1995)

[55] D. Moro, E. Seravalli, P. Colautti - *Statistical and Overall Uncertainties in BNCT Microdosimetric Measurements* - LNL-INFN Annual Report (2003)

[56] V. Conte, D. Moro, B. Grosswendt, P. Colautti - *Lineal Energy Calibration of Mini Tissue Equivalent Gas-Proportional Counters (TEPC)* - AIP Conference Proceedings vol. 1530, 171-178 (2013)

[57] NIST database for electrons stopping powers - *http://physics.nist.gov/PhysRefData/Star/Text/ESTAR.html*

[58] International Commission on Radiation Units and Measurements - *Stopping Powers for Electrons and Positions, ICRU Report no. 37* - Bethesda, MD (1984)

[59] NIST database for protons stopping powers - *http://physics.nist.gov/PhysRefData/Star/Text/PSTAR.html*

[60] NIST database for protons stopping powers - *http://physics.nist.gov/PhysRefData/Star/Text/ASTAR.html*

[61] International Commission on Radiation Units and Measurements - *Stopping Powers and Ranges for Protons and Alpha Particles, ICRU Report no. 49* - Bethesda, MD (1993)

[62] P.R. Bevington, D.K. Robinson - *Data Reduction and Error Analysis for the Physical Sciences* - McGraw Hill (1969)

[63] L.H. Gray - *An Ionization Method for the Absolute Measurement of γ -Ray Energy* - Royal Society of London Proceedings Series A vol. 156, 578-596 (1936)

[64] J.F. Ziegler, J.P. Biersack, M.D. Ziegler - *SRIM - The Stopping and Range of Ions in Matter* - http://www.srim.org

[65] International Commission on Radiation Units and Measurements - *Stopping of Ions Heavier Than Helium, ICRU Report no. 73* - Bethesda, MD (2005)

[66] E. Haettner, H. Iwase, D. Schardt - *Experimental Fragmentation Studies with ^{12}C Therapy Beams* - Radiation Protection Dosimetry vol. 122, 485-487 (2006)

[67] K. Gunzert-Marx, H. Iwase, D. Schardt, R.S. Simon - *Secondary Beam Fragments Produced by 200MeVu^{-1} ^{12}C Ions in Water and Their Dose Contributions in Carbon Ion Radiotherapy* - New Journal of Physics vol. 10, 075003 (2008)

[68] S. Chiriotti, D. Moro, E. Motisi, M. Ciocca, P. Colautti, V. Conte - *First Microdosimetric Measurements at CNAO* - LNL-INFN Annual Report (2014)

[69] S. Endo, K. Tanaka, M. Takada, Y. Onizuka, N. Miyahara, T. Sato, et al. - *Microdosimetric Study for Secondary Neutrons in Phantom Produced by a 290 MeV/nucleon Carbon Beam* - Medical Physics vol. 34, 3571-3578 (2007)

[70] T.T. Böhlen, M. Dosanjh, A. Ferrari, I. Gudowska - *Simulations of Microdosimetric Quantities with the Monte Carlo code FLUKA for Carbon Ions at Therapeutic Energies* - International Journal of Radiation Biology vol. 88, 176-182 (2012)